Jouni Vuojolainen

IDENTIFICATION OF MAGNETICALLY LEVITATED MACHINES

ACTA UNIVERSITATIS LAPPEENRANTAENSIS 907

Jouni Vuojolainen

IDENTIFICATION OF MAGNETICALLY LEVITATED MACHINES

Dissertation for the degree of Doctor of Science (Technology) to be presented with due permission for public examination and criticism in the room 1316 at Lappeenranta–Lahti University of Technology LUT, Lappeenranta, Finland on the 16th of June, 2020, at noon.

Acta Universitatis
Lappeenrantaensis 907

Supervisors Professor Olli Pyrhönen
Laboratory of Control Engineering and Digital Systems
LUT School of Energy Systems
Lappeenranta–Lahti University of Technology LUT
Finland

Dr. Rafal P. Jastrzebski
Laboratory of Control Engineering and Digital Systems
LUT School of Energy Systems
Lappeenranta–Lahti University of Technology LUT
Finland

Reviewers Associate Professor Arkadiusz Mystkowski
Department of Automation and Control Engineering
Bialystok University of Technology
Poland

Assistant Professor Eric Severson
Department of Electrical and Computer Engineering
University of Wisconsin Madison
USA

Opponents Associate Professor Marko Hinkkanen
Department of Electrical Engineering and Automation
Aalto University
Finland

Associate Professor Arkadiusz Mystkowski
Department of Automation and Control Engineering
Bialystok University of Technology
Poland

ISBN 978-952-335-517-0
ISBN 978-952-335-518-7 (PDF)
ISSN-L 1456-4491
ISSN 1456-4491

Lappeenranta–Lahti University of Technology LUT
LUT University Press 2020

Abstract

Jouni Vuojolainen
Identification of magnetically levitated machines
Lappeenranta 2020
68 pages
Acta Universitatis Lappeenrantaensis 907
Diss. Lappeenranta–Lahti University of Technology LUT
ISBN 978-952-335-517-0, ISBN 978-952-335-518-7 (PDF)
ISSN-L 1456-4491, ISSN 1456-4491

Magnetically levitated machines use magnetic levitation to maintain the separation between the bearing races. They offer various benefits compared with other types of bearings: no contact between the bearing races, the absence of lubrication, and suitability for high-speed applications. Magnetically levitated machines can be divided into two groups: active magnetic bearing (AMB) and bearingless machines.

An active magnetic bearing is the traditional magnetic bearing. AMBs use electromagnets to maintain the rotor in a stable position. Bearingless machines are similar to AMB machines, but they use the same air gap for the generation of the torque-producing and levitation flux. Magnetically levitated systems are unstable, complex, and nonlinear multi-input multi-output systems. Thus, they require feedback control for stable operation. Further, accurate modeling is essential for the robust control of these systems.

In this doctoral dissertation, the system identification aspect of magnetically levitated systems is considered. In general, system identification refers to construction of mathematical models of systems by measuring input-output data during an identification experiment. System identification can assist in the modeling, and more accurate models can be built with real data. In this dissertation, different excitation signals; pseudorandom binary sequence (PRBS), chirp, stepped sine, and multisine are first applied to the AMB system identification for single-input single-output and multi-input multi-output cases. Next, the online identification of an AMB rotor–bearing system with a sliding discrete Fourier transform with the direct and indirect identification is shown. Then, the identification methods used for AMB machines are applied to bearingless machines. The effects of noise and delay on the linearized plant identification accuracy based on nonlinear simulation models are examined. Finally, the AMB rotor–bearing system identification with the PRBS for a multi-input multi-output system is presented.

The doctoral dissertation provides results for the identification of a magnetically levitated system. Several laboratory test rigs were used to obtain the results. It is shown that the methods used for the AMB system identification can be applied to bearingless machines.

Keywords: active magnetic bearings, bearingless machines, modeling, frequency domain identification, system identification

Acknowledgements

This study was carried out at the Laboratory of Control Engineering and Digital Systems at Lappeenranta–Lahti University of Technology LUT, Finland, between 2016 and 2019.

I would like to thank Professor Olli Pyrhönen for the opportunity to work with a very skillful research team on projects related to magnetically levitated systems. His guidance and help during the whole dissertation process is highly appreciated. I am grateful to Dr. Rafal Jastrzebski for comments, discussions, and help with the various parts of the research and doctoral dissertation. I also wish to thank the members of the magnetic levitation team, Mr. Teemu Sillanpää, Dr. Pekko Jaatinen, and Dr. Niko Nevaranta. For the help in scientific writing and language improvement of the first publication, I would like to thank Mr. Peter Jones. Thanks are extended to Dr. Hanna Niemelä for improving the language of this doctoral dissertation.

I would like to express my gratitude to the preliminary examiners of the dissertation, Associate Professor Arkadiusz Mystkowski from Bialystok University of Technology and Assistant Professor Eric Severson from the University of Wisconsin Madison for their valuable comments and suggestions for improving this doctoral dissertation.

Lastly, I would like to thank my family for their support during this project.

Jouni Vuojolainen
May 2020
Lappeenranta, Finland

Contents

List of publications

Publication I
Vuojolainen, J., Jastrzebski, R., and Pyrhönen, O. (2016). Using a pseudorandom binary sequence for rotor-bearing system identification in active magnetic bearing rotor systems. In *15th International Symposium on Magnetic Bearings (ISMB15)*, Kitakyushu, Japan, pp. 618–625.

In this publication, Mr. Vuojolainen designed and implemented the pseudorandom binary sequence and conducted the experiments and postprocessed the experimental data. He was the principal author of the paper.

Publication II
Jastrzebski, R., Vuojolainen, J., Jaatinen, P., Sillanpää, T., and Pyrhönen, O. (2016). Commissioning of Modular 10 kW Magnetically Levitated Test Rig. In *2016 19th International Conference on Electrical Machines and Systems (ICEMS)*, Chiba, Japan, pp. 1–6.

In this publication, Mr. Vuojolainen helped in conducting the experiments and postprocessing of the experimental data. Dr. Jastrzebski was the principal author of the paper.

Publication III
Vuojolainen, J., Nevaranta, N., Jastrzebski, R., and Pyrhönen, O. (2017). Online identification of AMB rotor system dynamics using sliding DFT. In *2017 IEEE 11th International Symposium on Diagnostics for Electrical Machines, Power Electronics and Drives (SDEMPED)*, Tinos, Greece, pp. 267–273.

In this publication, Mr. Vuojolainen designed the sliding DFT algorithm based on Dr. Nevaranta's work. Mr. Vuojolainen also conducted the experiments, postprocessed the experimental data, and was the principal author of the paper. Dr. Nevaranta helped significantly in the writing process.

Publication IV
Vuojolainen, J., Nevaranta, N., Jastrzebski, R., and Pyrhönen, O. (2017). Comparison of Excitation Signals in Active Magnetic Bearing System Identification. *Modeling, Identification and Control*, vol. 38, no. 3, pp. 123–133.

In this publication, Mr. Vuojolainen designed and implemented several different identification signals, conducted the experiments and postprocessed the experimental data, and was the principal author of the paper. The other authors helped in the writing process.

Publication V
Nevaranta, N., Vuojolainen, J., Sillanpää, T., and Pyrhönen, O. (2019). Pseudo Random Binary Signal for MIMO Frequency Response Identification of a Magnetically Levitated Rotor System. *IOP Conference Series: Materials Science and Engineering*, 643. pp. 012146.

Mr. Vuojolainen helped in the writing process and formatting of the results. Dr. Nevaranta was the principal author of the paper.

Publication VI
Jaatinen, P., Vuojolainen, J., Nevaranta, N., Jastrzebski, R., and Pyrhönen, O. (2019). Control System Commissioning of Fully Levitated Bearingless Machine. *Modeling, Identification and Control*, vol. 40, no. 1, pp. 27–39.

Mr. Vuojolainen converted the AMB rotor-bearing system identification to bearingless machines. Dr. Jaatinen was the principal author of the paper.

Nomenclature

To clarify the nomenclature used in **Publications I–VI**, some of the symbols below are provided with their different meanings in the respective publications, indicated by (**I**)–(**VI**).

Abbreviations

AMB	active magnetic bearing
DFT	discrete Fourier transform
DOF	degree of freedom
DX	drive-end x-axis
DY	drive-end y-axis
FEM	finite element method
FFT	fast Fourier transform
FRF	frequency response function
IPM	interior permanent magnet
MIMO	multi-input multi-output
NX	non-drive-end x-axis
NY	non-drive-end y-axis
PM	permanent magnet
PRBS	pseudorandom binary sequence
SDFT	sliding discrete Fourier transform
SIMO	single-input multi-output
SISO	single-input single-output
SNR	signal to noise ratio

Greek Symbols

α	angle between a pole and the control axis	deg
β	rotation around axis	rad
λ'_m	suspension force constant	H/m
μ_0	magnetic permeability of air	H/m
Ω	rotational speed	rad/s
ω_{bw}	bandwidth of the power amplifier	rad/s
$\boldsymbol{\Phi}$	reduced mode shape function matrix	
ϕ	phase angle	rad
ψ	flux linkage	Wb-turn
θ	moment	Nm

Symbols

A	amplitude	
$\mathbf{A}$	state matrix	
A_{air}	air gap cross-sectional area	m^2
$\mathbf{B}$	input matrix	
$\mathbf{C}$	output matrix	

$C(\mathrm{j}\omega_k)$	controller transfer function	
d	PRBS number of cells, (**I**, **IV**–**V**)	
d	distance from the center of mass	
$\mathbf{D}$	feedforward matrix	
$\mathbf{D}_\mathrm{M}$	mechanical model damping matrix	
e	natural logarithm	
F	force	N
f	excitation frequency	Hz
$\mathbf{F}$	force vector	
f_0	chirp signal start frequency	Hz
f_1	chirp signal end frequency	Hz
f_r	PRBS frequency resolution	Hz
f_s	sampling frequency	Hz
$\mathbf{G}_\mathrm{M}$	mechanical model gyroscopic matrix	
g_0	air gap between a pole and the rotor	m
$G_0(\mathrm{j}\omega_k)$	open loop transfer function	
$G_\mathrm{cl}(\mathrm{j}\omega_k)$	closed-loop transfer function	
G_{cc}	transfer function of the power amplifier	
G_p	gain of the feedback current control loop	
i	coil current	A
$\mathbf{I}$	identity matrix	
$\mathbf{i}$	current vector	
i_b	bias current	A
i_c	control current	A
i_m	electromagnet magnetizing current	A
i_max	maximum current	A
i_ref	reference current	A
I_x	transversal moment of inertia about *x*-axis	kgm^2
I_y	transversal moment of inertia about *y*-axis	kgm^2
I_z	*z*-axis rotational moment of inertia	kgm^2
j	imaginary unit	
k	chirp signal rate of change	
$\mathbf{K}$	stiffness matrix	
$\mathbf{K}_\mathrm{i}$	current stiffness matrix	N/A
$\mathbf{K}_\mathrm{x}$	position stiffness matrix	N/m
k_i	current stiffness	N/A
k_u	velocity-induced voltage coefficient	
k_x	position stiffness	N/m
k_{x1}	suspension position stiffness	N/m
k_{x2}	suspension position stiffness related to the q-axis motor drive current	N/m
L	PRBS number of data points, (**I**, **IV**–**V**)	
L	inductance	H
l	length	
l	length of the inductor core	m

l_{air}	length of the air gap	m
m	mass	kg
$\mathbf{M}$	mass matrix	
M'	suspension force constant	Wb/m
N	PRBS signal length, (**I**, **IV**–**V**)	
N	number of samples, (**III**)	
N	number of coil turns	
n	index, (**IV**)	
n	time instant, (**III**)	
$\mathbf{N}$	shape function matrix	
N_f	number of frequencies in the multisine signal	
P	number of nodes in the FEM analysis	
$\mathbf{q}$	displacement vector	
R	resistance	Ω
$R(\mathrm{j}\omega_k)$	discrete Fourier transform of the reference signal	
s	Laplace variable	
$\mathbf{S}$	nodal location	
T	chirp signal end time	s
t	time	s
$\mathbf{T}_1$	transformation matrix	
$\mathbf{T}_2$	transformation matrix	
$\mathbf{T}_\mathrm{s}$	transformation matrix	
T_s	sampling time	
u	voltage	V
$\mathbf{u}$	input vector	
$U(\mathrm{j}\omega_k)$	discrete Fourier transform of the input signal	
$u(k)$	plant input	
$u_1(k)$	AMB current reference signal	
u_{dc}	DC link voltage	V
W	magnetic energy	J
w	width of the inductor core	m
W'	magnetic coenergy	J
$w(k)$	excitation signal	
x	x-axis displacement	m
$\mathbf{x}$	state vector	
$X(\mathrm{n})$	harmonic on the n^{th} time instant	
$x(\mathrm{n})$	DFT/SDFT input signal	
y	y-axis displacement	m
$\mathbf{y}$	output vector	
$Y(\mathrm{j}\omega_k)$	discrete Fourier transform of the output signal	
$y(k)$	plant output	
$y_1(k)$	AMB measured current	
$y_2(k)$	measured position signal	

Superscripts

g	in global coordinates
H	complex conjugate transpose
m	in modal coordinates
T	transpose

Subscripts

A	bearing A
a	actuator
B	bearing B
b	in bearing coordinates
c	control current
d	direct (d) axis
i	element number
k	index
lo	lower electromagnet
m	motor
q	quadrature (q) axis
r	rotor
s	sensor
s	suspension
up	upper electromagnet
x	x-axis/direction
y	y-axis/direction

1 Introduction

This chapter presents the motivation, background, objectives, and scope of this doctoral dissertation. An introduction into magnetically levitated systems is given. System identification and rotor modeling are discussed in brief. The outline of the dissertation and the scientific contributions are presented.

1.1 Motivation and background

Bearings are important machine elements used to reduce friction between moving parts and constrain relative motion to the desired motion. One of the most common bearing types is the rolling element bearing, which uses rollers to maintain the separation between the bearing races. This type of bearing is suitable for many applications, but it suffers from the sliding friction. This will eventually lead to a bearing failure and a need to replace the bearing. In some applications, the bearing failure time can be very short. The mechanical bearing is also usually the first point of failure, and the lubrication oil or grease may cause problems (Eaton et al., 2010). Advantages of mechanical bearings are their affordability and capability to provide high force density.

A fluid bearing is one alternative to rolling element bearings. These bearings use either gas or liquid, typically oil or working fluid, for example water, between the bearing races. This allows fluid bearings to have no sliding friction, and they are able to support high-load and high-speed applications better than rolling element bearings. However, these bearings also have significant disadvantages: the liquid must stay inside the bearing, which may be challenging to ensure. Furthermore, fluid bearings cannot be used in extreme temperatures and processes where contamination is a problem. In particular, gas bearings retain their low friction and low thermal effects at high speeds exceeding maximum allowable speeds for oil and roller bearings. Nevertheless, they face stability issues, and their modeling can also be very challenging (Czolczynski, 1999).

An active magnetic bearing (AMB) is a type of bearing that uses magnetic levitation to maintain the separation between the bearing races. This offers advantages over fluid and rolling element bearings. As there is no contact between the bearing races and no lubrication, AMBs can be used where contamination is a problem. They are also suitable for high-speed applications, and the rotational speed is typically only limited by the material strengths of the rotor (Schweitzer and Maslen, 2009). AMBs also have their disadvantages; they need safety bearings in case of an AMB failure or power loss. The design of AMBs is also not a simple task and requires knowledge of several fields of science. The investment cost is also high. If large levitation forces are needed, AMBs may lengthen the rotor so that it becomes supercritical, which is highly undesirable.

AMBs have been extensively studied at LUT University, producing many scientific publications and doctoral dissertations. Jastrzebski (2007) presented an FPGA-based LQ control of active magnetic bearings with the dSPACE platform. Hynynen (2011) focused on

the system identification of AMBs in single-input single-output (SISO) and multi-input multi-output (MIMO) cases using multisine and stepped sine signals. Smirnov (2012) introduced an automatic commissioning procedure of a high-speed motor levitated with AMBs.

In recent years, the bearingless machines have also become a research topic at LUT University. Several scientific publications and one doctoral dissertation have been published on this topic (Jaatinen, 2019).

Bearingless machines use the same air gap for the generation of the torque-producing and levitation flux. This allows them to be shorter than AMB machines thereby enabling higher critical speeds; however, they are not able to produce as much levitation force as standard AMB machines (Chiba, 2005). However, normally, the acting surfaces are much larger, often ensuring sufficient forces.

AMBs and bearingless machines have also been investigated in numerous studies. In (Gosiewski and Mystkowski, 2008), robust control of a radial AMB with a rigid rotor was considered. (Mystkowski et al., 2018) discussed the use of the Newton observer for estimation of the magnetic flux within the feedback control of a nonlinear AMB system. In (Sokolov et al., 2019), modeling of a bearingless synchronous reluctance motor with combined windings was presented. (Severson, 2018) addressed the usability of bearingless machines in industrial and transportation applications.

1.2 Objectives and scope of the dissertation

The main objective of the dissertation is to provide different system identification methods for magnetically levitated systems. Different excitation signals (chirp or swept sine, multisine, pseudorandom binary sequence (PRBS), and stepped sine) are used for the system identification. Direct and indirect identification and sliding discrete Fourier transform (SDFT) are used for the AMB rotor–bearing system identification. The rotor–bearing system identification of a bearingless machine is presented. SISO, single-input multiple-output (SIMO), and MIMO identification are considered for the AMB machine and SISO for the bearingless machine.

The main scope of the dissertation is in the nonparametric frequency domain estimation. Parametric estimation is used only in **Publication IV**.

1.3 Introduction of magnetically levitated systems

A magnetically levitated system is a system where the rotor is supported by magnetic levitation rather than by a standard rolling element bearing, film bearing, or the like. Rolling element bearings are able to provide force densities of around 205 N/cm^2, fluid bearings around 69 N/cm^2, and magnetically levitated systems around 80 N/cm^2 (Clark

et al., 2004). These systems can be divided into two groups: traditional AMB machines and bearingless machines.

1.3.1 Active magnetic bearings (AMBs)

AMBs apply magnetic levitation to support the rotor in its nominal position. The simplest magnetic levitation system is a one-degree-of-freedom (DOF) system, where one object such as a ball made from a ferromagnetic material is levitated. The system consists of one electromagnet, a displacement sensor for detecting the ball position, a controller, and a current regulator, which amplifies the current command of the controller. With such a system, stable levitation can be achieved, because without active control the system would be unstable. When there is current flowing in the conductor, the electromagnet produces a magnetic field, which produces a force that pulls the object towards it. An example of such a system is shown in Fig. 1.1.

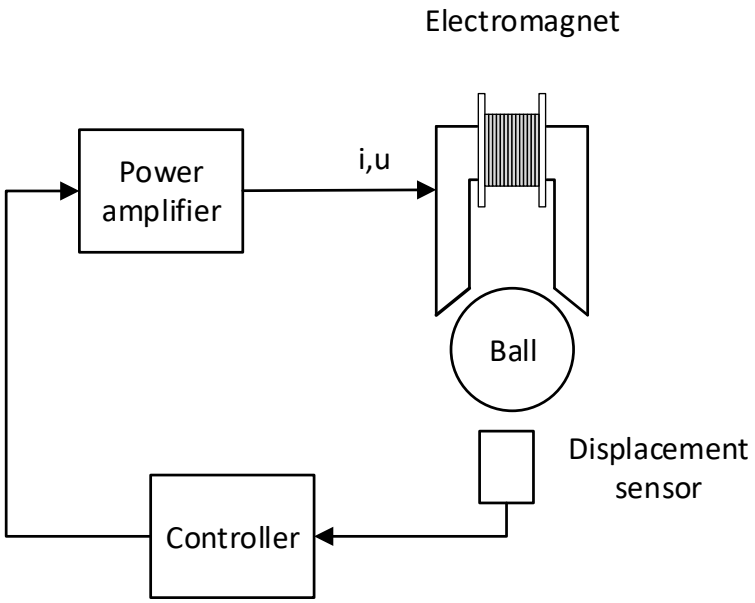

Figure 1.1. One-degree-of-freedom magnetic levitation system.

A typical AMB system consists of two radial (xy plane) AMBs and one axial (z-plane) AMB. Three or more radial AMB planes are sometimes applied, for instance in (Jastrzebski et al., 2019). One radial AMB is thus a 2-DOF system, and the axial one is a 1-DOF system. In total, this will result in a 5-DOF system. Typically, each degree of freedom is controlled with two electromagnets. The purpose of using two electromagnets per one

DOF is to provide force in both directions, because electromagnets can only provide positive pull force. Position information related to all degrees of freedom is also needed. This requires a minimum of five position sensors or more, if differential or redundant measurements are used. Safety bearings must also be used in case of an AMB failure, rotor touchdown, or for safely holding the rotor while the system is not powered. An example of a simple 5-DOF AMB system is shown in Fig. 1.2.

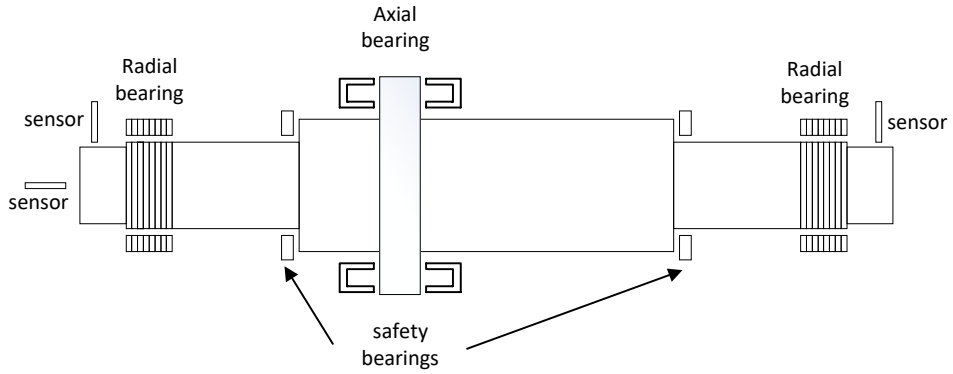

Figure 1.2. Simple five-degree-of-freedom AMB system.

There are also different AMB actuator configurations. In the heteropolar configuration, the polarities of the stator poles vary. In this case, the magnetic flux is confined to the plane perpendicular to the axis of rotation. In the homopolar configuration, the stator poles have the same polarity, and at least some of the flux passes axially along the rotor (Schweitzer and Maslen, 2009).

In permanent magnet (PM) biased magnetic bearings, permanent magnet materials are used to provide the bias magnetic flux. This has the advantage that the power loss related to maintaining the bias field is eliminated (Schweitzer and Maslen, 2009). They can also be useful in vertically oriented machines as they eliminate the gravity force, which is constant. One such example is a flywheel, where low power losses are essential. In some setups, some degrees of freedom can be controlled totally passively with permanent magnets only. Passive permanent magnet bearings often use Halbach arrays to increase stiffness (Mystkowski and Ambroziak, 2010).

There are also hybrid AMBs, where both radial and axial forces can be generated. One such example is the conical AMB. With this configuration, it is possible to generate also axial forces (Katyayn and Agarwal, 2017). In setups where low axial forces are needed, conical AMBs are one option. This also has the advantage that the rotor can be shorter as there is no need for a separate axial AMB. Other solutions are also applied, for instance a dead pole for combining axial and radial AMBs (Filatov et al., 2016).

1.3.2 Bearingless machines

Bearingless machines use the same air gap for the generation of the torque-producing and levitation flux. The radial levitation force generation with a 4-pole motor and a 2-pole suspension winding is shown in Fig. 1.3. When the conductor 2a is energized, the flux density in the air gap region 1 increases and the flux density in the air gap region 3 decreases. This produces a positive force in the *x*-direction. The same holds in Fig. 1.3b when the current on the conductor 2a is reversed; the flux density in the air gap region 3 increases and the flux density in the air gap region 1 decreases, producing a negative force in the *x*-direction. The same principle applies to the force generation in the *y*-direction as shown in Fig. 1.4. Bearingless machines with combined windings and current injection can also be applied (Jastrzebski et al., 2017b).

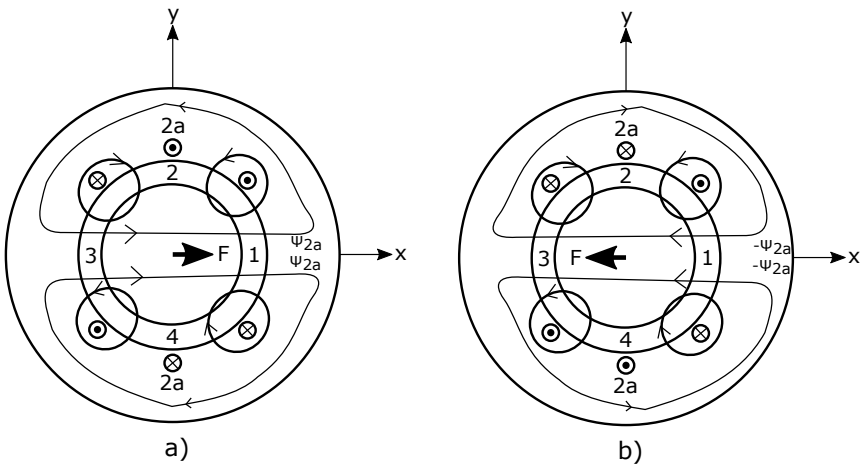

Figure 1.3. Bearingless machine levitation force generation in the *x*-direction; a) positive, b) negative. 4-pole motor and a 2-pole suspension winding.

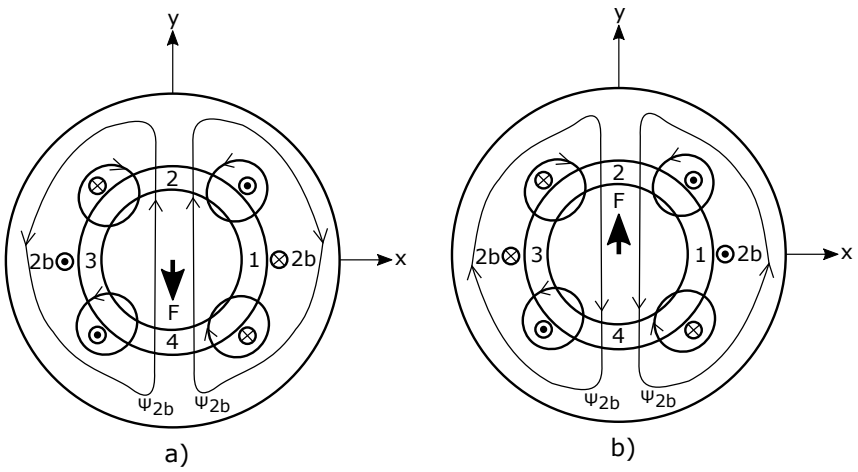

Figure 1.4. Bearingless machine levitation force generation in the *y*-direction; a) negative b) positive. 4-pole motor and a 2-pole suspension winding.

1.4 Rotor modeling of magnetically levitated systems

The rotors of AMB systems and bearingless machines can be modeled as either rigid or flexible. In the rigid rotor, the critical frequencies are higher than the maximum rotational speed and the bandwidth of the position controller. In the flexible rotor, the critical frequencies are lower than the maximum rotational speed. The rotor behavior at the critical speed can be affected by the position controller and may be crossed during run-down and run-up. Modeling of flexible rotors requires modeling of the elastic behavior of the rotor (Lösch, 2002). It should be noted that pure rigid rotors do not exist, and typically, one or more flexible modes are modeled even though the rotor is assumed rigid.

One rule of thumb is that the rotor is assumed rigid if the rotational speed is below 30–50% of the first critical frequency. A Campbell diagram is a visual tool used to determine if the rotor can be assumed rigid or flexible. The Campbell diagram plots the rotational speed of the rotor and the flexible eigenfrequencies on the axes. The Campbell diagram shows the splitting of the flexible eigenfrequencies caused by the gyroscopic forces when the rotational speed increases. The flexible eigenfrequencies are split into forward modes, which have an increasing frequency, and backward modes, which have a decreasing frequency. The intersection points between the forward and backward modes and the rotational speeds are called critical frequencies of the rotor. An example Campbell diagram of the 10 kW AMB test rig rotor is shown in Fig. 1.5.

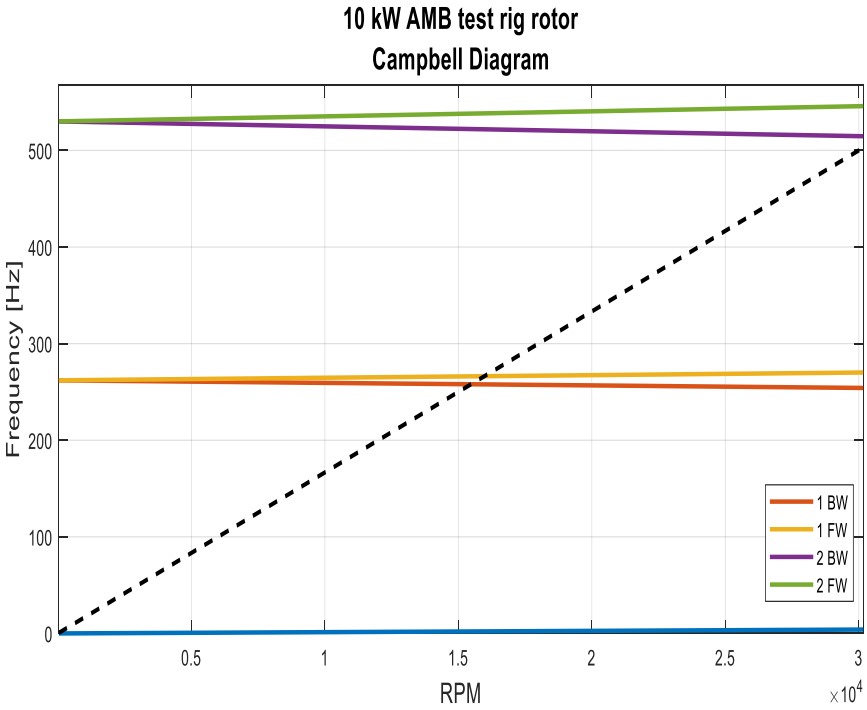

Figure 1.5. Campbell diagram of the 10 kW AMB test rig rotor. The black dashed line shows the rotor rotational speed.

1.5 System identification

System identification is a methodology of constructing mathematical models of systems. System inputs and outputs are typically measured during an identification experiment, and an experimental model is generated from this data set (Ljung, 1987).

For stable systems where operation without a controller is possible, the plant can be identified directly with open-loop identification methods. For unstable systems, such as AMB rotor systems, the plant identification has to be performed with a closed-loop feedback. However, the controller can affect the identification results. The closed-loop identification can be divided into three subcategories: direct, indirect, and joint-input-output methods. In the direct approach, the effect of the controller is neglected, and the plant is identified as in the case of an open-loop system. In the indirect approach, the effect of the known controller is taken into account by solving the open-loop transfer function from the identified closed-loop transfer function. In the joint-input-output approach, both the plant and the feedback dynamics can be identified using the plant inputs and outputs as the system outputs. The joint-input-output approach was discussed in (Anderson and Gevers, 1979).

In the case of magnetically levitated systems, the system identification must be carried out in the closed loop because the open-loop system is unstable. Typically, the first direct approach is used as it is the easiest and requires no knowledge of the feedback loop. After that, an indirect or joint-input-output approach should be used for better results.

In this dissertation, system identification is used for the magnetically levitated system identification. Different excitation signals (chirp or swept sine, multisine, PRBS, and stepped sine) and identification methods are applied.

1.6 Outline of the dissertation

This dissertation is presented in the following six chapters:

Chapter 1 shows the motivation, background, and objectives of the dissertation. An overview of magnetically levitated systems and system identification is given.

Chapter 2 deals with a detailed analysis of magnetically levitated systems; AMB machines and bearingless machines. The basic theory for the magnetic levitation is presented. References of the analytical modeling of magnetically levitated systems are given.

Chapter 3 addresses the rotor modeling of AMB and bearingless machines. Rigid and flexible models are discussed.

Chapter 4 gives a more detailed introduction to the system identification. Specific conditions in magnetically levitated systems (unstable nature, nonlinearities, SISO, SIMO, and MIMO identification) are provided.

Chapter 5 presents the simulation and experimental results with laboratory test rigs of two AMB machines and one bearingless machine. A short description of each test rig is given. The estimation errors, uncertainties in measurement signals, and identification results are discussed in brief.

Chapter 6 summarizes the work and provides suggestions for future work.

1.7 Scientific contributions and publications

In this doctoral dissertation, an identification methodology was developed. The dissertation provides the following scientific contributions:

- Pseudorandom binary sequence is applied to the AMB system identification in SISO, SIMO, and MIMO cases.
- A comparison of different excitation signals (PRBS, chirp, stepped sine, and multisine) in the SISO AMB system identification is made.

- Online identification of an AMB rotor–bearing system is carried out with a sliding discrete Fourier transform (DFT) using a multisine excitation signal in the SIMO identification with the indirect and direct methods.

- The identification methods of AMB machines are applied to bearingless machines.

The following publications address the topics of this dissertation:

Publication I discusses the use of a pseudorandom binary sequence for the rotor–bearing system identification of an AMB system in the SISO case. A comparison is made with the stepped sine excitation signal, and it is shown that the PRBS provides adequate frequency response estimation in the nonparametric case. Results of the inner current control loop identification are also given. Furthermore, harmonic analysis of the rotor–bearing system is presented with a constant amplitude stepped sine signal.

Publication II focuses on the commissioning of a 10 kW AMB test rig, which is used to obtain the results presented in this publication and **Publications I**, **III**, and **IV**. The publication shows the same identification results as **Publication I**, and provides additional results for the magnetic center identification with different rotor angles and the identification of the current and position stiffnesses with static measurements. Results from the rotational test of the machine are also given together with the analysis of the unbalance compensation and the unbalance magnetic pull from the induction motor.

Publication III studies the online identification of the rotor–bearing system of an AMB machine with the sliding DFT. A comparison of the nonparametric frequency response estimates is made with a multisine excitation signal in the offline and online SISO and SIMO cases with the direct and indirect closed-loop identification. It is found that the SDFT provides accurate FRFs when compared with the offline ones.

Publication IV is a continuation of **Publication I**. It discusses the usage of several different excitation signals (chirp or swept sine, multisine, PRBS, and stepped sine) in the rotor–bearing system identification with AMBs. The excitation signal properties are discussed, and a comparison of the excitation signals is made in the nonparametric frequency response estimation SISO case. Results of the inner current control loop identification are presented. Further, the current and position stiffnesses are identified with different excitation signals and compared with the initial ones and the static measurements from **Publication II**.

Publication V is related to and partially a continuation of **Publication I** and **IV** as it uses the PRBS excitation signal in the AMB rotor–bearing system identification. The publication shows the usage of noncorrelated PRBS excitation signals for the nonparametric frequency response identification of an AMB rotor–bearing system in a MIMO case. The publication presents a hermetic steam turbo generator (HERGE) test rig.

Publication VI is related to **Publication I** and **IV** as it uses the stepped sine excitation signal but now to identify the rotor levitated with a bearingless machine. It is noted that the identification of the rotor–bearing dynamics can be carried out similarly as with the AMB system. This publication mainly focuses on the control design aspect of a 10 kW bearingless permanent magnet synchronous motor.

The author has also published research results related to AMB and bearingless machines, which are not covered in this dissertation:

1. Vuojolainen, J., Smirnov, A., Jastrzebski, R., Sillanpää, T., Behnam, G., Hartikainen, T., and Pyrhönen, O. (2016). Updating the model of a rotor with surface mounted permanent magnets in an active magnetic bearing rotor system. In *15th International Symposium on Magnetic Bearings (ISMB15)*, Kitakyushu, Japan, pp. 534–541.

2. Jastrzebski, R., Sillanpää, T., Jaatinen, P., Smirnov, A., Vuojolainen, J., Lindh, T., Laiho, A., and Pyrhönen, O. (2016). Automated Design of AMB Rotor Systems with Standard Drive, Control Software and Hardware Technologies. In *15th International Symposium on Magnetic Bearings (ISMB15)*, Kitakyushu, Japan, pp. 78–85.

3. Vuojolainen, J., Nevaranta, N., Jastrzebski, R., and Pyrhönen, O. (2018). MATLAB-Based Tool for Teaching of Active Magnetic Bearing Design to Undergraduate Students. In *2018 IEEE 18th International Power Electronics and Motion Control Conference (PEMC)*, Budapest, Hungary, pp. 926–931.

4. Jaatinen, P., Vuojolainen, J., Sillanpää, T., Nevaranta, N., Jastrzebski, R., and Pyrhönen, O. (2018). Motion Control of a Dual-Motor Interior Permanent Magnet Bearingless Machine. In *2018 IEEE 18th International Power Electronics and Motion Control Conference (PEMC)*, Budapest, Hungary, pp. 717–722.

5. Vuojolainen, J., Jastrzebski, R., and Pyrhönen, O. (2018). Balancing of a Rotor with Active Magnetic Bearing System: Comparison of One-and Two-Plane Balancing Procedures. In *2018 20th European Conference on Power Electronics and Applications (EPE'18 ECCE Europe)*, Riga, Latvia, pp. P.1–P.7.

6. Jaatinen, P., Nevaranta, N., Vuojolainen, J., Jastrzebski, R., and Pyrhönen, O. (2019). H_∞ Control of a Dual Motor Bearingless Machine. In *2019 IEEE International Electric Machines & Drives Conference (IEMDC)*, San Diego, USA, pp. 875–881.

7. Jaatinen, P., Nevaranta, N., Vuojolainen, J., Lindh, T., and Pyrhönen, O. (2019). Monitoring Concept for a High-Speed Machine Application with a Magnetically Levitated Rotor System. In *IECON 2019 - 45th Annual Conference of the IEEE Industrial Electronics Society*, Lisbon, Portugal, pp. 1204–1209.

8. Nevaranta, N., Jaatinen, P., Vuojolainen, J., Sillanpää, T., and Pyrhönen, O. (2020). Adaptive MIMO pole placement control for commissioning of a rotor system with active magnetic bearings. *Mechatronics*, vol. 65, pp. 102313.

2 Magnetically levitated systems

In this chapter, active magnetic bearing (AMB) machines and permanent magnet bearingless machines are discussed in detail. The chapter provides a basic force generation equation of a radial AMB, an equation for the power amplifier, and the basic force generation of a bearingless machine. The analytical modeling of magnetically levitated systems is also discussed in brief. The purpose of this chapter is to provide the basic theory of magnetic levitation systems.

2.1 Active magnetic bearings (AMBs)

This chapter presents the basic AMB dynamics and equations. The main focus is on the radial AMB.

2.1.1 Radial actuator model

An electromagnet can only produce positive force. This can be noted from Eq. (2.1), where the force equation of an electromagnet is given as

$$F = \frac{\mu_0 N^2 i^2 A_{air} \cos\alpha}{4 l_{air}^2}, \tag{2.1}$$

where μ_0 is the magnetic permeability of air, i is the coil current, N is the number of coil turns, α is the angle between a pole and the control axis, A_{air} is the air gap cross-sectional area, and l_{air} is the air gap. It can be seen that the force produced by the electromagnet is highly nonlinear because of the relation to the square of the coil current and the inverse square of the air gap.

In order to move the rotor along one axis (x or y), a pair of electromagnets is required. The force generated by a pair of opposing electromagnets is

$$F_x = F_{x,up} - F_{x,lo} = \frac{\mu_0 N^2 A_{air} \cos\alpha}{4} \left(\frac{i_{x,up}^2}{(g_0 - x)^2} - \frac{i_{x,lo}^2}{(g_0 + x)^2} \right), \tag{2.2}$$

where $i_{x,up}$ is the coil current of the upper electromagnet, $i_{x,lo}$ is the coil current of the lower electromagnet, and g_0 is the air gap between a pole and the rotor. For control design purposes, Eq. (2.2) is linearized. The linearization point is assumed to be the center position of the rotor $x \sim 0$. For the current linearization, a bias current i_b is used. The bias current is selected to be less than or equal to half of the maximum coil current i_{max} ($i_b \leq 0.5 i_{\text{max}}$). Thus, the coil currents can be calculated as

$$i_{x,up} = \begin{cases} i_b + i_c, & \text{if } i_c \geq -i_b, \\ 0, & \text{if } i_c < -i_b, \end{cases} \tag{2.3}$$

$$i_{x,lo} = \begin{cases} i_b - i_c, & \text{if } i_c \leq i_b, \\ 0, & \text{if } i_c > i_b, \end{cases} \tag{2.4}$$

where i_c is the control current. The linearized force equation is

$$F_x = k_i i_{x,c} + k_x x, \tag{2.5}$$

where k_i is the current stiffness, and k_x is the position stiffness. They can be calculated as

$$k_i = \frac{\partial F}{\partial i_c}\Big|_{x=0,i_c=0} = \frac{\mu_0 N^2 i_b A_{air} \cos\alpha}{g_0^2}, \tag{2.6}$$

$$k_x = \frac{\partial F}{\partial x}\Big|_{x=0,i_c=0} = \frac{\mu_0 N^2 i_b^2 A_{air} \cos\alpha}{g_0^3}. \tag{2.7}$$

The linearized force shown in Eq. (2.5) holds the linearity well close to the operating point, which is typically the case. In some special cases, such as flux saturation and very low bias currents, more detailed and/or nonlinear models are required (Schweitzer and Maslen, 2009).

2.1.2 Radial AMBs

Radial AMBs are used to support the rotor radially (*xy* plane). A typical configuration of a radial AMB has eight or twelve poles (E-core). The E-core AMB structure is described in (Allaire et al., 2016). In some cases, a higher pole count such as 16 might be used. Radial bearings are laminated (both the stator and the rotor) to allow high flux densities and low eddy currents. Fig. 2.1 shows an example of a 12-pole E-core radial AMB.

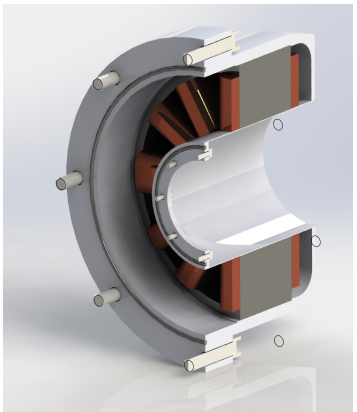

Figure 2.1. Radial AMB from the HERGE test rig, E-core 12 poles. (From **Publication V**).

2.1.3 Axial AMBs

An axial or thrust AMB is used to support the rotor in the axial direction (z-plane). Typically, it has a standard C-core structure. Compared with radial AMBs, axial AMBs are seldom laminated. However, sometimes a segmented structure can be used (Jastrzebski et al., 2019). A solid structure limits the flux density, and high eddy currents are generated. One reason for this is that thin sheets are not able to withstand stresses at high rotational speeds. Fig. 2.2 shows an example of an axial AMB.

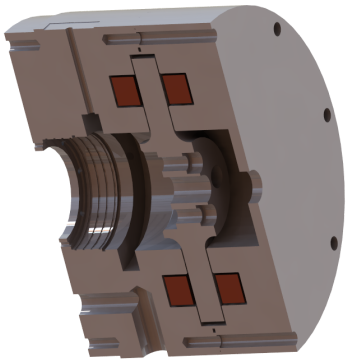

Figure 2.2. Axial AMB from the HERGE test rig. (From **Publication V**).

2.1.4 Power Electronics

AMBs need electricity for operation. Thus, they require controlled power amplifiers, which generate the reference current i_{ref} ($i_{\text{ref}} = i_b \pm i_c$). A simple block diagram of the AMB system is shown in Fig. 2.3.

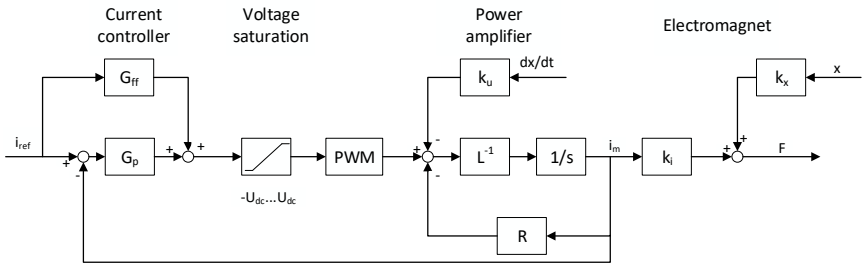

Figure 2.3. Block diagram of the linearized AMB model with the basic inner control loop.

The voltage of the power amplifier is

$$u = L\frac{\mathrm{d}i}{\mathrm{d}t} + Ri + k_u\frac{\mathrm{d}x}{\mathrm{d}t}, \tag{2.8}$$

where R is the resistance of the coil, and L is the inductance. When neglecting magnetic saturation, hysteresis, eddy currents, and leakage flux paths, the equation for the inductance L is written as

$$L = \frac{N^2\mu_0 wl}{2(g_0 - x)}. \tag{2.9}$$

According to Eq. (2.9), the inductance L is not constant but varies in the nonlinear model, whereas in the linear model it has a constant value. k_u is the velocity-induced voltage coefficient, and it is approximately equal to half of the current stiffness k_i. However, this can be neglected in most applications as the magnitude is low compared with the voltage of the coil (Schweitzer and Maslen, 2009). The resistance R can also be neglected as it is very low. Based on these assumptions, a first-order model of the closed-loop dynamics of the power amplifier can be written as

$$G_{cc} = \frac{i_m}{i_{\text{ref}}} \approx \frac{G_P}{sL + G_p}, \tag{2.10}$$

where i_m is the magnetizing current of the electromagnet, and G_p is the gain of the feedback current control loop. In a similar way, based on the bandwidth of the power amplifier, we obtain

$$G_{cc} \approx \frac{\omega_{bw}}{s + \omega_{bw}}, \tag{2.11}$$

where ω_{bw} is the bandwidth of the power amplifier. Using the rise time of the first-order approximation, the bandwith of the power amplifier is (Jastrzebski, 2007)

$$\omega_{bw} = \frac{\ln(9)u_{dc}}{Li_{\text{max}}}. \tag{2.12}$$

2.2 Permanent magnet bearingless machines

Force generation of a bearingless machine can be calculated as follows. The flux linkages of the motor and the suspension winding direct and quadrature axes ($\psi_{m,d}$, $\psi_{m,q}$, $\psi_{s,d}$, $\psi_{s,q}$) can be calculated with

$$\begin{bmatrix}\psi_{m,d}\\ \psi_{m,q}\\ \psi_{s,d}\\ \psi_{s,q}\end{bmatrix} = \begin{bmatrix} L_d & 0 & M'_d x & -M'_d y \\ 0 & L_q & M'_q y & M'_q x \\ M'_d x & M'_q y & L_s & 0 \\ -M'_d y & M'_q x & 0 & L_s \end{bmatrix} * \begin{bmatrix} i_{m,d}\\ i_{m,q}\\ i_{s,d}\\ i_{s,q}\end{bmatrix} + \begin{bmatrix} \lambda_m \\ 0 \\ \lambda'_m x \\ -\lambda'_m y \end{bmatrix}, \tag{2.13}$$

where L_d is the motor d-axis inductance, L_q is the motor q-axis inductance, L_s is the suspension winding inductance, $i_{m,d}$ and $i_{m,q}$ are the motor drive winding currents, $i_{s,d}$ and $i_{s,q}$ are the suspension winding currents, and λ'_m and M'_d and M'_q are the suspension force constants (Chiba, 2005). This equation does not take into account magnetic saturation, rotor angle, eddy currents, and leakage fluxes. Now, the forces can be derived by using the stored magnetic coenergy W'_m

$$W'_m = W_m = \frac{1}{2}\begin{bmatrix} i_{m,d} & i_{m,q} & i_{s,d} & i_{s,q} \end{bmatrix} \begin{bmatrix} \psi_{m,d} \\ \psi_{m,q} \\ \psi_{s,d} \\ \psi_{s,q} \end{bmatrix}, \tag{2.14}$$

$$F_x = \frac{\partial W_m}{\partial x}, \tag{2.15}$$

$$F_y = \frac{\partial W_m}{\partial y}, \tag{2.16}$$

where W_m is the magnetic energy, being equal to the magnetic coenergy W'_m.

For a 4-pole interior permanent magnet (IPM) bearingless motor with 2-pole suspension and separate windings (Jastrzebski et al., 2015; Jaatinen et al., 2015), linearized forces are as follows. Assuming motor control for $i_{m,d} = 0$, adding the unbalance magnetic pull (UMP), and neglecting gravity, linearized forces F_x and F_y are ($\lambda'_m = k_i$)

$$\begin{bmatrix} F_x \\ F_y \end{bmatrix} = \begin{bmatrix} (k_{x1} + k_{x2} i_{m,q}) x \\ (k_{x1} + k_{x2} i_{m,q}) y \end{bmatrix} + \begin{bmatrix} \frac{1}{2} k_i & M'_q i_{m,q} \\ M'_q i_{m,q} & -\frac{1}{2} k_i \end{bmatrix} * \begin{bmatrix} i_{s,d} \\ i_{s,q} \end{bmatrix}, \tag{2.17}$$

where k_{x1} is the suspension position stiffness, and k_{x2} is the position stiffness on the suspension related to the q-axis motor drive current. This is comparable with AMBs; see Eq. (2.5).

2.3 Analytical modeling

Analytical modeling of AMBs has been discussed in (Hynynen, 2011; Jastrzebski et al., 2016). In (Jugo et al., 2008), analytical modeling of AMBs was performed in the harmonic domain. In (Wang et al., 2017), analytical modeling method of AMBs was shown taking into account the magnetic saturation. In (Romanenko et al., 2014), modeling of losses in an AMB using a reluctance network method of fluxes in a heteropolar 8-pole bearing was presented. In (Jastrzebski et al., 2019), modeling of radial and axial AMBs was shown with the 3D FEM. In this work, the AMBs were modeled with lookup tables, which were obtained from the FEM analysis of the AMB.

(Jastrzebski et al., 2018) presented modeling and optimization of a bearingless motor structure with the FEM. In (Jastrzebski et al., 2017a), modeling and control design simulations were presented for a linear flux-switching permanent-magnet-levitated motor.

2.4 Differences between AMBs and Permanent magnet bearingless machines

A bearingless motor actuator signal has an error angle (between the x and y-axes) resulting from permeability changes caused by slots and poles and magnetomotive force variations. For the nonrotating case, this translates into a dc offset error in the suspension force vector (Chiba, 2005). A comprehensive analysis of the suspension force error angle in a 10 kW bearingless test rig was presented in (Jaatinen, 2019). When rotating, there will be modulated harmonics of 20–24 times the rotational frequency, and the highest harmonic is four times the rotational frequency. For the mechanical model, there is no difference between AMB and bearingless machines. The bearingless machine also has a coupling between the actuators and the motor coils through mutual inductances. For AMBs, the xy forces are symmetrical for the rotor in the center position. For the 4-pole bearingless machine, the error angle was minimized in the machine design, and the forces are symmetrical if the error angle is not taken into account. For example, for a 2-pole rotor, there would have been significant differences between the x- and y-force vectors.

3 Rotor modeling

In this chapter, rotor modeling of AMB and bearingless machines is presented. Rigid and flexible rotor models are shown. The models are later compared with the identification results.

The modeling of rigid and flexible rotors can be started from Newton's II law of motion in a linearized case

$$\mathbf{M}\ddot{\mathbf{q}}(t) + (\mathbf{D}_\mathrm{M} + \Omega\mathbf{G}_\mathrm{M})\dot{\mathbf{q}}(t) + \mathbf{K}\mathbf{q}(t) = \mathbf{F}(t), \tag{3.1}$$

where $\mathbf{D}_\mathrm{M}$ is the damping matrix, $\mathbf{G}_\mathrm{M}$ is the gyroscopic matrix, $\mathbf{K}$ is the stiffness matrix, M is the mass matrix, Ω is the rotational speed, $\mathbf{q}$ is the displacement vector, and $\mathbf{F}$ is the force vector. This equation can be used assuming that the rotational speed is constant, displacements from the reference points are small, and the rotor is axisymmetric.

3.1 Rigid rotor model

In the rigid rotor, the critical frequencies are higher than the maximum rotational speed and the bandwidth of the position controller. In this case, a rigid rotor with two radial AMBs is considered. The model describes the rotor motion related to the center of the mass with the state vector $\mathbf{q} = \begin{bmatrix} x & y & \beta_x & \beta_y \end{bmatrix}^T$, where x and y denote displacements along the axes and β_x and β_y rotations around those axes. Thus, a four-degree-of-freedom (DOF) system is obtained. The fifth DOF is motion along the z-axis, but it is not coupled with the x- and y-axes, and it is controlled separately with an axial AMB. Rotation around the z-axis, which is the sixth DOF, is included as a multiplier in the gyroscopic ($\mathbf{G}_\mathrm{M}$) matrix. Some additional transformations are also required to shift the positions of the sensors and the actuators to the center of mass. The resulting equation of motion for the center of mass is

$$\mathbf{M}\ddot{\mathbf{q}} + \Omega\mathbf{G}_\mathrm{M}\dot{\mathbf{q}} = \mathbf{F}, \tag{3.2}$$

where the matrices $\mathbf{M}$, $\mathbf{G}_\mathrm{M}$, and $\mathbf{F}$ are constructed as

$$\mathbf{M} = \begin{bmatrix} m & 0 & 0 & 0 \\ 0 & m & 0 & 0 \\ 0 & 0 & I_x & 0 \\ 0 & 0 & 0 & I_y \end{bmatrix}, \ \mathbf{G}_\mathrm{M} = \begin{bmatrix} 0 & 0 & 0 & 0 \\ 0 & 0 & 0 & 0 \\ 0 & 0 & 0 & I_z \\ 0 & 0 & -I_z & 0 \end{bmatrix}, \ \mathbf{F} = \begin{bmatrix} f_x \\ f_y \\ \theta_x \\ \theta_y \end{bmatrix}, \tag{3.3}$$

where I_x is the transversal moment of inertia about the x-axis, I_y is the transversal moment of inertia about the y-axis, I_z is the z-axis rotational moment of inertia, f_x is the force acting in the x-direction, θ_x is the moment applied to the x-axis, and f_y and θ_y are the force and moment of the y-axis/direction, respectively. The outputs in the sensor locations are $\mathbf{q}_\mathrm{s} = \begin{bmatrix} x_\mathrm{s,A} & y_\mathrm{s,A} & x_\mathrm{s,B} & y_\mathrm{s,B} \end{bmatrix}^T$. This is demonstrated in Fig. 3.1.

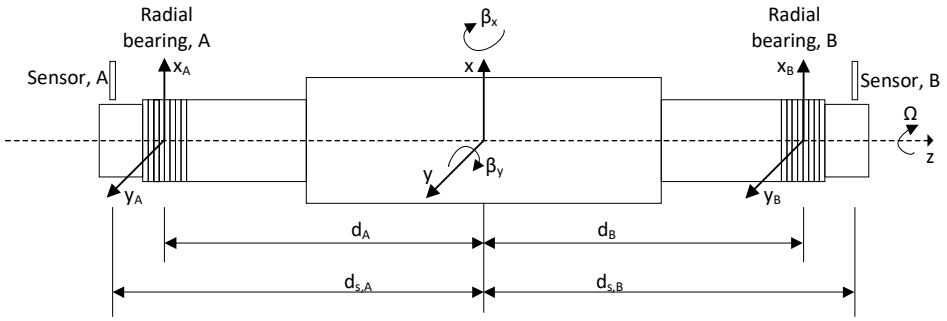

Figure 3.1. Rigid rotor coordinate systems.

An equation similar to the one written for the center of mass (Eq. (3.2)) can be given in the bearing coordinates

$$\mathbf{M}_\mathrm{b}\ddot{\mathbf{q}}_\mathrm{b} + \Omega\mathbf{G}_\mathrm{b}\dot{\mathbf{q}}_\mathrm{b} = \mathbf{K}_\mathrm{x}\mathbf{q}_\mathrm{b} + \mathbf{K}_\mathrm{i}\mathbf{i}_\mathrm{c}, \tag{3.4}$$

where the subscript b denotes the bearing coordinates $\mathbf{q}_\mathrm{b} = \begin{bmatrix} x_\mathrm{A} & y_\mathrm{A} & x_\mathrm{B} & y_\mathrm{B} \end{bmatrix}$, and x_A is the x-axis displacement in bearing A; similarly, y_A is the y-axis displacement in bearing A, x_B and y_B are the x- and y-axis displacements in bearing B, respectively,
and $\mathbf{i}_\mathrm{c} = \begin{bmatrix} i_\mathrm{c,x,A} & i_\mathrm{c,y,A} & i_\mathrm{c,x,B} & i_\mathrm{c,y,B} \end{bmatrix}$ is the control current vector denoting the currents of the electromagnets in bearings A and B in the x- and y-directions. The transformations from the center of gravity coordinates to the bearing coordinates are made with

$$\begin{aligned} \mathbf{q}_\mathrm{b} &= \mathbf{T}_1\mathbf{q}, \quad & \mathbf{G}_\mathrm{b} &= \mathbf{T}_2^T\mathbf{G}_\mathrm{M}\mathbf{T}_2, \; \mathbf{M}_\mathrm{b} = \mathbf{T}_2^T\mathbf{M}\mathbf{T}_2, \\ \mathbf{q}_\mathrm{s} &= \mathbf{T}_\mathrm{s}\mathbf{q}, & \mathbf{T}_2 &= \mathbf{T}_1^{-1}, \end{aligned} \tag{3.5}$$

where the subscript s denotes the sensor coordinate system. The transformation matrices are

$$\mathbf{T}_1 = \begin{bmatrix} 1 & 0 & 1 & 0 \\ 0 & 1 & 0 & 1 \\ 0 & -d_\mathrm{A} & 0 & d_\mathrm{B} \\ -d_\mathrm{A} & 0 & d_\mathrm{B} & 0 \end{bmatrix}, \; \mathbf{T}_\mathrm{s} = \begin{bmatrix} 1 & 0 & 1 & 0 \\ 0 & 1 & 0 & 1 \\ 0 & -d_\mathrm{s,A} & 0 & d_\mathrm{s,B} \\ -d_\mathrm{s,A} & 0 & d_\mathrm{s,B} & 0 \end{bmatrix}, \tag{3.6}$$

where d is the distance from the sensor to the center of mass or the distance from the center of mass to the corresponding bearing (see Fig. 3.1).

3.2 Flexible rotor model

In the flexible rotor, the critical frequencies are lower than the maximum rotational speed, they can be affected by the position controller, and may be exceeded during run-down

and run-up. Flexible rotors are modeled by dividing them into a finite set of similar elements, which is known as FEM modeling. Usually, rotors are divided into 20–40 elements. Rotors are typically modeled with cylinders described as Timoshenko beam elements (Timoshenko, 1921, 1922). The benefit of using Timoshenko beam elements is that both the rotational inertia and the shear deformation are taken into account, which is useful for short and thick rotors. Each element can be expressed as

$$\mathbf{M}_i\ddot{\mathbf{q}}_i + (\mathbf{D}_i + \Omega\mathbf{G}_i)\dot{\mathbf{q}}_i + \mathbf{K}_i\mathbf{q}_i = \mathbf{F}_i, \tag{3.7}$$

where $\mathbf{D}_\mathrm{i}$ is the damping matrix, $\mathbf{G}_\mathrm{i}$ is the gyroscopic matrix, $\mathbf{K}_\mathrm{i}$ is the stiffness matrix, $\mathbf{M}_\mathrm{i}$ is the mass matrix, Ω is the rotational speed, $\mathbf{F}_\mathrm{i}$ is the force vector, and $\mathbf{q}_i = \begin{bmatrix} x_i & y_i & \beta_{x,i} & \beta_{y,i} \end{bmatrix}^T$ is the state vector. The matrix structure is the same as shown in Eq. (3.3); however, now the subscript i denotes the number of elements. An example of the Timoshenko beam element and coordinate systems in the flexible rotor modeling is shown in Fig. 3.2.

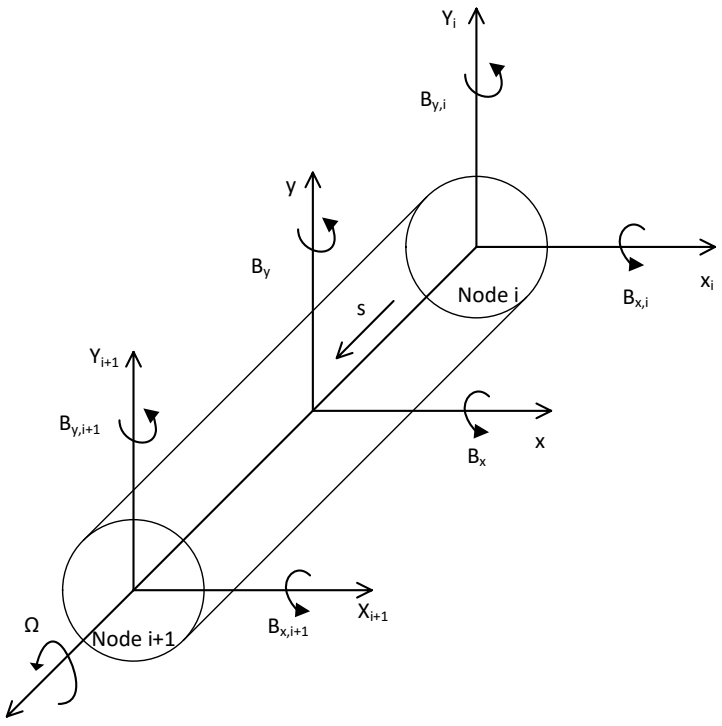

Figure 3.2. Timoshenko beam element and coordinates.

In the global coordinate system applying the shape function matrix $\mathbf{N}$, the final shape of

the rotor is

$$\mathbf{q}_i^{\mathrm{g}} = \mathbf{N}(s)\mathbf{q}_i, \tag{3.8}$$

where the superscript g denotes the global coordinate system, and s is the longitudinal coordinate of each node. Now, the equation of motion for the rotor can be written as

$$\mathbf{M}^{\mathrm{g}}\ddot{\mathbf{q}}^{\mathrm{g}} + (\mathbf{D}^{\mathrm{g}} + \Omega\mathbf{G}^{\mathrm{g}})\dot{\mathbf{q}}^{\mathrm{g}} + \mathbf{K}\mathbf{q}^{\mathrm{g}} = \mathbf{F}^{\mathrm{g}}, \tag{3.9}$$

where $\mathbf{q}^{\mathrm{g}} = \begin{bmatrix}\mathbf{q}_1^{\mathrm{g}} & \mathbf{q}_2^{\mathrm{g}} & \cdots & \mathbf{q}_P^{\mathrm{g}}\end{bmatrix}^T$ is the global displacement vector. However, Eq. (3.9) has a high number of state variables, as it is the number of degrees of freedom multiplied by the number of elements used for modeling of the rotor. Therefore, it is necessary to reduce the number of state variables for the control purposes by using model reduction techniques. Typically, only the first few flexible modes are necessary. Transferring Eq. (3.9) into a modal one (Smirnov, 2012) gives

$$\mathbf{M}^{\mathrm{m}}\ddot{\mathbf{q}}^{\mathrm{m}} + (\mathbf{D}^{\mathrm{m}} + \Omega\mathbf{G}^{\mathrm{m}})\dot{\mathbf{q}}^{\mathrm{m}} + \mathbf{K}\mathbf{q}^{\mathrm{m}} = \mathbf{F}^{\mathrm{m}}. \tag{3.10}$$

The coordinate transformation is carried out with

$$\mathbf{q}^{\mathrm{g}} = \boldsymbol{\Phi}^{\mathrm{m}}\mathbf{q}^{\mathrm{m}}, \tag{3.11}$$

where $\boldsymbol{\Phi}^{\mathrm{m}}$ is the reduced mode shape function matrix in modal coordinates. Typically, the mode shape function matrix is scaled so that the modal mass matrix becomes an identity matrix $\mathbf{M}^{\mathrm{m}} = (\boldsymbol{\Phi}^{\mathrm{m}})^T\mathbf{M}\,\boldsymbol{\Phi}^{\mathrm{m}} = \mathbf{I}$. The matrices $\mathbf{M}^{\mathrm{m}}$, $\mathbf{D}^{\mathrm{m}}$, $\mathbf{G}^{\mathrm{m}}$, $\mathbf{K}^{\mathrm{m}}$, $\mathbf{F}^{\mathrm{m}}$ are obtained by the following transformations

$$\begin{aligned}
&\mathbf{M}^{\mathrm{m}} = (\boldsymbol{\Phi}^{\mathrm{m}})^T\mathbf{M}\,\boldsymbol{\Phi}^{\mathrm{m}}, \quad && \mathbf{K}^{\mathrm{m}} = (\boldsymbol{\Phi}^{\mathrm{m}})^T\mathbf{K}\,\boldsymbol{\Phi}^{\mathrm{m}},\\
&\mathbf{G}^{\mathrm{m}} = (\boldsymbol{\Phi}^{\mathrm{m}})^T\mathbf{G}\,\boldsymbol{\Phi}^{\mathrm{m}}, && \mathbf{D}^{\mathrm{m}} = (\boldsymbol{\Phi}^{\mathrm{m}})^T\mathbf{D}\,\boldsymbol{\Phi}^{\mathrm{m}},\\
&\mathbf{F}^{\mathrm{m}} = (\boldsymbol{\Phi}^{\mathrm{m}})^T\mathbf{F}\,\boldsymbol{\Phi}^{\mathrm{m}}.
\end{aligned} \tag{3.12}$$

3.3 Overall plant model

First, combining the linearized forces provided by the electromagnets with the equation of motion for the flexible rotor yields

$$\mathbf{M}^{\mathrm{m}}\ddot{\mathbf{q}}^{\mathrm{m}} + (\mathbf{D}^{\mathrm{m}} + \Omega\mathbf{G}^{\mathrm{m}})\dot{\mathbf{q}}^{\mathrm{m}} + (\mathbf{K}^{\mathrm{m}} + \mathbf{K}_{\mathrm{x}}^{\mathrm{m}})\mathbf{q}^{\mathrm{m}} = \mathbf{K}_{\mathrm{i}}^{\mathrm{m}}\mathbf{i}_{\mathrm{c}}, \tag{3.13}$$

where $\mathbf{K}_{\mathrm{i}}^{\mathrm{m}}$ and $\mathbf{K}_{\mathrm{x}}^{\mathrm{m}}$ are the translated current and position stiffnesses to the center of mass. They can be obtained with

$$\begin{aligned}
\mathbf{K}_{\mathrm{i}}^{\mathrm{m}} &= (\boldsymbol{\Phi}^{\mathrm{m}})^T\mathbf{S}_{\mathrm{a}}\mathbf{K}_{\mathrm{i}}\,\boldsymbol{\Phi}^{\mathrm{m}},\\
\mathbf{K}_{\mathrm{x}}^{\mathrm{m}} &= (\boldsymbol{\Phi}^{\mathrm{m}})^T\mathbf{S}_{\mathrm{a}}(-\mathbf{K}_{\mathrm{x}})\,\boldsymbol{\Phi}^{\mathrm{m}},
\end{aligned} \tag{3.14}$$

where $\mathbf{S}_{\mathrm{a}}$ includes the position of the actuators and $\mathbf{S}_{\mathrm{s}}$ the position of the sensors.

Equation (3.13) is expressed in the state space form

$$\begin{aligned}\dot{\mathbf{x}}_\mathrm{r} &= \mathbf{A}_\mathrm{r}\mathbf{x}_\mathrm{r} + \mathbf{B}_\mathrm{r}\mathbf{u},\\ \mathbf{y}_\mathrm{r} &= \mathbf{C}_\mathrm{r}\mathbf{x}_\mathrm{r} + \mathbf{D}_\mathrm{r}\mathbf{u},\end{aligned} \tag{3.15}$$

where the matrices $\mathbf{A}_\mathrm{r}$, $\mathbf{B}_\mathrm{r}$, $\mathbf{C}_\mathrm{r}$, $\mathbf{D}_\mathrm{r}$ are

$$\begin{aligned}\mathbf{A}_\mathrm{r} &= \begin{bmatrix}\mathbf{0} & \mathbf{I}\\ -(\mathbf{M}^\mathrm{m})^{-1}(\mathbf{K}^\mathrm{m}+\mathbf{K}_\mathrm{x}^\mathrm{m}) & -(\mathbf{M}^\mathrm{m})^{-1}(\mathbf{D}^\mathrm{m}+\Omega\mathbf{G}^\mathrm{m})\end{bmatrix},\\ \mathbf{B}_\mathrm{r} &= \begin{bmatrix}\mathbf{0}\\ -(\mathbf{M}^\mathrm{m})^{-1}\mathbf{K}_\mathrm{i}^\mathrm{m}\end{bmatrix},\ \mathbf{C}_\mathrm{r} = \begin{bmatrix}\mathbf{S}_\mathrm{s}\boldsymbol{\Phi}^\mathrm{m} & \mathbf{0}\end{bmatrix},\ \mathbf{D}_\mathrm{r} = \mathbf{0}.\end{aligned} \tag{3.16}$$

The system inputs are the control currents for the bearings $\mathbf{u} = \begin{bmatrix} i_{\mathrm{c,x,A}} & i_{\mathrm{c,y,A}} & i_{\mathrm{c,x,B}} & i_{\mathrm{c,y,B}}\end{bmatrix}^T$, the outputs are the rotor positions $\mathbf{y}_\mathrm{r} = \begin{bmatrix} x_\mathrm{A} & y_\mathrm{A} & x_\mathrm{B} & y_\mathrm{B}\end{bmatrix}$, and the states $\mathbf{x}_\mathrm{r}$ combine the modal positions and the velocity $\mathbf{x}_\mathrm{r} = \begin{bmatrix}\mathbf{q} & \dot{\mathbf{q}}\end{bmatrix}^T$.
Now, for the overall model, the reduced rotor model is combined with the linearized actuator dynamics

$$\begin{aligned}\dot{\mathbf{x}} &= \mathbf{A}\mathbf{x} + \mathbf{B}\mathbf{u},\\ \mathbf{y} &= \mathbf{C}\mathbf{x} + \mathbf{D}\mathbf{u},\end{aligned} \tag{3.17}$$

$$\begin{aligned}\mathbf{A} &= \begin{bmatrix}\mathbf{A}_\mathrm{a} & \mathbf{0}\\ \mathbf{B}_\mathrm{r}\mathbf{C}_\mathrm{a} & \mathbf{A}_\mathrm{r}\end{bmatrix},\ \mathbf{B} = \begin{bmatrix}\mathbf{B}_\mathrm{a}\\ \mathbf{0}\end{bmatrix},\\ \mathbf{C} &= \begin{bmatrix}\mathbf{0} & \mathbf{C}_\mathrm{r}\end{bmatrix},\ \mathbf{D} = \mathbf{0},\end{aligned} \tag{3.18}$$

where the state vector $\mathbf{x}$ combines the states of both the actuator and the rotor $\mathbf{x} = \begin{bmatrix}\mathbf{x}_\mathrm{a} & \mathbf{x}_\mathrm{r}\end{bmatrix}^T$. The subscript r denotes the rotor part and the subscript a the actuator part. The actuator matrices are diagonal $\mathbf{B}_\mathrm{a} = -\mathbf{A}_\mathrm{a} = \mathrm{diag}(\begin{bmatrix}\omega_{bw} & \omega_{bw} & \omega_{bw} & \omega_{bw}\end{bmatrix})$ and $\mathbf{C}_\mathrm{a} = \mathbf{I}_{4\mathrm{x}4}$. A simple linearization shown in Eq. (2.11) is used for each channel.

The presented overall plant model, however, contains mostly linear relations, and there are some unmodeled dynamics. In reality, the relations are nonlinear, and for example the force of an electromagnet is highly nonlinear (Eq. 2.1). The power amplifier also has some dynamics, for instance a varying gain based on frequency. The same holds for the sensors. There may also be a coupling between the radial and axial bearings and an x-y coupling through actuators. Some unmodeled dynamics are for instance foundations, shrink fits, and seals. The overall plant model is usually only a best guess and must be updated based on the system identification results from a real machine.

The flexible rotor models were obtained by using RoBeDyn MATLAB toolbox. The

models are later compared with the identification results.

4 System identification

In this chapter, the system identification theory is discussed. SISO and MIMO AMB and bearingless machine identification is presented.

4.1 Frequency domain identification

The system identification of magnetically levitated systems is usually carried out in the frequency domain. The identification must be carried out in a closed loop as the system is unstable without a controller.

4.1.1 Closed-loop identification

In the closed-loop identification, the effect of the controller is also included in the measured frequency response functions (FRFs). There are three closed-loop identification approaches: the first is the direct approach, which is typically used during initial identification or when there is no information of the feedback. In the direct approach, the effect of the controller is omitted and the open-loop model is calculated directly from the plant input $u(k)$ and output signals $y(k)$

$$G_0(\mathrm{j}\omega_k) = \frac{Y(\omega_k)}{U(\omega_k)}. \tag{4.1}$$

The second approach is the indirect approach. In the indirect approach, the effect of the controller is taken into account. However, the indirect approach is sensitive to errors in the controller transfer function, such as deviation from a linear regulation. In the indirect approach, the open-loop model is calculated from the closed-loop transfer function $G_{\mathrm{cl}}(\mathrm{j}\omega_k)$ between the measured plant output $y(k)$ and the excitation signal $w(k)$ when the controller model is known

$$G_0(\mathrm{j}\omega_k) = \frac{G_{\mathrm{cl}}(\mathrm{j}\omega_k)}{1 - G_{\mathrm{cl}}(\mathrm{j}\omega_k)C_0(\mathrm{j}\omega_k)}. \tag{4.2}$$

The third approach is the joint-input-output approach. With this method, both the plant and feedback dynamics can be identified. A disadvantage is that knowledge of the reference signal is needed. In the joint-input-output approach, the excitation signal $w(k)$ is the system input, and the plant input $u(k)$ and the plant output $y(k)$ are considered system outputs

$$G_0(\mathrm{j}\omega_k) = \frac{Y(\omega_k)R(\omega_k)^H}{U(\omega_k)R(\omega_k)^H}, \tag{4.3}$$

where $R(\omega_k)$ is the reference signal. A block diagram for these different closed-loop

identification approaches is presented in Fig. 4.1.

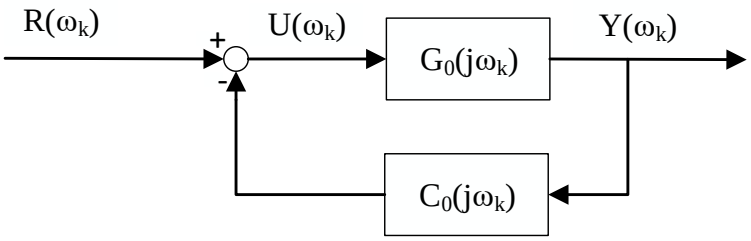

Figure 4.1. Plant ($G_0(j\omega_k)$) identification with feedback controller ($C_0(j\omega_k)$) . $R(\omega_k)$ is the reference signal, $U(\omega_k)$ is the measured input and $Y(\omega_k)$ is the measured output.

In this dissertation, the direct approach is mainly used. The indirect approach is employed only in **Publication II**.

4.1.2 Sliding discrete Fourier transform (SDFT)

Discrete Fourier transform is a way of determining discrete-time signal's frequency spectrum. This however is a complex operation and requires the summing and multiplication of all the measurement samples over a full measurement window with an exponential function. An alternative for DFT is the SDFT algorithm which works on sample-by-sample basis utilizing a sliding window and is suitable for real-time spectral analysis. Within a period of N samples, at a specific time instant n the k^{th}-order harmonic is obtained with

$$X_k(n) = \sum_{l=0}^{N-1} x(n-(N-1)+l)e^{-\mathrm{j}k(2\pi/N)l}. \tag{4.4}$$

The SDFT's basic form can be derived from Eq. (4.4) as (Jacobsen and Lyons, 2003)

$$X_k(n) = (X_k(n-1) + x(n) - x(n-N))e^{\mathrm{j}k(2\pi/N)}. \tag{4.5}$$

The Eq. (4.5) shows the main principle of the SDFT. The SDFT uses a moving window where the calculation of a new DFT bin is calculated from the previous DFT result. Figure 4.2 illustrates the implementation and the principle of the SDFT. The computational efficiency of the SDFT is based on that at each time instant n, from the window, the oldest measurement sample is removed and the newest sample is added to the sum as shown in

Fig. 4.2a. The SDFT tracks the signals used in the identification as depicted in Fig. 4.2b. For the SDFT, the most suitable excitation signal would be multisine that would have the same excitation frequencies that are tracked with the SDFT.

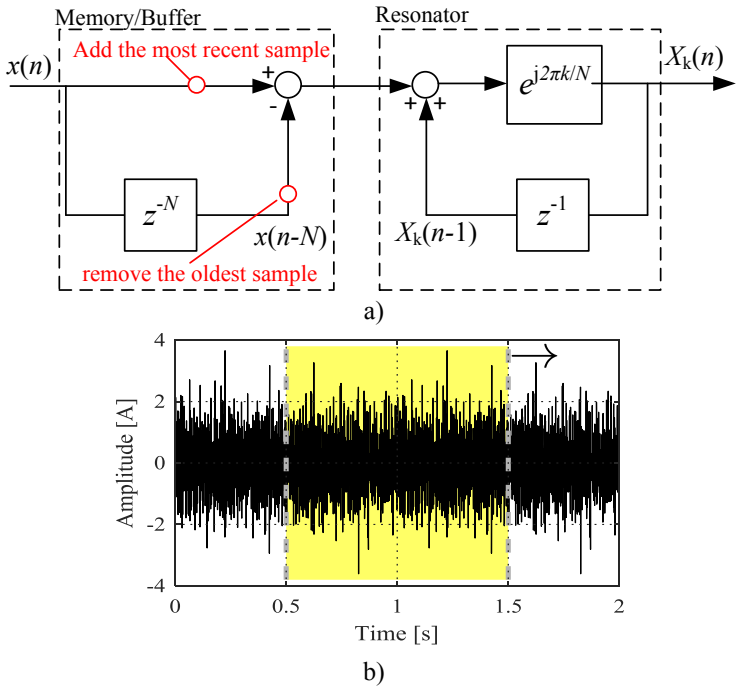

Figure 4.2. Principle of the SDFT; a) implementation and b) demonstration of the SDFT window (yellow region) plotted over two periods of the multisine excitation signal in the time domain. (From **Publication III**).

4.1.3 Offline vs. online identification

Offline identification is the traditional way of identification. In the offline identification, the identification data are postprocessed offline. Typically, data are processed with the fast Fourier transform (FFT), which is a computationally efficient way of calculating DFT. Here, the benefit compared with the online identification is that all of the frequency components are analyzed with the FFT. Offline identification is suitable for initial identification and for example updating the FEM model.

Online identification is the other way of identification. In the online identification, the data are processed online. FFT is not suitable for online identification because it requires recalculation of the whole Fourier transform, requiring too many calculations after the data are modified. Here, the SDFT is used for the online identification, which works on a sample-by-sample basis using a moving window and is suitable for online identification.

Typically, not all of the frequencies are tracked with SDFT, which is the key difference between online and offline identification. The resolution depends on the selected samples N, and can be chosen freely. With a large N, a resolution comparable with offline identification is achieved. The online identification is suitable for diagnostics and tracking frequencies of interest such as the critical frequencies.

4.2 Excitation signals

Selection of the excitation signal is an important part of the system identification. This selection is usually based on prespecified criteria and the type of the identification problem (Pintelon and Schoukens, 2012). This dissertation studies closed-loop identification of magnetically levitated systems using various excitation signals. A pseudorandom binary sequence (PRBS) excitation signal is used in **Publication I**, **II**, **IV**, and **V**, chirp or swept sine in **Publication IV**, multisine in **Publication III** and **IV**, and stepped sine in **Publication I**, **II**, **IV**, and **VI**.

4.2.1 Pseudorandom binary sequence (PRBS)

Pseudorandom binary sequence (PRBS) presented in Fig. 4.3a is an identification excitation signal that alters between two levels; amplitudes -A and +A. Properties of the PRBS include: it's generation is easy and the PRBS is periodic and deterministic. The PRBS also has an optimal spectrum for the excitation signal, a controllable spectral energy and a high spectral energy over a wide band range. The basic PRBS is defined by the selected excitation frequency f and the number of cells d. The length N of the PRBS is obtained with

$$N = 2^d - 1. \tag{4.6}$$

The frequency resolution f_r of the PRBS is expressed as

$$f_r = \frac{f_s}{N}. \tag{4.7}$$

where f_s is the sampling frequency. The PRBS identification data needs L data points for saving

$$L = \frac{N f_s}{f}. \tag{4.8}$$

The maximum length N is limited by the maximum available L and the ratio of the sampling and excitation frequency f_s/f, as shown in Eq. (4.8). If you want to increase the frequency resolution f_r defined by Eq. (4.7) it can be accomplished with a lower N, a higher f and a higher f_s.

4.2.2 Chirp

A chirp signal (see Fig. 4.3b), is an identification excitation signal in which the frequency either increases or decreases in one period. It's also known as a sweep or swept signal. There are typically two groups the chirp signals are divided into: exponential/geometrical and linear. In the exponential/geometrical group the frequency varies geometrically and in the linear group linearly with time. In this dissertation, a linear chirp signal with a sinusoidal waveform is applied. Linear chirp signal's instantaneous frequency $f(t)$ is express as

$$f(t) = f_0 + kt, \tag{4.9}$$

where f_0 is the start frequency, k is the rate of frequency change and t is the current time. The rate of frequency change k is obtained with

$$k = \frac{f_1 - f_0}{T}, \tag{4.10}$$

where f_1 is the end frequency and T is the end time after the the frequency change from f_0 to f_1 (either increasing or decreasing). The equation of the linear sine chirp signal is (Pintelon and Schoukens, 2012)

$$u(t) = A \cdot \sin\Big(2\pi \cdot \big(f_0 t + \frac{k}{2} t^2\big)\Big), \tag{4.11}$$

where A is the amplitude of the chirp signal. With chirp signal the frequency content of the signal can be somewhat controlled. In the case of AMB system identification, chirp signals have been used in (Inman et al., 2005; Lanzon and Tsiotras, 2005).

4.2.3 Multisine

A multisine signal illustrated in Fig. 4.3c, is obtained with

$$u(t) = \sum_{n=1}^{N_\mathrm{f}} A_n \cdot \cos(2\pi f_n t + \phi_n), \tag{4.12}$$

where N_f is the total number of frequencies over n indices, A_n is the amplitude, f_n is the frequency, and ϕ_n is the phase of the n^{th} sine wave component. The phases of these sine wave components are randomly chosen from the interval [0, 2π]. The multisine signals used in the AMB system identification must be designed so that the frequency spectrum of the signal avoids the harmonics produced by the nonlinearities of the system as discussed in (Hynynen and Jastrzebski, 2009; Hynynen et al., 2010). In this dissertation similar guidelines are adopted and the multisine signal used consist of four bands where for each

band the frequency resolution, the start and end frequencies and the amplitudes can be chosen freely.

4.2.4 Stepped sine

A single sine wave has all of its power at one frequency only. In order to cover the whole frequency range, several sine waves with different frequencies and amplitudes are excited separately. This is known as a stepped sine depicted in Fig. 4.3d. In general, the amplitude A_n and the frequency f_n can be chosen freely for each sine wave. The stepped sine wave is described with the following equation

$$u(t) = A_n \cdot \sin\Big(2\pi f_n t\Big). \tag{4.13}$$

In this dissertation an adaptive amplitude stepped sine is used. In the adaptive amplitude stepped sine the frequency f_n is selected freely and in order to keep the magnetically levitated system in the linear region and to get an acceptable response the amplitude A_n adjusted between prespecified limits (Smirnov, 2012).

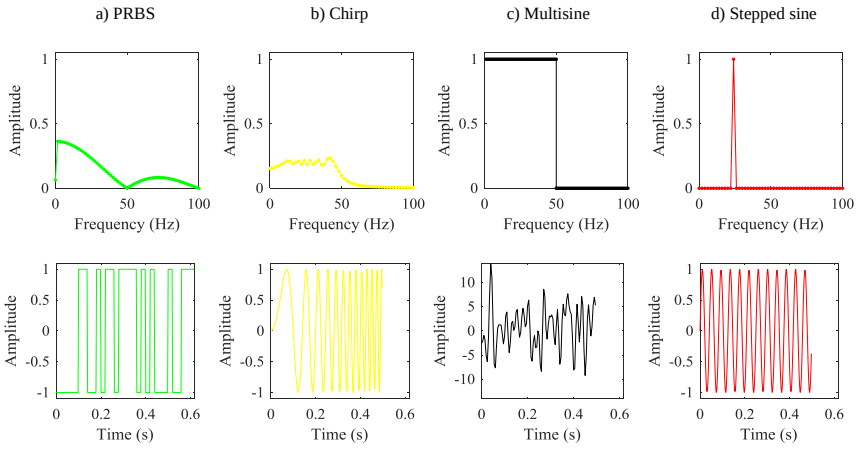

Figure 4.3. Excitation signal comparison in the frequency domain (upper row) and the time domain (bottom row). (From **Publication IV**).

4.2.5 Comparison of the excitation signal properties

Table 4.1 shows a comparison of the excitation signal properties presented in the previous sections. In general, the PRBS is the best option for initial identifications, where the SNR is not the most important criterion and fast identifications are preferred. For more accurate identification, either multisine or stepped sine is required.

Table 4.1. Summary of the comparison of different excitation signals with respect to their embedded implementation in an AMB system. (*) individual excitation frequencies and amplitudes can be controlled.

	PRBS	Chirp	Multisine	Stepped sine
Complexity	low	med	high	med
Execution time	short	short	short	long
Memory consumption	high	high	high	low
SNR	low	med	med	high
Controllability of excitation frequency	low	low	high*	high*
Controllability of excitation amplitude	low	low	high*	high*

4.3 Special cases in the magnetically levitated system identification

The identification of magnetically levitated systems must be carried out in a closed loop. The identification must also be carried out when the rotor is levitating in a stable position. It should be noted that a rotor-stator contact must be avoided as it would falsify the identification results (Schweitzer and Maslen, 2009). There are several transfer functions that can be identified from AMB systems, such as the open-loop plant (rotor model/rotor–bearing system), controller, input sensitivity, output sensitivity, and inner current control loop (ISO 14839-3, 2006). In this dissertation, the focus is on the inner current control loop and rotor–bearing system identification.

4.3.1 Inner current control loop

In the current control loop identification, the effect of the reference control current on the measured coil current is identified. Typically, the inner current control loop is approximated as a first-order system, presented in Eq. (2.11). The inner current control loop identification is shown in Fig. 4.4a. In this dissertation, the SISO inner current control loop identification is used in **Publication I** and **IV**.

4.3.2 Rotor–bearing system

Rotor–bearing system identification is used for control design purposes and to verify the accuracy of the rotor model and rotor–bearing dynamics. The rotor model consists mainly of mechanical resonances and antiresonances. Figure 4.4b shows the block diagram of the rotor–bearing system identification. The rotor–bearing system identification can be carried out in a SISO or MIMO loop. The SISO loop identification is useful for initial iden-

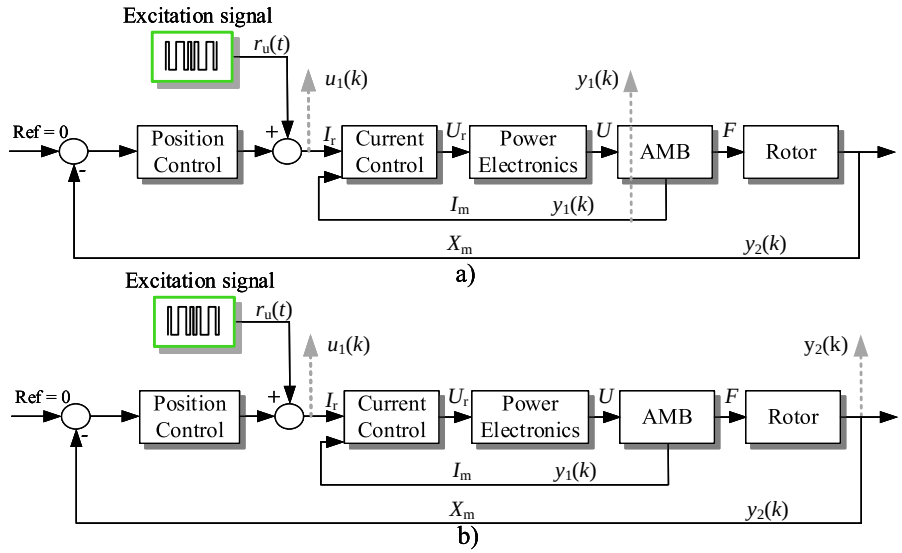

Figure 4.4. Block diagram of the AMB system with input and output signals used in the identification (dotted grey lines); a) identification of the bearing (inner current control loop) dynamics using the current reference signal $u_1(k)$ and the measured current $y_1(k)$ and b) identification of the rotor–bearing system model using the current reference signal $u_1(k)$ and the measured position signal $y_2(k)$. (Adapted from **Publication IV**).

tification as it cannot identify the coupling between the axes. The single-input multiple output (SIMO) is an alternative to the SISO identification, and it can show some effects of the coupling because now all the outputs are measured. The MIMO identification is the best option if accurate results of the cross coupling between the axes are required.

In this dissertation, the SISO rotor–bearing system identification is used in **Publication I**, **II**, **IV**, and **VI**, the SIMO identification in **Publication III**, and the MIMO identification in **Publication V**.

4.3.3 Disturbances in the measured data

Usually, the measurement data contain disturbances. In the case of AMB systems there are several sources of disturbances in the measured data; for example, sensors and actuator surfaces have always some runout. A further source of disturbances is the mechanical tolerances in the manufactured prototypes, in particular, air gaps and clearances. Again, a nonconcentric assembly and the motor can cause disturbances to the measured data. Other sources of disturbances are gravity and loads, such as impellers and flywheels. Thermal effects (dimension and resistance changes) can also cause disturbances. The effect of nearby power amplifiers and electromagnetic fields on sensor signals as well as the effect of base/ground vibrations are also sources of disturbances. Finally, plant dynamics will change over time as a result of aging, reassembly, and other reasons.

5 Experimental results

In this chapter, system identification results are presented. Details of the test rigs used in this work are given.

The results of the inner current control loop and rotor–bearing system identification presented here are used to tune the control model applied to the controller synthesis. The results could also be used during the run time for the diagnostics of the system. Measurement data were detrended before the identification tests.

The position measurement is constructed of oversampled analog position input signals sampled at 100 kHz, and five measurements are then averaged. This results in a bandwidth of 9 kHz. The current measurement has a bandwidth of 7 kHz.

There are several sources of uncertainties in the measurement signals and the identification results. One source of uncertainty is the position sensor. The position sensor used in the 10 kW AMB test rig is SKF's CMSS 65-002-RM-12-5A eddy current sensor. In the product specifications, this sensor has excellent properties, such as linearity of +-25.4 μm. However, when assembled to the AMB system, the sensor calibration (sensor gain and offset) based on the assumed clearance will increase the uncertainty. The sensor calibration has been discussed in (Smirnov, 2012; Webster and Eren, 2014). Further, the manufacturing tolerances, electrical noise, and switching are sources of uncertainty. Other sources of uncertainties in the measurement signals and the identification results are the runout of the sensor and actuator surfaces. The rotor angle is also a source of uncertainty especially in the 10 kW AMB test rig, where there was no angle measurement and the angle was unknown between the measurements. Temperature also causes uncertainty because of the thermal expansion. This is most relevant to the HERGE test rig, where there are considerable temperature differences between the hot and cold machine. In HERGE, the rotor mass is 265 kg, and the rotor dimensions are relatively large compared with the air gaps of the AMBs. Finally, the current control of the actuator and the current measurement accuracy also cause uncertainty.

The measurements were not statistically analyzed, as it would require many additional measurements in the same conditions and be very time consuming. However, a statistical analysis is planned to be carried out in a future study. This statistical analysis could be used for example for monitoring and diagnostics of the system.

5.1 10 kW AMB test rig

The first test rig consists of two standard radial AMBs, an axial AMB, and a 10 kW 30,000 rpm induction motor. The sampling frequency is $f_s = 20$ kHz. This test rig is discussed in more detail in **Publication II**. The 10 kW AMB test rig is shown in Fig. 5.1.

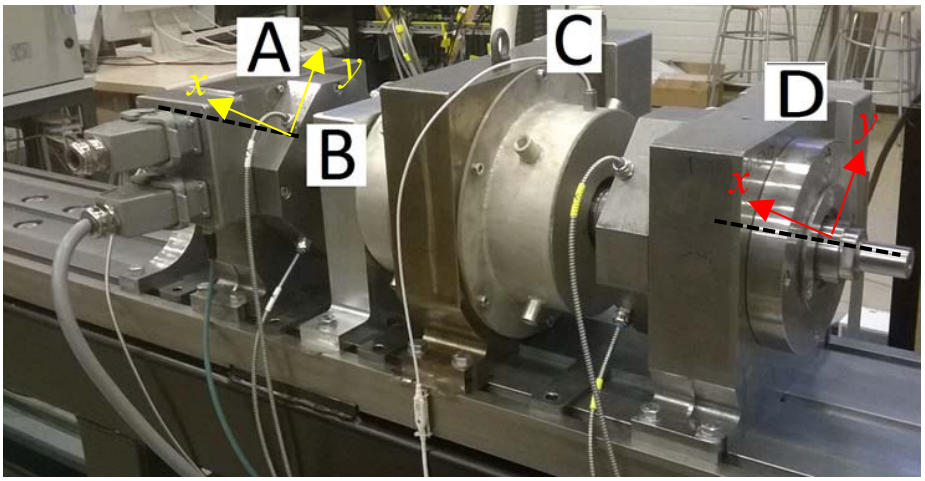

Figure 5.1. 10 kW AMB test rig; a) radial bearing non-drive-end, b) axial bearing, c) induction motor, and d) radial bearing drive-end. (From **Publication IV**).

First, the simulation results with the 10 kW AMB test rig are illustrated in Fig. 5.2. The time span from 0 to 0.2 s shows the simulated lift-up and the +100 μm position reference given on the drive-end x-axis (DX). Then, from 0.2 s to 2.7 s, the excitation on the drive-end x-axis with the PRBS is depicted. Finally, from 2.7 s to 3.0 s, the steady state is shown.

Next, the results of the inner current control loop are presented. PRBS, chirp, multisine, and stepped sine excitation signals with the following properties are used.

- The PRBS excitation signal has a frequency of $f = 3.33$ kHz with $d = 11$ cells and an amplitude of 2.5 A, resulting in a frequency resolution of $f_r = 1.63$ Hz. Ten periods are collected with the maximum of one second per period.
- The chirp excitation signal has a start frequency of $f_0 = 5$ Hz, an end frequency of $f_1 = 1$ kHz, and an amplitude of 1 A. The end time is $T = 1$ s. Ten periods are collected with the maximum of one second per period.
- The multisine excitation signal has the following four bands, and ten periods with the maximum of one second per period are collected:
  1. From 1 Hz to 19 Hz with 2 Hz steps and a 10 mA amplitude.
  2. From 23 Hz to 200 Hz with 4 Hz steps and a 50 mA amplitude.
  3. From 203 Hz to 399 Hz with 2 Hz steps and an 80 mA amplitude.
  4. From 403 Hz to 698 Hz with 5 Hz steps and a 120 mA amplitude.
- The adaptive amplitude stepped sine excitation signal has a frequency range from 1 Hz to 750 Hz with the maximum amplitude of 2.5 A and 250 frequency points, resulting in a frequency resolution of $f_r = 3.01$ Hz.

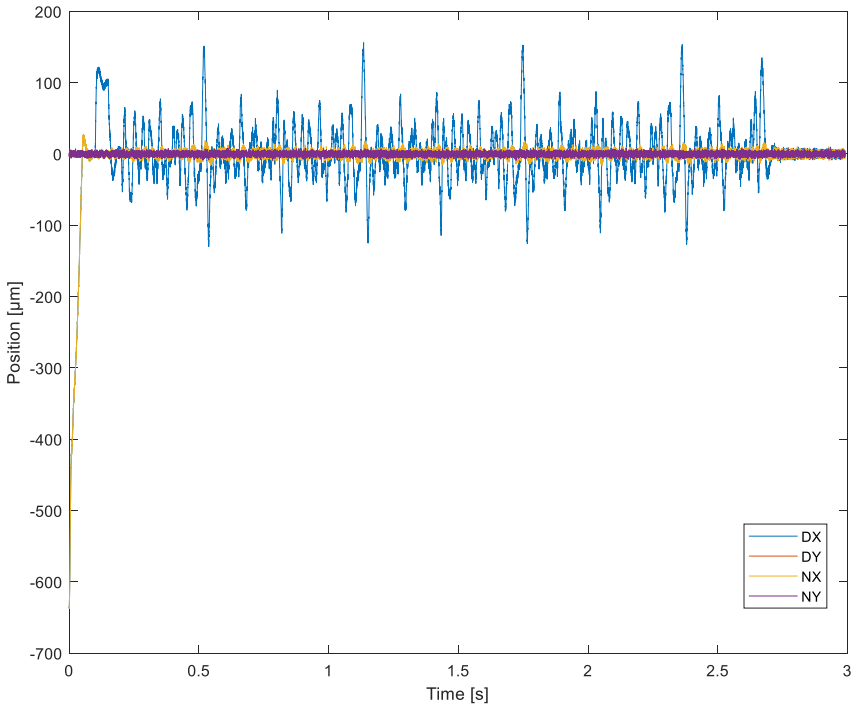

Figure 5.2. Simulation results with the 10 kW AMB test rig. DX and DY are the drive-end x-axis and y-axis, respectively. NX and NY are the non-drive-end x-axis and y-axis, respectively.

Fig. 5.3 presents the results of the inner current control loop identification. It can be seen that all the excitation signals show good correspondence with the approximated inner current control loop model. However, in the frequency region below 100 Hz there are variations between the excitation signals. This is a result of the excitation signal amplitudes in this specific region.

Next, the results of the rotor–bearing system are presented. The same excitation signals are used as previously. Fig. 5.4 presents the results of the rotor–bearing system identification. The results show that all the excitation signals provide a good accuracy compared with the FEM model on the slope up to the first resonance frequency (10 Hz to 280 Hz) on the drive-end x-axis and y-axis (DX and DY). After the first resonance frequency there is more variation between the identification results and the FEM model, but the second resonance frequency located at approx. 560 Hz is visible in all of them.

A similar accuracy can be seen on the non-drive-end x-axis and y-axis (NX and NY); however, there is a noticeable offset between the FEM model and the excitation signals. Now, the results are similar and accurate up to the second resonance frequency (560 Hz).

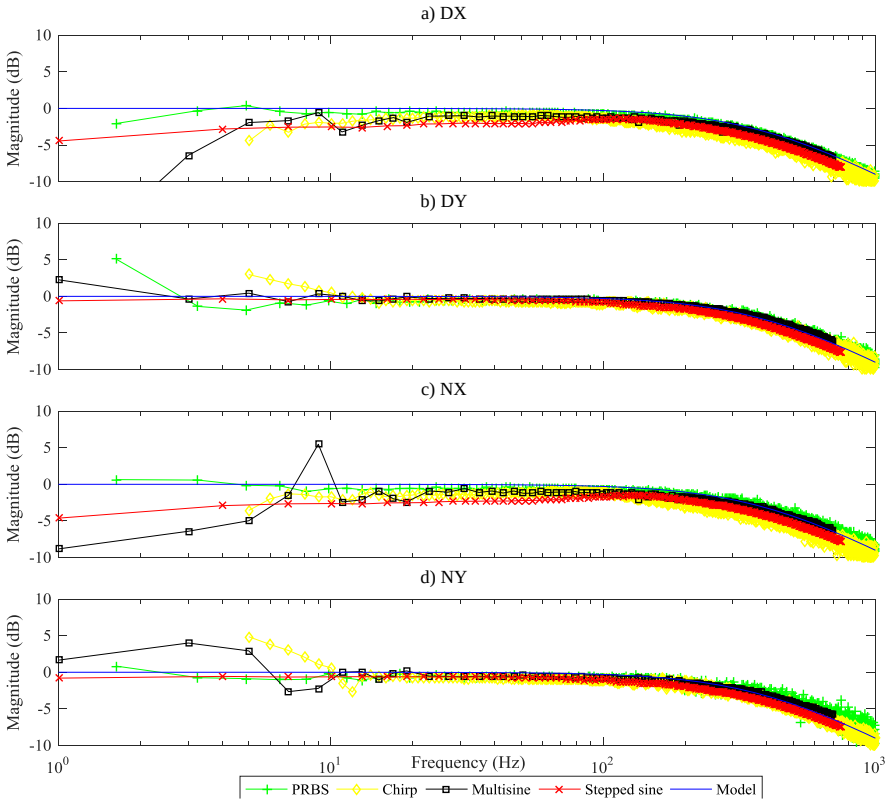

Figure 5.3. Comparison of the inner current control loop transfer functions. DX and DY are the drive-end x-axis and y-axis, respectively. NX and NY are the non-drive-end x-axis and y-axis, respectively. (From **Publication IV**).

The PRBS excitation signal was also used to identify the simulation model of the 10 kW AMB test rig with and without simulated noise. This is shown in Fig. 5.5.

It can be noted that the PRBS excitation signal provides a very good accuracy compared with the FEM model in the simulation with no noise added. When noise is added, the accurate zero detection is impaired. A slightly worse accuracy was found with the experimental results shown in Fig. 5.4.

Finally, the results of the online identification with the sliding DFT are presented for the rotor–bearing system. The same multisine excitation signal is used for these results as previously. However, now only some of the frequencies are tracked with the SDFT {1, 3, 5, 7, 9, 13, 15, 19, 23, 27, 31, 39, 47, 59, 71, 95, 119, 143, 167, 191, 227, 281, 289, 299, 335, 371, 413, 448, 473, 498, 533, 563, 593, 623, 653, 698} Hz in order to see the tracked frequencies more clearly. The window length is selected as $N = 2500$, and the

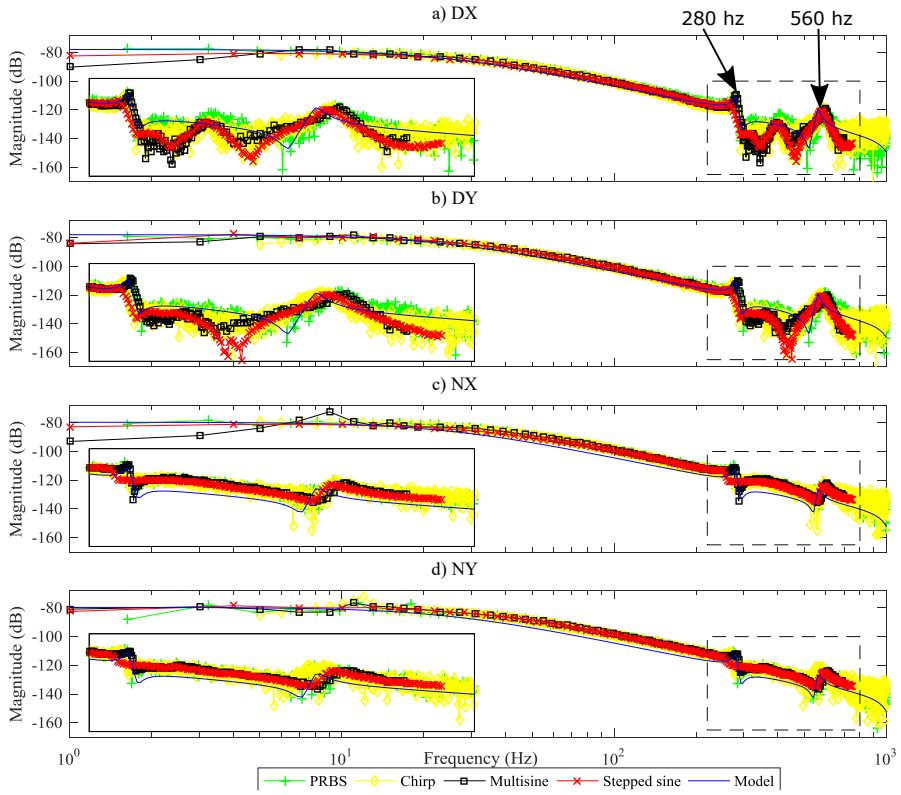

Figure 5.4. Comparison of the open-loop transfer functions of the rotor–bearing system. DX and DY are the drive-end x-axis and y-axis, respectively. NX and NY are the non-drive-end x-axis and y-axis, respectively. (From **Publication IV**).

sampling time T_s as 400 μs. The upper part of Fig. 5.6 shows the SISO-identified frequency response of the SDFT against the direct offline-identified model and the reference rotor–bearing system model. The lower part of Fig. 5.6, again, shows the SISO-identified-frequency response of the SDFT against the indirect offline-identified model and the FEM rotor–bearing system model. The results show that the SDFT is suitable for the online diagnostics purposes.

The online SDFT is also demonstrated with the SIMO identification with the direct offline-identified rotor–bearing system model (Fig. 5.7). A slightly larger deviation can be seen in the SDFT compared with the SISO case. However, the SDFT still captures the system dynamics similarly to the offline direct identification approach, which is based on multisine excitation.

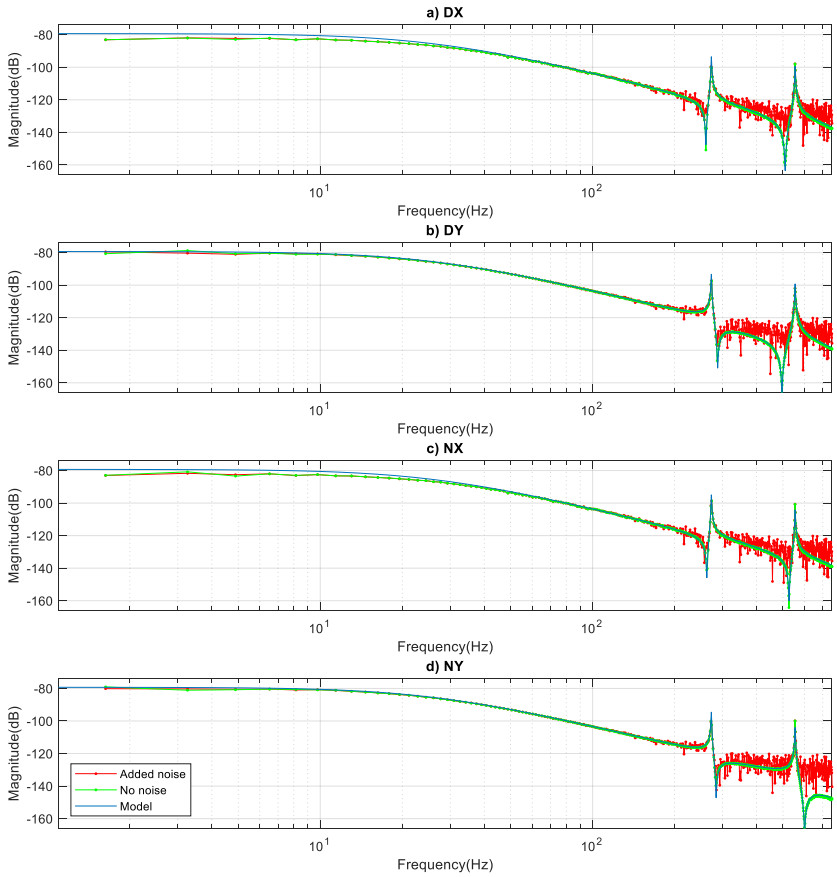

Figure 5.5. Comparison of the open-loop transfer functions of the rotor–bearing system in a simulation with the PRBS excitation signal. DX and DY are the drive-end x-axis and y-axis, respectively. NX and NY are the non-drive-end x-axis and y-axis, respectively.

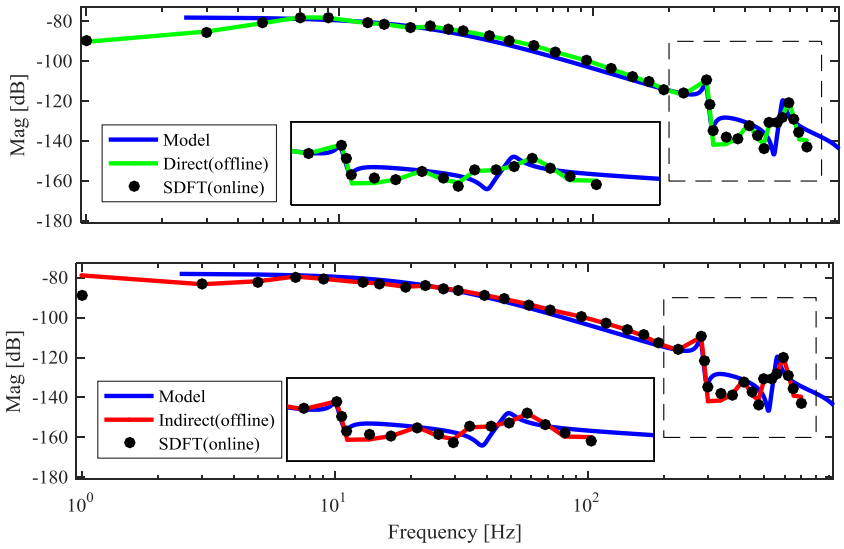

Figure 5.6. Comparison of the online (SDFT) and offline SISO-identified frequency responses of the rotor–bearing system with the reference model. The upper figure shows the direct identification case and the lower figure the indirect one. (From **Publication III**).

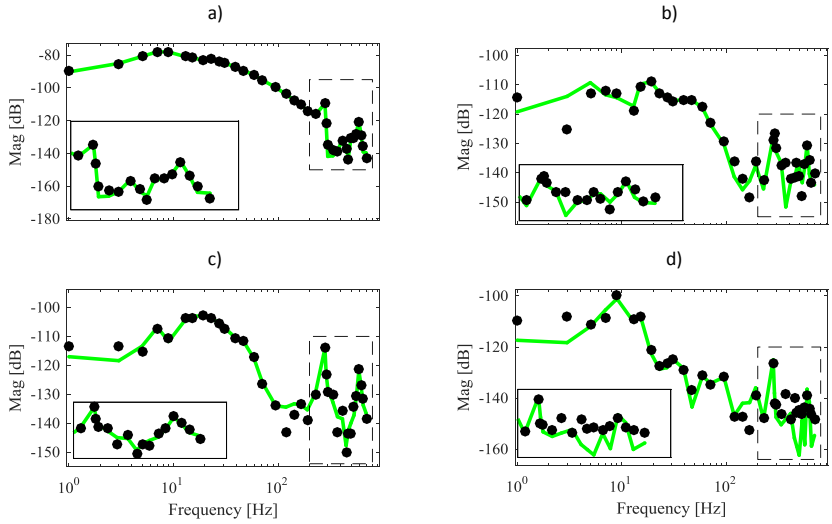

Figure 5.7. Comparison of the online (SDFT) and offline directly identified frequency responses of the rotor–bearing system in the SIMO case. From the drive-end x-axis to the a) drive-end x-axis, b) drive-end y-axis, c) non-drive-end x-axis, and d) non-drive-end y-axis. The green line indicates the offline directly identified model and the dots show the online model. (From **Publication III**).

5.2 10 kW bearingless test rig

The second test rig used in this dissertation is a twin bearingless IPM machine with a 5 kW power per motor unit (total power 10 kW), 30,000 rpm, and an axial AMB. The sampling frequency is $f_s = 20$ kHz. This test rig is discussed in more detail in **Publication VI**. The 10 kW bearingless test rig is shown in Fig. 5.8.

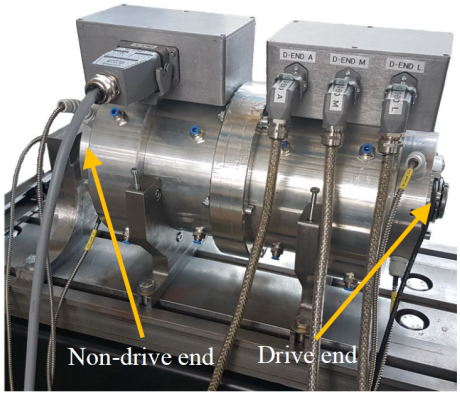

Figure 5.8. 10 kW Bearingless test rig. The axial AMB is in the middle of the machine and the bearingless motors are located on both ends. (From **Publication VI**).

For the bearingless test rig, the rotor–bearing system is identified in the SISO case. An adaptive amplitude stepped sine is used with a frequency range of 1 Hz to 750 Hz with 250 points, resulting in a $f_r = 3.01$ Hz frequency resolution and the maximum amplitude of 0.75 A. This result is shown in Fig. 5.9. It can be noted that the rotor–bearing system can be identified accurately as was the case with the traditional AMB system. The first resonance frequency at 560 Hz is clearly visible. A slight difference can be noticed in the location of the first resonance frequency between the identified model and the rotor model, likely resulting from inaccuracies in the modeling.

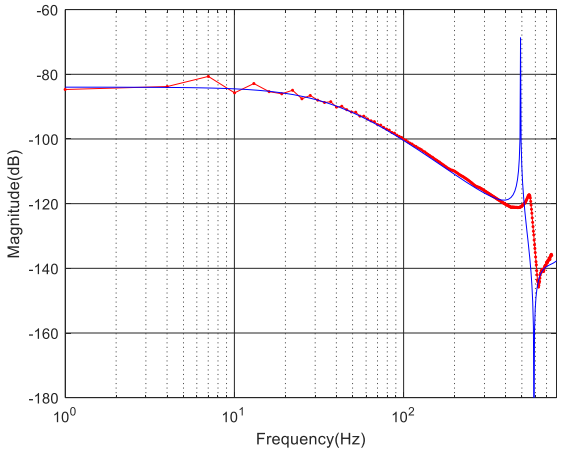

Figure 5.9. Rotor–bearing system identification of the bearingless machine in the SISO case on the drive-end x-axis (DX). The red line indicates the stepped-sine-identified model and the blue one the initial rotor model.

5.3 Hermetic steam turbo generator

The third test rig is a vertically oriented high-speed induction generator with two radial AMBs and one axial AMB. The nominal power of the generator is 1 MW and the speed 12,500 rpm. The sampling frequency is $f_s = 10$ kHz. This test rig is discussed in more detail in **Publication V**. The test rig is shown in Fig. 5.10.

For the hermetic steam turbo generator (HERGE), the rotor–bearing system identification is performed for SISO and MIMO cases with the PRBS excitation signal. The PRBS is constructed such that it is uncorrelated between the inputs (**Publication V**). The PRBS excitation signal has a frequency of $f = 1.67$ kHz with $d = 15$ cells, resulting in a frequency resolution of $f_r = 0.31$ Hz and an amplitude of 0.5 A.

First, the results of the SISO rotor–bearing system identification are presented (Fig. 5.11). The results show that the MIMO PRBS provides adequate correspondence with the model especially on the non-drive-end axes (NX and NY). On the drive-end axes (DX and DY), the accuracy is very good up to the second resonance frequency.

Second, the results of the MIMO rotor–bearing system identification are presented (Fig. 5.12). In the results, the first resonance frequency is visible on all of the FRFs. The cross coupling can also be clearly seen.

Finally, results are provided for the SISO rotor–bearing system identification in the MIMO

Figure 5.10. Hermetic steam turbo generator test rig. (From **Publication V**).

excitation when the rotor is rotating at 90 Hz (Fig. 5.13). It can be seen that the rotor–bearing system identification can also be carried out while the rotor is rotating.

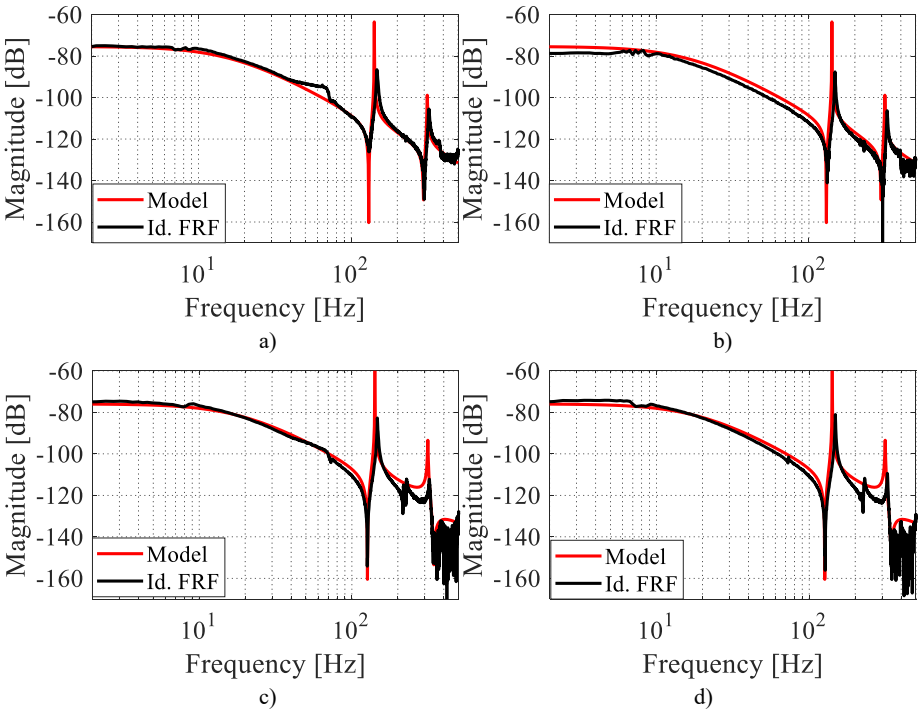

Figure 5.11. Estimated SISO frequency response functions of the rotor–bearing system from the identification tests compared with the initial mathematical model; a) from the non-drive-end x-axis current to the x-axis position NX-NX, b) NY-NY, c) DX-DX, and d) DY-DY. (From **Publication V**).

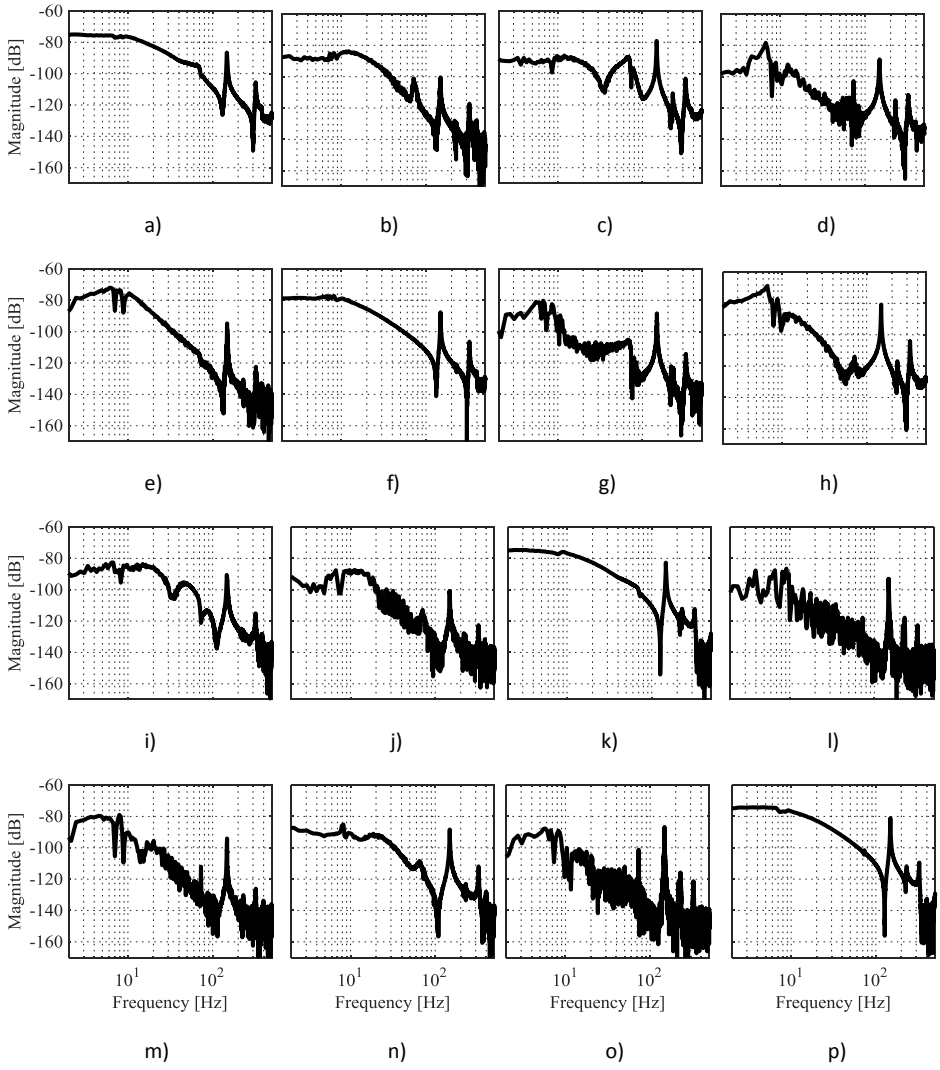

Figure 5.12. Estimated MIMO frequency response functions of the rotor–bearing system from the identification tests; a) NX-NX, b) NX-NY, c) NX-DX, d) NX-DY, e) NY-NX, f) NY-NY, g) NY-DX, h) NY-DY, i) DX-NX, j) DX-NY, k) DX-DX, l) DX-DY, m) DY-NX, n) DY-NY, o) DY-DX, and p) DY-DY. (From **Publication V**).

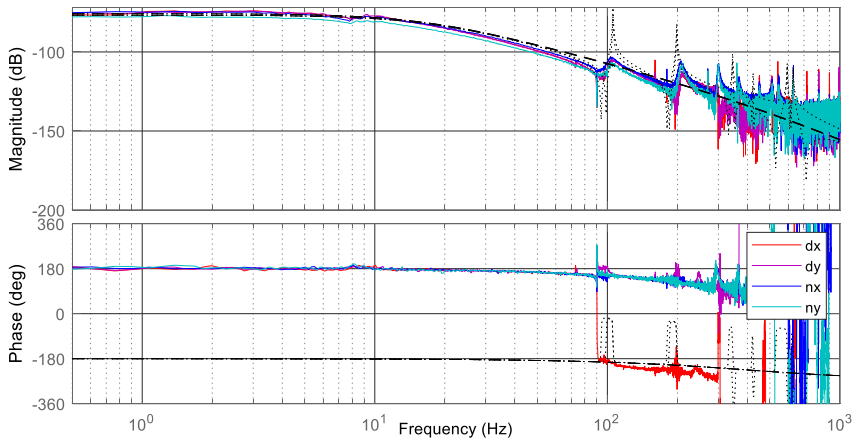

Figure 5.13. Estimated SISO frequency response functions of the rotor–bearing system from the identification tests compared with the initial mathematical model when the rotor is rotating at 90 Hz.

6 Conclusions

In this chapter, the main results of the study are discussed and conclusions are drawn. Suggestions for future work are given.

6.1 Summary

This doctoral dissertation focused on the system identification of magnetically levitated systems. Both offline and online identification methods as well as different excitation signals were considered. First, the theory of the magnetically levitated systems was presented. Then, the rotor modeling was addressed, after which the system identification theory and special cases in the magnetically levitated system identification were discussed. Finally, the results of the system identification were presented for magnetically levitated systems. The estimation errors, uncertainties in measurement signals, and identification results were discussed in brief.

First, simulation and identification results were shown for a 10 kW AMB test rig. It was noted that the PRBS, chirp, multisine, and stepped sine can be used for the offline SISO identification of the inner current loop and the rotor–bearing system. For the rotor–bearing system, identification results where shown with the PRBS also in the simulation case. Then, the online SIMO identification of the rotor–bearing system was presented with the sliding DFT using multisine and comparing the results with the offline identification. It was found that the SDFT provides adequate results compared with the offline identification and the FEM model.

Next, identification results were given for the 10 kW bearingless test rig. It was shown that the stepped sine offline SISO identification of the rotor–bearing system can be used directly also for bearingless machines. This was one of the key scientific contributions of this dissertation and shows that other identification methods can be converted from AMB systems to bearingless machines. The bearingless test rig is also more linear than the AMB test rig because of the linearizing effect of the permanent magnets.

Finally, identification results were shown for the HERGE test rig. First, results with the PRBS for the offline SISO identification of the rotor–bearing system were provided. Then, results were given for the MIMO identification with an uncorrelated PRBS signal. It was found that the MIMO PRBS yields results comparable with the SISO case and that the cross coupling is clearly visible. Finally, results were given for a case where the rotor was rotating at 90 Hz.

The presented identification methods are all suitable for magnetically levitated systems. The SISO and SIMO PRBS identification would be the most suitable method for initial identification, where a high accuracy is not needed; it is also based on easy generation of the PRBS excitation signal. If a higher accuracy is needed, either chirp, multisine, or stepped sine excitation should be used. Stepped sine has the highest accuracy in the SISO

and SIMO identification, but it cannot be used for the MIMO identification, and it is very time consuming. The MIMO identification is the most accurate method, and can be used with the PRBS and multisine excitation signals; however, this requires careful design of the excitation signals for each axis so that they do not correlate with each other. The MIMO multisine excitation would be the choice for the most accurate identification.

For the discussed closed-loop identification approaches (direct, indirect, and joint-input-output), the direct approach is the most suitable one for initial identification, as it does not require knowledge of the controller. For more accurate identification, either an indirect or a joint-input-output approach should be used. The indirect approach is suitable if the controller transfer function is well known and linear. The most accurate method would be the joint-input-output approach. A disadvantage of the join-input-output approach is that knowledge of the reference signal is needed.

6.2 Future Work

Future work could focus on testing of the MIMO identification of bearingless machines. A nonlinear distortion analysis in SISO and MIMO cases could also be performed on both AMBs and bearingless machines. More identification tests could also be carried out when the rotor is rotating. Further topics of study could be identification of a healthy machine vs. a damaged one, or including for instance touching, added delay, motor pull, or rotor reassembly. Further comparisons between simulated and experimental identification tests could also be made. The estimation errors could be analyzed by repeating the same excitation test multiple times and then performing a statistical analysis. This analysis could be applied to monitoring and diagnostics of the system.

References

Allaire, P., et al. (2016). Design of Active Magnetic Radial and Thrust Bearings for High-Speed Turbo Aerator. In: *Proceedings of 15th International Symposium on Magnetic Bearings (ISMB)*, pp. 230–237.

Anderson, B. and Gevers, M. (1979). Identifiability of Closed Loop Systems Using the Joint Input-Output Identification Method. In: *IFAC Proceedings Volumes*, vol. 12, 8, pp. 645 – 652.

Chiba, A. (2005). *Magnetic Bearings and Bearingless Drives*. Amsterdam: Elsevier. ISBN 0-7506-5727-8.

Clark, D.J., Jansen, M.J., and Montague, G.T. (2004). An Overview of Magnetic Bearing Technology for Gas Turbine Engines. *NASA technical memorandum*, pp. 1–7.

Czolczynski, K. (1999). *Rotordynamics of Gas-Lubricated Journal Bearing Systems*. New York: Springer-Verlag New York. ISBN 978-0-387-98677-7.

Eaton, D., Rama, J., and Singhal, S. (2010). Magnetic bearing applications & economics. In: *2010 Record of Conference Papers Industry Applications Society 57th Annual Petroleum and Chemical Industry Conference (PCIC)*, pp. 1–9. ISSN 2161-8127.

Filatov, A., Hawkins, L., and McMullen, P. (2016). Homopolar Permanent-Magnet-Biased Actuators and Their Application in Rotational Active Magnetic Bearing Systems. *Actuators*, 5(4), p. 26.

Gosiewski, Z. and Mystkowski, A. (2008). Robust control of active magnetic suspension: Analytical and experimental results. *Mechanical Systems and Signal Processing*, 22(6), pp. 1297 – 1303. doi:https://doi.org/10.1016/j.ymssp.2007.08.005.

Hynynen, K. and Jastrzebski, R.P. (2009). Optimized excitation signals in AMB rotor system identification. In: *IASTED International Conference on Identification, Control and Applications (ICA)*, pp. 1–6.

Hynynen, K., Jastrzebski, R.P., and Smirnov, A. (2010). Experimental Analysis of Frequency Response Function Estimation Methods for Active Magnetic Bearing Rotor System. In: *Proceedings of 12th International Symposium on Magnetic Bearings (ISMB)*, pp. 40–46.

Hynynen, K. (2011). *Broadband excitation in the system identification of active magnetic bearing rotor systems*. Doctoral dissertation. Lappeenranta University of Technology, Lappeenranta, Finland.

Inman, D.J., et al. (2005). Magnetic Bearings for Non-Destructive Health Monitoring of Rotating Machinery Supported in Conventional Bearings. *Key Engineering Materials*, 293–294, pp. 383–390. doi:10.4028/www.scientific.net/KEM.293-294.383.

ISO 14839-3 (2006). *Mechanical vibration - Vibration of rotating machinery equipped with active magnetic bearings - Part 3: Evaluation of stability margin*. ISO. 14839-3:2006. Geneva, Switzerland: International Organization for Standardization.

Jaatinen, P., et al. (2015). Optimization of the rotor geometry of a high-speed interior permanent magnet bearingless motor with segmented magnets. In: *2015 18th International Conference on Electrical Machines and Systems (ICEMS)*, pp. 962–967.

Jaatinen, P. (2019). *Design and control of a permanent magnet bearingless machine*. Doctoral dissertation. LUT University, Lappeenranta, Finland.

Jacobsen, E. and Lyons, R. (2003). The sliding DFT. *IEEE Signal Processing Magazine*, 20(2), pp. 74–80. ISSN 1053-5888, doi:10.1109/MSP.2003.1184347.

Jastrzebski, R.P. (2007). *Design and implementation of FPGA-based LQ control of active magnetic bearings*. Doctoral dissertation. Lappeenranta University of Technology, Lappeenranta, Finland.

Jastrzebski, R.P., Jaatinen, P., and Pyrhönen, O. (2017a). Modeling and control design simulations of a linear flux-switching permanent-magnet-levitated motor. *Mechanical Engineering Journal*, 4(5), pp. 17–00084–17–00084. doi:10.1299/mej.17-00084.

Jastrzebski, R.P., Jaatinen, P., Pyrhönen, O., and Chiba, A. (2017b). Current injection solutions for active suspension in bearingless motors. In: *2017 19th European Conference on Power Electronics and Applications (EPE'17 ECCE Europe)*, pp. P.1–P.8.

Jastrzebski, R.P., Jaatinen, P., Pyrhönen, O., and Chiba, A. (2018). Design Optimization of Permanent Magnet Bearingless Motor Using Differential Evolution. In: *2018 IEEE Energy Conversion Congress and Exposition (ECCE)*, pp. 2327–2334.

Jastrzebski, R.P., Kurvinen, E., and Pyrhönen, O. (2019). Design, Modelling and Control of MIMO AMB System with 3 Radial Bearing Planes for Megawatt-Range High-Speed Rotor. In: *2019 IEEE International Electric Machines Drives Conference (IEMDC)*, pp. 805–811.

Jastrzebski, R.P., et al. (2015). Design of a bearingless 100 kW electric motor for high-speed applications. In: *2015 18th International Conference on Electrical Machines and Systems (ICEMS)*, pp. 2008–2014.

Jastrzebski, R.P., et al. (2016). Automated Design of AMB Rotor Systems with Standard Drive, Control Software and Hardware Technologies. In: *The 15th International Symposium on Magnetic Bearings*, pp. 78–85.

Jugo, J., Lizarraga, I., and Arredondo, I. (2008). Nonlinear modelling and analysis of active magnetic bearing systems in the harmonic domain: a case study. *IET Control Theory Applications*, 2(1), pp. 61–71. doi:10.1049/iet-cta:20060461.

Katyayn, A. and Agarwal, P.K. (2017). Comparative analysis of conical and conventional active magnetic bearings for complete support of a 5-dof rotor system. In: *2017 International Conference on Advances in Mechanical, Industrial, Automation and Management Systems (AMIAMS)*, pp. 53–58.

Lanzon, A. and Tsiotras, P. (2005). A combined application of $\mathcal{H}_\infty$ loop shaping and μ-synthesis to control high-speed flywheels. *IEEE Trans. Control Syst. Technol.*, 13(5), pp. 766–777. ISSN 1063-6536, doi:10.1109/TCST.2005.847344.

Ljung, L. (1987). *System Identification Theory for the User*. New Jersey: Prentice-Hall, Inc. ISBN 0-13-881640-9.

Lösch, F. (2002). *Identification and automated controller design for active magnetic bearing systems*. Doctoral dissertation. ETH Zürich, Zürich, Switzerland.

Mystkowski, A. and Ambroziak, L. (2010). Investigation of passive magnetic bearing with Halbach-array. *Acta Mechanica et Automatica*, 40(4), pp. 78–82.

Mystkowski, A., Kierdelewicz, A., Kotta, Ü., and Kaparin, V. (2018). Experimental validation of the Newton observer for a nonlinear flux-controlled AMB system operated with zero-bias flux. *International Journal of Control*, 0(0), pp. 1–10. doi: 10.1080/00207179.2018.1552025.

Pintelon, R. and Schoukens, J. (2012). *Design of Excitation Signals*. Wiley-IEEE Press. ISBN 9781118287422, 151-175 p.

Romanenko, A., Smirnov, A., Jastrzebski, R.P., and Pyrhönen, O. (2014). Losses estimation and modelling in active magnetic bearings. In: *2014 16th European Conference on Power Electronics and Applications*, pp. 1–8.

Schweitzer, G. and Maslen, E.H. (2009). *Magnetic Bearings - Theory, Design, and Application to Rotating Machinery*. New York: Springer-Verlag Berlin Heidelberg. ISBN 978-3-642-00496-4.

Severson, E.L. (2018). Bearingless Motor Technology for Industrial and Transportation Applications. In: *2018 IEEE Transportation Electrification Conference and Expo (ITEC)*, pp. 266–273.

Smirnov, A. (2012). *AMB system for high-speed motors using automatic commissioning*. Doctoral dissertation. Lappeenranta University of Technology, Lappeenranta, Finland.

Sokolov, M., Gruber, W., Saarakkala, S., and Hinkkanen, M. (2019). Modeling of a bearingless synchronous reluctance motor with combined windings. In: *Proceedings of the 11th IEEE Energy Conversion Congress and Exposition, ECCE 2019*, pp. 7084–7090.

Timoshenko, S.P. (1921). LXVI. On the correction for shear of the differential equation for transverse vibrations of prismatic bars. *The London, Edinburgh, and Dublin Philosophical Magazine and Journal of Science*, 41(245), pp. 744–746. doi: 10.1080/14786442108636264.

Timoshenko, S.P. (1922). X. On the transverse vibrations of bars of uniform cross-section. *The London, Edinburgh, and Dublin Philosophical Magazine and Journal of Science*, 43(253), pp. 125–131. doi:10.1080/14786442208633855.

Wang, D., Wang, N., Ye, C., and Chen, K. (2017). Research on analytical bearing capacity model of active magnetic bearings based on magnetic saturation. *IET Electric Power Applications*, 11(9), pp. 1548–1557. doi:10.1049/iet-epa.2017.0106.

Webster, J.G. and Eren, H. (2014). *Measurement, Instrumentation, and Sensors Handbook*. CRC Press.

A Appendix

Example MATLAB identification code with PRBS excitation signal.
data_analysis.m

```
load('prbs\Data_11_04_2016_11_48_52.mat')
    f_prbs = data_exc_dx(:,1); %get the frequency vector
    %calculate the FRFs
    dxdx_prbs=prbs_bode_dB(data_exc_dx(:,3),
    data_exc_dx(:,7));
    dxdy_prbs=prbs_bode_dB(data_exc_dx(:,3),
    data_exc_dx(:,8));
    dxnx_prbs=prbs_bode_dB(data_exc_dx(:,3),
    data_exc_dx(:,9));
    dxny_prbs=prbs_bode_dB(data_exc_dx(:,3),
    data_exc_dx(:,10));

    dydx_prbs=prbs_bode_dB(data_exc_dy(:,4),
    data_exc_dy(:,7));
    dydy_prbs=prbs_bode_dB(data_exc_dy(:,4),
    data_exc_dy(:,8));
    dynx_prbs=prbs_bode_dB(data_exc_dy(:,4),
    data_exc_dy(:,9));
    dyny_prbs=prbs_bode_dB(data_exc_dy(:,4),
    data_exc_dy(:,10));

    nxdx_prbs=prbs_bode_dB(data_exc_nx(:,5),
    data_exc_nx(:,7));
    nxdy_prbs=prbs_bode_dB(data_exc_nx(:,5),
    data_exc_nx(:,8));
    nxnx_prbs=prbs_bode_dB(data_exc_nx(:,5),
    data_exc_nx(:,9));
    nxny_prbs=prbs_bode_dB(data_exc_nx(:,5),
    data_exc_nx(:,10));

    nydx_prbs=prbs_bode_dB(data_exc_ny(:,6),
    data_exc_ny(:,7));
    nydy_prbs=prbs_bode_dB(data_exc_ny(:,6),
    data_exc_ny(:,8));
    nynx_prbs=prbs_bode_dB(data_exc_ny(:,6),
    data_exc_ny(:,9));
    nyny_prbs=prbs_bode_dB(data_exc_ny(:,6),
    data_exc_ny(:,10));

    eudx_prbs=db2mag(prbs_bode_dB(data_exc_dx(:,2),
```

```
    data_exc_dx(:,3)));
    eudy_prbs=db2mag(prbs_bode_dB(data_exc_dy(:,2),
    data_exc_dy(:,4)));
    eunx_prbs=db2mag(prbs_bode_dB(data_exc_nx(:,2),
    data_exc_nx(:,5)));
    euny_prbs=db2mag(prbs_bode_dB(data_exc_ny(:,2),
    data_exc_ny(:,6)));
```

prbs_bode_dB.m

```
function [ out_dB, out_phase,h ] = prbs_bode_dB(
    in_seq, out_seq)
    X = fft(in_seq); % input spectrum
    Y = fft(out_seq); % output spectrum
    %4) Power spectrum of the input and cross power
    spectrum between the input and output:
    Rxx = conj(X).*X; % power spectrum of input
    Rxy = conj(X).*Y; % cross power spectrum between
    input and output
    % 5) Divide the cross power spectrum by the
    power spectrum
    Hxy = Rxy./Rxx; % frequency response
    % 6) Computing gain and phase
    out_dB = db(Hxy); % gain in decibels
    p = unwrap(angle(Hxy)); % phase in radians
    (unwrap command is needed to avoid full cycle
    phase jumps)
    %p=angle(Hxy);
    out_phase = p*180/pi; % phase in degrees
    (180 degrees is subtracted for software reasons)
    h=complex(db2mag(out_dB).*cosd(out_phase),
    db2mag(out_dB).*sind(out_phase));
end
```

Publication I

Vuojolainen, J., Jastrzebski, R., and Pyrhönen, O.
Using a pseudorandom binary sequence for rotor-bearing system identification in active magnetic bearing rotor systems

Reprinted with permission from
Proceedings of the 15th International Symposium on Magnetic Bearings (ISMB15), Kitakyushu, Japan
pp. 618–625, 2016

The 15th International Symposium on Magnetic Bearings, August 3-6, 2016, Mojiko Hotel, Kitakyushu, Japan

ISMB15

Using a pseudorandom binary sequence for rotor-bearing system identification in active magnetic bearing rotor systems

Jouni VUOJOLAINEN*, Rafal JASTRZEBSKI* and Olli PYRHÖNEN*

*Dept. of Electrical Engineering, Lappeenranta University of Technology

Skinnarilankatu 34, 53850 Lappeenranta, Finland

E-mail: Jouni.Vuojolainen@lut.fi

Abstract

This paper examines usage of a pseudorandom binary sequence (PRBS) in system identification of the rotor-bearing system in active magnetic bearings (AMBs). In the work, PRBS system identification is compared with adaptive amplitude stepped sine identification. PRBS is a deterministic, periodic signal varying between two levels. A stepped sine wave is a type of sine wave that has all the energy on one frequency only. The paper compares the running time, memory consumption and accuracy of the identification methods studied. A five degree-of-freedom (DOF) AMB testrig is used to test the accuracy of the stepped sine and PRBS system identification approaches. Both methods are implemented in a real-time open automation system. Required running time of the PRBS identification was significantly shorter than that of the stepped sine identification, but more memory was needed for data points. The accuracy of both identification methods was similar at lower frequencies, but at higher frequencies there was greater fluctuation with PRBS identification than when using the stepped sine method. The results show the suitability of using a PRBS in AMB rotor-bearing system identification. The PRBS based approach would be the choice for initial fast identifications of the system, while the stepped sine method would remain as the choice when focusing on identification at specific and higher frequencies.

Keywords: System identification, Frequency response function (FRF), Active magnetic bearing (AMB), Pseudorandom binary sequence (PRBS), Stepped sine

1. Introduction

System identification is the construction of a mathematical model of a dynamical system based on observed and measured data from the system. Input-output data of the system are recorded during specific identification experiments to make the input-output data maximally informative (Ljung, 1987). Different types of identification experiments are used depending on the system to be analyzed. One approach is to use step and impulse signals to obtain identification data from the step and impulse responses of the system. Sine waves can also be used in identification experiments, for example, multisines or stepped sines. A multisine is a sine wave where power is divided into different frequencies, and a stepped sine is a sine wave that has all the power on one frequency only. Random signals such as random Gaussian signals and pseudorandom binary sequence signals have also been used in the identification experiments, for example, by (Shariff, et al., 2013), (Fairweather, et al., 2011). Multi-level pseudorandom signals have been applied for nonlinear system identification, for example, by (Braun, et al., 1999).

For active magnetic bearing (AMB) rotor-bearing system identification, which is the application studied in this work, sine wave based identification experiments have been performed by a number of researchers: stepped sine identification experiments were used by (Gähler, 1998), (Lösch, 2002) and (Vuojolainen, 2015), and multisine identification by (Hynynen, 2011).

This paper applies a pseudorandom binary sequence (PRBS) in system identification of a five degrees-of-freedom (DOF) AMB rotor-bearing system. The suitability of a PRBS approach for AMB rotor-bearing system identification is investigated, and the performance of the PRBS system identification is evaluated and compared with that of an adaptive amplitude stepped sine identification algorithm presented by (Vuojolainen, 2015). Accuracy, memory consumption and

running time are the evaluation criteria used. To the best of the authors' knowledge, no results for the application of PRBS in AMB rotor-bearing system identification and diagnostics have been presented in the literature.

The paper starts by describing the pseudorandom binary sequence and adaptive amplitude stepped sine signal approaches. Experimental results from utilization of the methods in rotor-bearing system identification are then given. The identification results are evaluated and compared with a nominal finite element method (FEM) model of the rotor. In addition, the inner current control loop from the reference control current to the measured control current from the electromagnets is identified. Nonlinearity in the system is investigated with a constant amplitude stepped sine by analyzing the harmonics in the frequency response of the rotor displacement. Finally, conclusions are drawn about the suitability of the PRBS based approach for AMB rotor-bearing system identification.

Nomenclature

A	amplitude
d	order of the PRBS
DX	drive end x-axis
DY	drive end y-axis
f	excitation frequency
f_r	frequency resolution
f_s	sampling frequency
G	transfer function
L	number of data points
N	length of the PRBS
NX	non-drive end x-axis
NY	non-drive end y-axis
U	plant input(reference control current)
V_1	plant output(rotor displacement)
V_2	plant output(measured control current)
Z	axial z-axis

2. Methods

Pseudorandom binary sequence is a type of binary signal which can be used in the system identification. Adaptive amplitude stepped sine is a type of signal where the sine wave amplitude is adjusted to get an acceptable response and is used in the system identification. Nonlinearities in the system can be analyzed with looking at the harmonics present in the frequency response of the rotor displacement.

2.1 Pseudorandom binary sequence

A pseudorandom binary sequence is a periodic, deterministic signal that varies between two levels, typically between amplitudes $+A$ and $-A$. The pseudorandomness of the signal means that although it is deterministic, it seems to behave like a real random sequence and is hard to predict.

Binary signals such as pseudorandom binary sequence have an optimal spectrum for the excitation signal. They are easy to generate, have controllable spectral energy and high spectral energy over a wide band range.

The PRBS is determined by the selected excitation frequency f and the order d. Length N of the PRBS is calculated with:

$$N = 2^d - 1. \tag{1}$$

An example of a third order PRBS signal is shown in Fig. 1a. Figure 1b shows a higher, seventh order PRBS signal. The amplitude of both signals is 1. Using Eq. (1), the length of the third order PRBS signal is 7 and the length of the seventh order PRBS signal is 127. PRBS excitation frequency is 3.33 kHz.

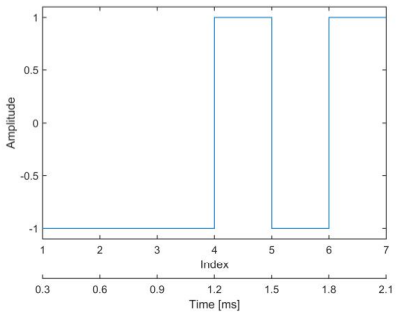

Fig. 1a Example of a third order PRBS.

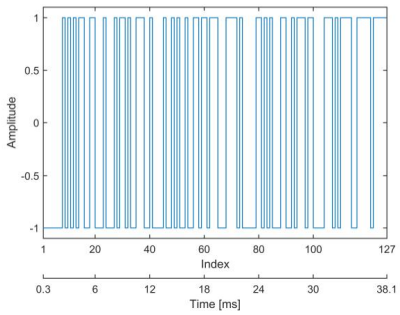

Fig. 1b Example of a seventh order PRBS.

Frequency resolution f_r of the pseudorandom binary sequence is:

$$f_r = \frac{f}{N}, \tag{2}$$

where f is the selected excitation (PRBS generation) frequency and N is the length of the PRBS. The number of data points L needed to save the PRBS identification data is:

$$L = \frac{N f_s}{f}, \tag{3}$$

where f_s is the sampling frequency used, which is 20 kHz in this case. A maximum of one second of the PRBS identification can be saved based on memory consumption considerations. The maximum number of data points in this case is thus 20 000. Now Eq. (3) can be reformulated as the following inequality:

$$\frac{N f_s}{f} \leq 20\,000. \tag{4}$$

Substituting the value of sampling frequency f_s in Eq. (4) yields:

$$\frac{N}{f} \leq 1. \tag{5}$$

Equation (5) shows that the length N of the PRBS and the excitation frequency f have to be chosen based on the maximum number of data points to be saved and the sampling frequency f_s. Multiplying Eq. (5) with excitation frequency f and dividing by the length N gives:

$$1 \leq \frac{f}{N}. \tag{6}$$

From Eq. (2), which defines the frequency resolution f_r of the PRBS signal, and Eq. (6) it can be noted that the frequency resolution of the PRBS is constrained to being equal or greater than one. Equation (2) shows that by decreasing the excitation frequency f and increasing the length N, a higher frequency resolution f_r is achieved. The maximum value of the length N is limited by the maximum number of data points L and the ratio of f/f_s, as seen in Eq. (3). Thus, higher frequency resolution can be achieved by increasing the sampling frequency f_s and the maximum number of data points L and decreasing the excitation frequency f.

PRBS identification was implemented in a real-time open automation system. In this implementation, the order of the PRBS can be chosen from 3 to 13 (where 14 is a limit from Eq. (5)). The amplitude and the number of PRBS measurement periods can be chosen freely. A minimum of two periods of the PRBS signal is used. The first period is a transient period, and data points related to the transient period are discarded because they lead to incorrect results. Data points related to the second period (measurement period) are saved and used for the identification. If two or more measurement periods are used, an average over the measurement periods is calculated and saved. The use of two or more measurement periods enables a better signal-to-noise ratio (SNR) to be achieved and the effect of possible outliers (measurement errors) to be minimized.

An advantage of the PRBS identification is the short runtime required, with ten measurement periods a maximum

of 11 s per axis is needed. A disadvantage is the large amount of memory needed to save the data, which in this case comprise 20 000 data points.

2.2 Adaptive amplitude stepped sine

A stepped sine is a type of sine wave where all the power is on one frequency only. Consequently, the SNR of the stepped sine is very high. In this paper, an adaptive amplitude stepped sine algorithm presented by (Vuojolainen, 2015) is used. Adaptive amplitude means that the sine wave amplitude is adjusted to get an acceptable response. An advantage of the adaptive amplitude stepped sine identification algorithm is that memory is needed only for 250 data points. However, the runtime is long, up to 12 minutes per axis, because every frequency has to be excited separately, and a waiting time is used between frequencies and if the amplitude is adjusted.

2.3 Harmonic analysis of nonlinear systems

Nonlinear systems produce additional harmonics in the frequency response. These harmonics degrade the quality of the measured frequency response functions (FRFs). Quadratic systems generate harmonics that are on the second multiple of the excited frequency. If a system contains harmonics that are on the odd multiple of the excited frequency, these harmonics add to the signal power of the excited frequency and are unwanted (Hynynen, 2011). In the case under study in this work, the rotor-bearing system is quadratic and the odd harmonics are analyzed. Harmonics are analyzed from the spectrum of the rotor displacement for the excited axis. In this study they are analyzed for the drive end *x*-axis (DX) using a constant amplitude stepped sine.

3. Experiments and results of the system identification

A five degree-of-freedom AMB testrig was used to test the PRBS and adaptive amplitude stepped sine system identification approaches. The testrig consists of two radial and one axial active magnetic bearing. For the PRBS identification, the excitation frequency was 3.33 kHz, the order was 11, the frequency resolution was 1.63 Hz, the amplitude was 2.5 A, and ten measurement periods were used. For the adaptive amplitude stepped sine identification, the frequency range was from 1 Hz to 750 Hz, the frequency resolution was 3.01 Hz, and the maximum sine wave amplitude was 2.5 A. A simple FRF, an empirical transfer function, was used to form the experimental transfer functions based on the identifications.

In the harmonic analysis of the rotor-bearing system, two different frequency bands were used, both of which used a sine wave amplitude of 2.5 A and step size of 4 Hz. The first frequency band was from 2 Hz to 146 Hz and the second frequency band was from 150 Hz to 302 Hz.

3.1 Rotor-bearing system identification

For the rotor-bearing system identification, excitation was applied at the reference control current. The plant input U and output V_1 were measured for the corresponding axis to form the open loop plant transfer function from the reference control current to the rotor displacement. The open loop plant transfer function G is written as:

$$G = \frac{V_1}{U}. \tag{7}$$

After forming the open loop plant transfer functions for the PRBS and adaptive amplitude stepped sine system identification, respectively, the transfer functions and the FEM-model rotor transfer function were compared. The comparison is shown in Fig. 2.

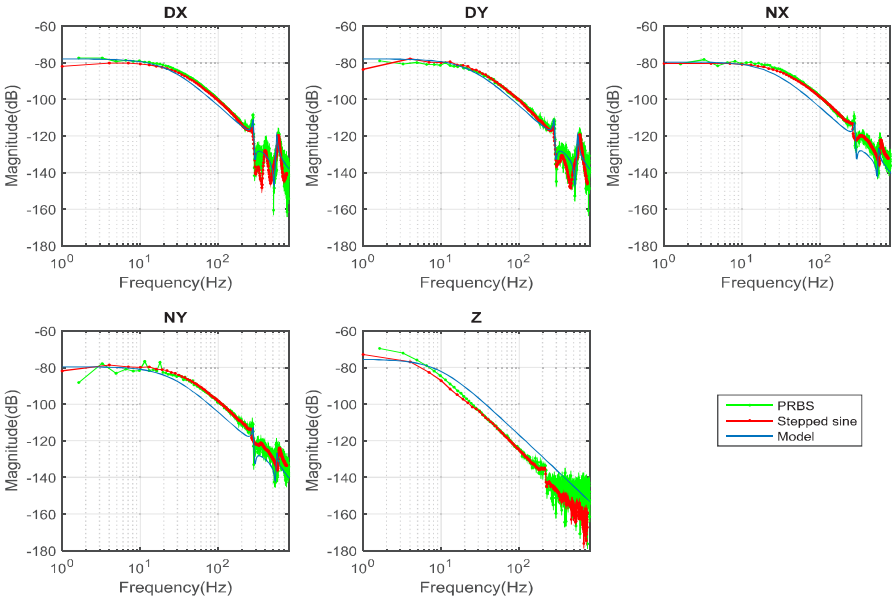

Fig. 2 Comparison of the open loop plant transfer functions, from the reference control current U to the rotor displacement V_1 for the corresponding axis. D is the drive end, N is the non-drive end and Z is the axial direction.

From Fig. 2, it can be seen that when compared to the FEM-model of the rotor, both the adaptive amplitude stepped sine and PRBS identification yield similar accuracy. The stepped sine identification has less fluctuation than the PRBS identification, particularly in the frequency range after the first resonance/anti-resonance frequency pair located at around 280 Hz and 290 Hz on the radial axes. On the Z-axis PRBS identification starts to have more fluctuation at around 220 Hz. PRBS identification on the other hand matches the model more accurately on the first resonance/anti-resonance frequency pair on the radial axes. PRBS has higher resolution 1.63 Hz compared to the stepped sine with 3.01 Hz resolution.

3.2 Inner current control loop identification

For the inner current control loop identification, excitation was applied at the reference control current. The plant input U and output V_2 were measured for the corresponding axis to form the transfer function from the reference control current to the measured control current. Transfer function G from the reference control current to the measured control current is written as:

$$G = \frac{V_2}{U}. \tag{8}$$

Comparison between the stepped sine and the PRBS identification of the inner current control loop is shown in Fig. 3.

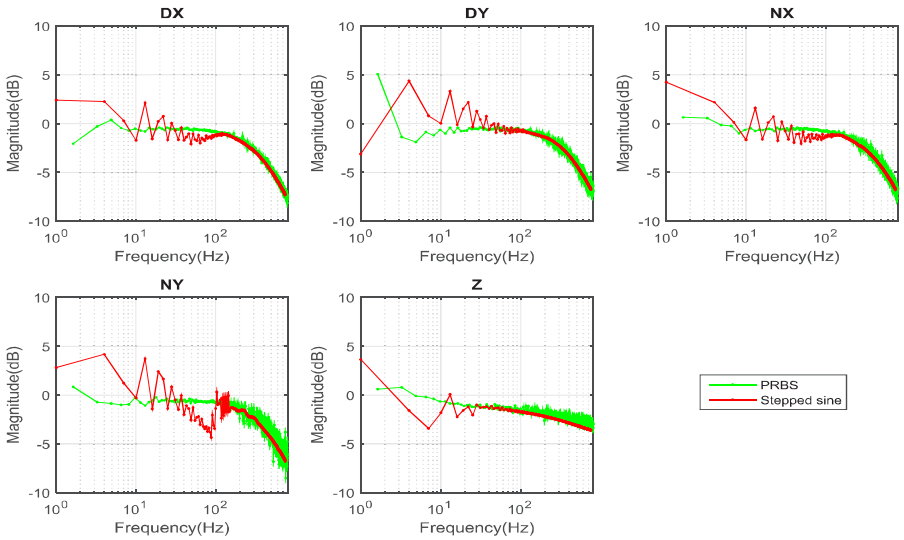

Fig. 3 Comparison of the inner current control loop transfer functions, from the reference control current U to the measured control current V_2 for the corresponding axis. D is the drive end, N is the non-drive end and Z is the axial direction.

From Fig. 3, it can be noted that in the frequency range below 100 Hz on the radial axes, the PRBS identification has less fluctuation between the identified points. On the Z-axis, PRBS identification has less fluctuation up to 30 Hz. On the radial axes, inner current control loop identification results start to converge at around 100 Hz, except on the NY-axis where convergence begins at around 150 Hz. On the Z-axis convergence occurs at around 30 Hz. After the convergence point, fluctuation in the PRBS identification starts to increase on all axes.

3.3 Harmonic analysis of the rotor-bearing system

In the harmonic analysis of the rotor-bearing system, excitation was applied at the reference control current on the DX-axis and the spectrum of the output V_1 (rotor displacement) was measured. Figure 4 shows the harmonic analysis of the frequency band from 2 Hz to 146 Hz in 4 Hz steps. Figure 5 shows the harmonic analysis of the frequency band from 150 Hz to 302 Hz in 4 Hz steps.

From Fig. 4, it can be seen that there are harmonics in the rotor-bearing system. A second harmonic, implying a quadratic system, is visible. A third harmonic, which is unwanted, is clearly visible. Other harmonics such as the fourth, sixth and unwanted fifth harmonic can be noted, especially at lower frequencies.

In Fig. 5, the second harmonic is clearly visible. The unwanted third harmonic is also visible but has less amplitude than in the harmonic analysis presented in Fig. 4. A fourth harmonic can also be seen. Other harmonics are not visible.

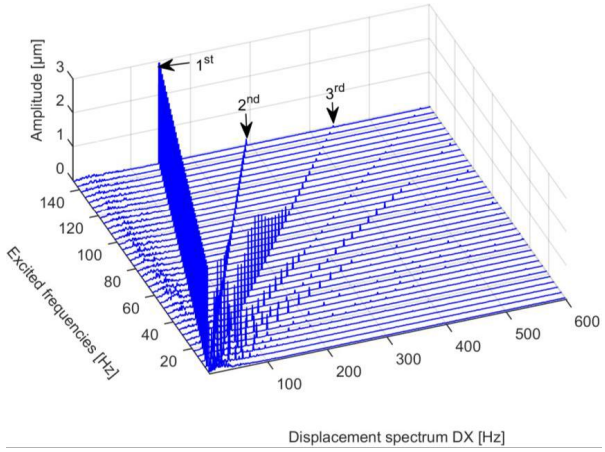

Fig. 4 Harmonic analysis of the rotor-bearing system on the drive end *x*-axis (DX). Frequencies from 2 Hz to 146 Hz in 4 Hz steps were excited. The second and third harmonics show clearly.

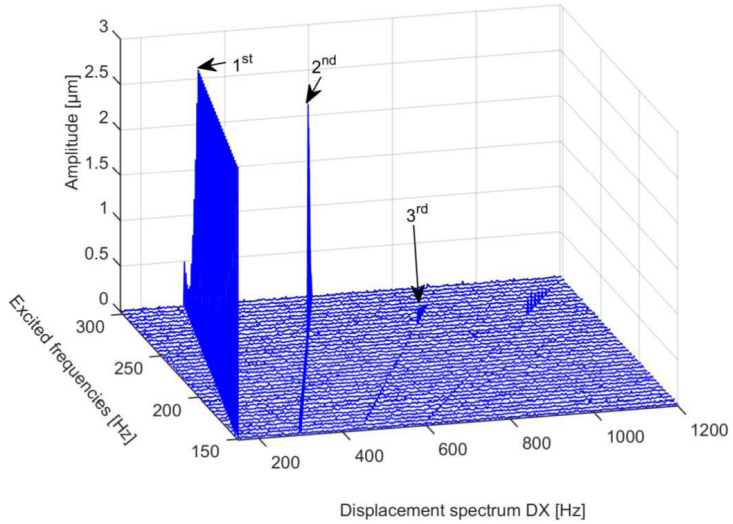

Fig. 5 Harmonic analysis of the rotor-bearing system on the drive end *x*-axis (DX). Frequencies from 150 Hz to 302 Hz in 4 Hz steps were excited. The second harmonic is clearly seen and a small third harmonic is present.

4. Discussion

Stepped sine and multisine identification experiments have typically been used in AMB rotor-bearing system identification. The results in this paper show the suitability of using a PRBS based approach in AMB rotor-bearing system identification. Comparison between the PRBS system identification and the adaptive amplitude stepped sine system identification showed that the required runtime of the stepped sine system identification is longer than that of the PRBS system identification. However, less memory is needed. The accuracy of the stepped sine system identification of the rotor-bearing system was greater at higher frequencies and the approach also produced more accurate results for inner

current control loop system identification at higher frequencies. The PRBS system identification had better accuracy for inner current control loop system identification at lower frequencies. Both identification methods had similar accuracy for rotor-bearing system identification at lower frequencies, but the PRBS system identification matched better the first resonance/anti-resonance frequency pair on the radial axes.

The harmonic analysis demonstrated that the second harmonic is clearly visible, indicating that the rotor-bearing system is quadratic. An unwanted third harmonic is also visible, especially at lower frequencies in the frequency band from 2 Hz to 146 Hz.

5. Conclusion

Use of a PRBS based approach was found to be feasible for AMB rotor-bearing system identification. The required running time is shorter than with stepped sine identification, but more memory is needed to store data points. The accuracy of both identification methods was similar for rotor-bearing system identification at lower frequencies. For inner current control loop identification, PRBS identification was more accurate at lower frequencies. Stepped sine identification was more accurate for rotor-bearing system identification at higher frequencies and gave better results for inner current control loop identification.

PRBS would be the first choice for fast and safe identification and diagnostics of the system. Other identification methods such as the stepped sine approach used in this work and multisine approaches could then be used to obtain a more accurate correspondence between the experimentally identified model and the FEM-model of the rotor, especially at higher frequencies.

Future work could include the testing of multi-level PRBS identification in rotor-bearing system identification. Additionally, the effect of adapting the amplitude of the PRBS signal based on noise and the maximum response of previous experiments could be investigated.

Acknowledgment

The work has been supported by Academy of Finland, decisions No. 270012 and No. 273489.

References

Braun, M. W., Riviera, D. E., Stenman, A., Foslien, W. and Hrenya, C., Multi-level pseudo-random signal design and 'model-on-demand' estimation applied to nonlinear identification of a RTP wafer reactor, Proceedings of the American Control Conference, Vol.3 (1999), pp.1573-1577.

Gähler, C., Rotor dynamic testing and control with active magnetic bearings (1998), Doctoral Thesis, ETH Zürich, Switzerland.

Fairweather, A. J., Foster, M. P. and Stone, D. A., Battery parameter identification with pseudo random binary sequence excitation (PRBS), Journal of Power Sources, Vol.196, Issue 22 (2011), pp.9398-9406.

Hynynen, K., Broadband excitation in the system identification of active magnetic bearing rotor systems (2011), Doctoral Thesis, Lappeenranta University of Technology, Finland.

Ljung, L., System Identification: Theory for the User (1987), Prentice-Hall, Inc.

Lösch, F., Identification and automatic controller design for active magnetic bearing systems (2002), Doctoral Thesis, ETH Zürich, Switzerland.

Shariff, H. M., Fazalul Rahiman, M. H. and Tajjudin, M., Nonlinear system identification: comparison between PRBS and random gaussian perturbation on steam distillation pilot plant, Proceedings of the IEEE 3rd International Conference on System Engineering and Technology (ICSET) (2013), pp.269-274.

Vuojolainen, J., Active magnetic bearing system identification methods and rotor model updating (2015), Master's Thesis, Lappeenranta University of Technology, Finland.

Publication II

Jastrzebski, R., Vuojolainen, J., Jaatinen, P., Sillanpää, T., and Pyrhönen, O.
Commissioning of Modular 10kW Magnetically Levitated Test Rig

Reprinted with permission from
Proceedings of the 19th International Conference on Electrical Machines and Systems (ICEMS), Chiba, Japan
pp. 1–6, 2016

Publication III

Vuojolainen, J., Nevaranta, N., Jastrzebski, R., and Pyrhönen, O.
Online identification of AMB rotor system dynamics using sliding DFT

Reprinted with permission from
Proceedings of the IEEE 11th International Symposium on Diagnostics for Electrical Machines, Power Electronics and Drives (SDEMPED), Tinos, Greece
pp. 267–273, 2017

Online Identification of AMB Rotor system dynamics using Sliding DFT

Jouni Vuojolainen, Niko Nevaranta, Rafal P. Jastrzebski, and Olli Pyrhönen
Dept. of electrical engineering
Lappeenranta University of Technology (LUT)
Lappeenranta, Finland
Jouni.Vuojolainen@lut.fi

***Abstract*— This paper presents an online nonparametric frequency response estimation approach for the identification of rotor dynamics of a high-speed machine supported by an active magnetic bearing (AMB) system. The closed-loop identification estimation approaches (direct and indirect) are based on a sliding discrete Fourier transform (SDFT) method that is applied in conjunction with a known multisine excitation signal design. The feasibility of the proposed identification approach is verified with experimental results on an AMB system. According to the results, the SDFT-based identification approach is applicable to online identification of rotor system dynamics in a computationally efficient manner.**

Keywords*— Active magnetic bearing (AMB) system, monitoring, online identification, sliding discrete Fourier transform (SDFT)

I. INTRODUCTION

OVER the recent years, different active magnetic bearing (AMB) rotor systems have become essential in demanding industry applications such as high-speed levitated blowers, pumps, generators, centrifugal compressors, and gas-turbine engines, to name but a few. This trend follows the increasing advantages in high-speed technology along with improvements in the calculation capacity of modern power electronics devices. In order to obtain fast and precise AMB systems, a successful design relies on a wide range of factors: complex control electronics, accurate plant modeling, modal analysis of rotor dynamics, and challenging control system design based on system identification.

Particularly, in the case of AMB systems it is of great importance to have adequate analytical models for control design in order to achieve a robust high-performance control system. Consequently, over the years, a great deal of effort has been made to develop system identification-based commissioning tools for AMB systems [1]. So far, the off-line identification of AMB systems has been performed to obtain parameter estimates, that is, physical values for controller design purposes. Even though most of the modeling and analysis is typically carried out in the frequency domain, time domain parameter estimation is also important particularly from the viewpoint of controller design.

Several off-line closed-loop identification methods can be found in the literature, and an extensive overview of identification and modeling approaches for AMB systems has been provided in [2]. In [3], a neural network auto-regressive model with an exogenous inputs (NNARX) structure has been proposed to identify the dynamics of an AMB system. Another approach has been introduced in [4], where a genetic-algorithm-based weighted least squares (GA-WLS) approach is introduced for robust control design based on the basis of the identified models so that the performance is optimized in terms of H_∞. Subspace-method-based identification has also been applied for example in [5], where a predictor-based subspace identification (PBSID) algorithm is presented and used for robust control design. In [6], least-squares-based parametric identification for an SISO AMB system is presented using a weighting function to reduce the effect of high frequencies on the model fitting. In [7], parametric MIMO multivariable identification for AMB systems is presented; it is capable of estimating both rigid body and flexible modes robustly, while other methods reported in the literature are claimed to be incapable of this. Furthermore, in [8], closed-loop identification of an AMB rotor system has been studied by applying a joint input and output approach to obtain an MIMO model.

Despite the extensive development of system identification methods for commissioning purposes, there are only a few studies available on the issues related to the real-time identification of AMB systems. In [9] and [10], diagnostics of an AMB system has been performed by taking a signal-based approach combined with a fuzzy logic system for fault classification. A least-mean-squares algorithm has been proposed in [11] for online identification of the current and position stiffness of an AMB system. Another real-time identification approach has been reported in [12], where a model-free imbalance compensation method is proposed based on online identification of the Fourier coefficient of the rotor imbalance disturbance. The extended Kalman filter (EKF) is a

The authors would like to thank Academy of Finland, grant No. 304071 and No. 304784 for its financial support.

978-1-5090-0409-6/17/$31.00 ©2017 IEEE

popular online identification tool for nonlinear systems, and it has been studied in [13] and [14] in the case of AMB systems.

This paper addresses issues in the monitoring and diagnostic options of an AMB system in the frequency domain. Motivated by the features of the sliding discrete Fourier transform (SDFT) in [15], the objective of this paper is to study nonparametric model estimation of an AMB system in real time. The SDFT is applied to nonparametric identification at a selected set of frequencies in conjunction with a multisine excitation signal input design. Moreover, the SDFT is applied for direct and indirect closed-loop identification purposes.

The paper is organized as follows: Section II describes the problem statement by introducing the frequency response identification of rotor dynamics supported by an active magnetic bearing (AMB) system. In addition, application of the SDFT to closed-loop identification is discussed. After that, in Section III, the proposed approach is verified by experimental tests and analyzed. Section IV concludes the paper.

II. PROBLEM STATEMENT

Owing to stability, performance, or safety constraints, identification of industrial systems must often be performed in a closed loop. An AMB system is a typical example of a closed-loop identification case, where identification must be carried out in closed-loop conditions because of the unstable open-loop system dynamics. A general principle of the closed-loop identification experiment for the AMB system dynamics is illustrated in Fig. 1, where the excitation signal is superposed to the current references of the radial bearing control. Naturally, depending on the AMB system configuration, the controller topology for the axial (z-direction) and radial (*x*- and *y*-direction) positions differs from Fig. 1, and thus, it has to be designed case specifically, but the fundamental control objective in the identification experiment is basically the same: to obtain frequency response functions that describe the dynamics of the MIMO system, that is, the drive end (the load side dynamics) and non-drive end dynamics, and the coupling between them.

In this paper, online identification of the AMB system dynamics is considered by applying a frequency domain nonparametric estimation approach at the frequencies where the excitation is provided. Online monitoring of these frequencies is carried out by applying a DFT algorithm that provides benefits in terms of computational efficiency and real-time performance. Thus, the well-known real-time DFT algorithm, sliding discrete fourier transform (SDFT), is considered in this paper for the online identification purposes. With the SDFT changes in the frequency response of the system dynamics due to e.g. unbalance, crack in the rotor, aging and thermal expansion can be monitored. However, it is pointed out that the main contribution of this paper is on introducing a real-time identification approach that can be considered for diagnostics purposes in AMB systems. Hence, the diagnostics options of actual failures is not discussed in this paper.

A. Frequency domain identification

Frequency domain identification approaches are well-established and of great importance for AMB commissioning purposes. The most straightforward nonparametric identification approach of the frequency response function of an SISO system is an empirical transfer function estimate (ETFE) defined by

$$\hat{G}_0(\mathrm{j}\omega_k) = \frac{Y(\omega_k)}{U(\omega_k)}, \tag{1}$$

where $Y(\omega_k)$ and $U(\omega_k)$ represent the DFT of the input $u(n)$ and output $y(n)$ signals. The DFT of a signal $x(n)$ over one period N of samples can be expressed in the form

$$X_k(n) = \sum_{l=0}^{N-1} x(n) e^{-\mathrm{j}k(2\pi/N)l}. \tag{2}$$

The ETFE (1) can be extended to MIMO systems, leading to an empirical frequency response matrix (ETRM) estimate [8]

$$\hat{\mathbf{G}}_0(\mathrm{j}\omega_k) = \mathbf{Y}(\omega_k)\mathbf{U}^{-1}(\omega_k), \tag{3}$$

with the input $\mathbf{U}(\omega_k)$ and output $\mathbf{Y}(\omega_k)$ matrices that contain the DFTs of all input and output signals. It is pointed out that in this paper, the identification problem is treated as a single input multiple output (SIMO) so that the excitation signal is superposed to the drive end *x*-axis controller. In the case of the AMB system under study, the outputs of the SIMO system are the drive end *x*-axis position, the drive end y-axis position, the non-drive end *x*-axis position, and the non-drive end *y*-axis position constituting a 1x4 SIMO system. The focus of this paper is on SISO identification, that is, identification of the drive end dynamics, and thus, SIMO system identification is only considered for demonstration purposes.

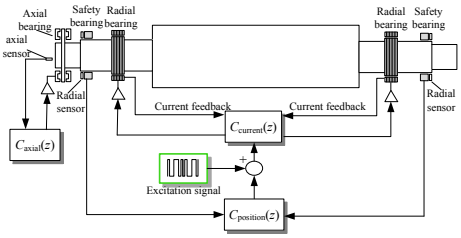

Fig. 1. General principle of a closed-loop identification experiment for an AMB system.

B. *Sliding discrete fourier transform*

The frequency spectrum of a discrete-time signal can be determined by a discrete Fourier transform, which, in practice, requires that all the measurement samples over a full measurement window are summed and multiplied by an exponential function. The SDFT algorithm is feasible for computationally efficient real-time spectral analysis by the sliding window that works on a sample-by-sample basis. At a specific time instant n, the kth-order harmonic can be calculated within a period of N samples as

$$X_k(n) = \sum_{l=0}^{N-1} x(n-(N-1)+l)e^{-\mathrm{j}k(2\pi/N)l} . \quad (4)$$

From (4), the basic form of the SDFT can be derived [16], leading to the following expression

$$X_k(n) = (X_k(n-1) + x(n) - x(n-N))e^{\mathrm{j}k(2\pi/N)} \quad (5)$$

This form describes the main principle of the SDFT, where the computational efficiency is based on the moving window, which can be applied to calculate a new DFT bin from the previous DFT result.

The implementation and principle of the SDFT are illustrated in Fig. 2. The SDFT algorithm is based on the fact that at each time instant n only the newest measurement sample is added to the sum, and at the same time, the oldest measurement sample is removed from the window as depicted in Fig. 2 a). The main idea behind the SDFT is to obtain moving window-type processing for real-time spectral analysis, that is, the signals used in the identification are tracked as illustrated in Fig. 2 b) on a sample-by-sample basis.

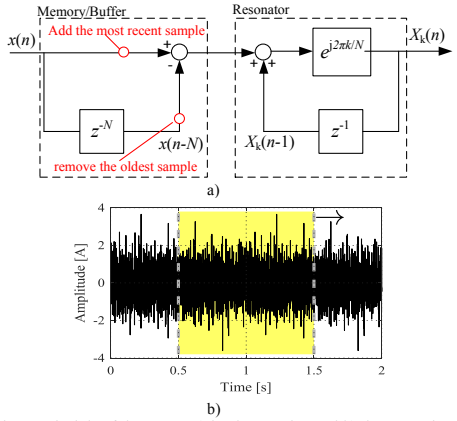

Fig. 2. Principle of the SDFT: a) implementation and b) demonstration of the SDFT window (yellow region) plotted over two periods of the multisine excitation signal in the time domain.

C. *Closed-loop identification*

In this paper, the SDFT is applied to direct and indirect closed-loop identification of the AMB system dynamics. In the direct identification approach, the influence of the feedback controller is omitted, and the approach is applied directly to the measured input $u(k)$ and output $y(k)$ signals. Correspondingly, the main idea behind the indirect identification relies on the fact that the open-loop model $G_0(\mathrm{j}\omega)$ is solved from the identified closed-loop transfer function $G_{\mathrm{cl}}(\mathrm{j}\omega)$ between the measured output $y(k)$ and the excitation signal $w(k)$ as follows

$$\hat{G}_0(\mathrm{j}\omega_k) = \frac{\hat{G}_{\mathrm{cl}}(\mathrm{j}\omega_k)}{1-\hat{G}_{\mathrm{cl}}(\mathrm{j}\omega_k)C(\mathrm{j}\omega_k)} \quad (6)$$

by exploiting the knowledge of the controller $C(\mathrm{j}\omega)$. It is pointed out that, to the authors' knowledge, the indirect closed-loop approach has not been widely applied to AMB system identification thus far [17]. In this paper, a model-based linear quadratic Gaussian multi-input multi-output controller with known parameters is considered during the identification experiment. Therefore, the open-loop model can be solved indirectly. The controller weighting matrices have been optimized using loop shaping and evolutionary principles, which have been reported, for example in [18],[19] and [20]. In general, the initial synthesis is performed using the assumed plant model. The identified model can be employed in the refined controller synthesized with the aforementioned genetic tuning.

III. EXPERIMENTAL RESULTS

An AMB test rig is used to validate the offline direct and indirect closed-loop identification and the proposed online SDFT identification approaches. The test rig is discussed in detail in [21] and shown in Fig. 3. A multisine signal with a frequency range of 1–700 Hz with four separate bands having different frequency resolutions and amplitudes is considered as an excitation signal. The first band has a frequency range of {1, 19} with 2 Hz resolution and amplitude of 10 mA, the second band {23, 199} with 4 Hz resolution and amplitude of 50 mA, the third band {203, 399} with 2 Hz resolution and

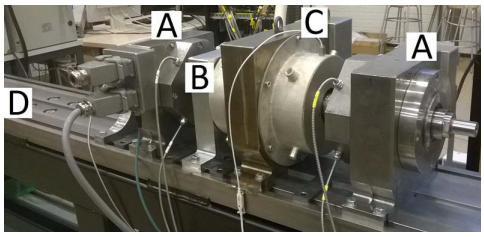

Fig. 3. Experimental test rig a) radial bearing modules, b) axial bearing modules, c) induction motor, and d) test bench. Description of control electronics can be found in detail in [19].

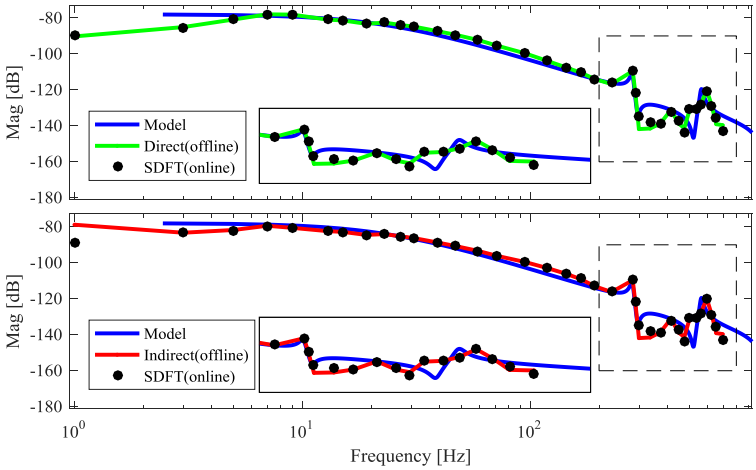

Fig. 4 Comparison of the online (SDFT) and off-line SISO identified frequency responses with the reference model. The upper figure shows the direct identification case and the lower figure the indirect one.

amplitude of 80 mA, and the fourth band {403, 698} with 5 Hz resolution and 120 mA amplitude.

For illustrative purposes only, some of the excited frequencies are tracked with the SDFT. The following frequencies are considered: {1, 3, 5, 7, 9, 13, 15, 19, 23, 27, 31, 39, 47, 59, 71, 95, 119, 143, 167, 191, 227, 281, 289, 299, 335, 371, 413, 448, 473, 498, 533, 563, 593, 623, 653, 698} Hz. Naturally, the selected set of frequencies determines the parametrization of the SDFT algorithm, that is, the required resonators and the window length N as shown in [15]. In this paper, the window length is selected as N = 2500 and the sampling time T_s as 400 µs.

First, the proposed identification approach is studied by identifying the nonparametric SISO model of the drive end x-axis dynamics. In the upper part of Fig. 4, the directly online-identified SISO frequency response is compared with the offline post-processed one and shown with the reference model. The reference model in Fig. 4 refers to a mathematical model obtained from a FEM-based rotor dynamic analysis. It is pointed out that, the flexible modes of the FEM-model has been updated based on system identification experiments with a pseudo random binary signal (PRBS) [22] and using a method presented in [23]. It is also emphasized that this model is for illustrative purposes only in order to show that the identified system dynamics with the proposed method are close to the assumed ones, e.g. the modeled resonance frequencies. Hence, the results of the proposed online identification approach (dots) are compared, and thus, validated against the offline identified ones (solid lines) in Fig. 4.

Moreover, the zoom in Fig. 4 is taken from the frequency region around the flexible modes to verify the effectiveness of the SDFT for frequency response estimation. Based on the results, the estimated frequency responses in Fig. 4 are quite similar with only minor differences, and thus, it is evident that the SDFT provides reasonable estimates of the rotor dynamics over the excited frequency band at the selected set of frequencies. Thus, it is clear that the SDFT is feasible for online system diagnostics purposes. To further validate these observations, in the lower part of Fig. 4, the drive end x-axis system dynamics are also identified indirectly with the SDFT by applying (6) and comparing this result with the off-line post-processed frequency response. Again, the online and off-line result agree remarkably well, although some minor differences in the amplitude response can be detected in the frequency region around the flexible modes and in the DC region. By comparing the direct and indirect identification approaches in Fig. 4, the results are similar but the indirect identification method has a slightly better correspondence with the model in the DC region and up to the 40 Hz frequency, as expected.

To further demonstrate the SDFT algorithm performance, the SIMO system dynamics of the AMB system is directly and indirectly identified based on (3). In Fig. 5, the direct online frequency response of the SIMO AMB system identification is shown and compared with the offline post-processed one and in Fig. 6 with the indirect one, respectively. The zoom is taken from the frequency region that constitutes the dominant flexible system dynamics. Evidently, the SIMO system identification results in Figs. 5 and 6 show a slightly higher deviation when comparing the results with the SISO case. This result is expected because of the fundamental difference between the off-line and online identification approaches. Moreover, it is pointed out that the excitation signal has been

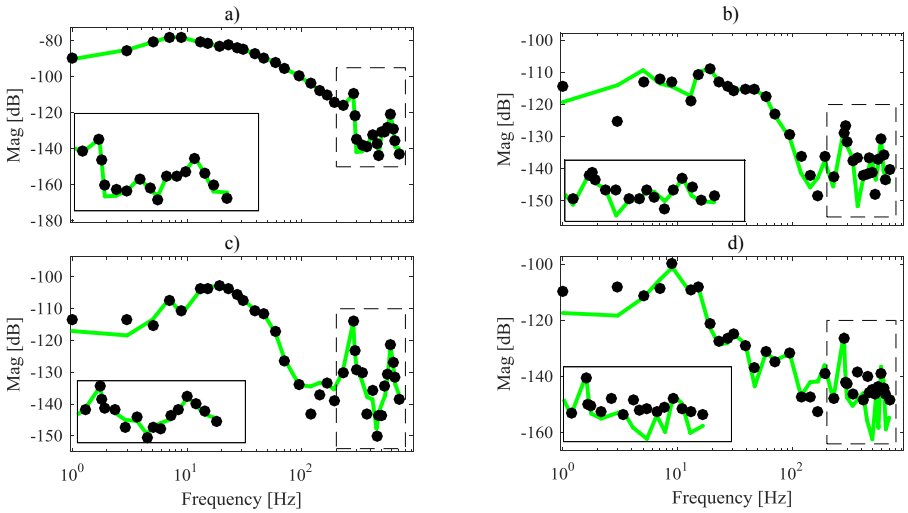

Fig. 5 Comparison of the online (SDFT) and off-line directly identified frequency responses in the SIMO case. From the drive end *x*-axis to the a) drive end *x*-axis, b) drive end *y*-axis, c) non-drive end *x*-axis, and d) non-drive end *y*-axis. The green line indicates the off-line directly identified model and the dots show the online model.

superposed to the drive end *x*-axis current control in order to obtain a representative nonparametric model of its dynamics. For this reason, it is obvious that the coupled system dynamics cannot be identified accurately from this experiment only. Nevertheless, based on the results, it is clear that the SDFT tracks the selected frequencies remarkably well and captures

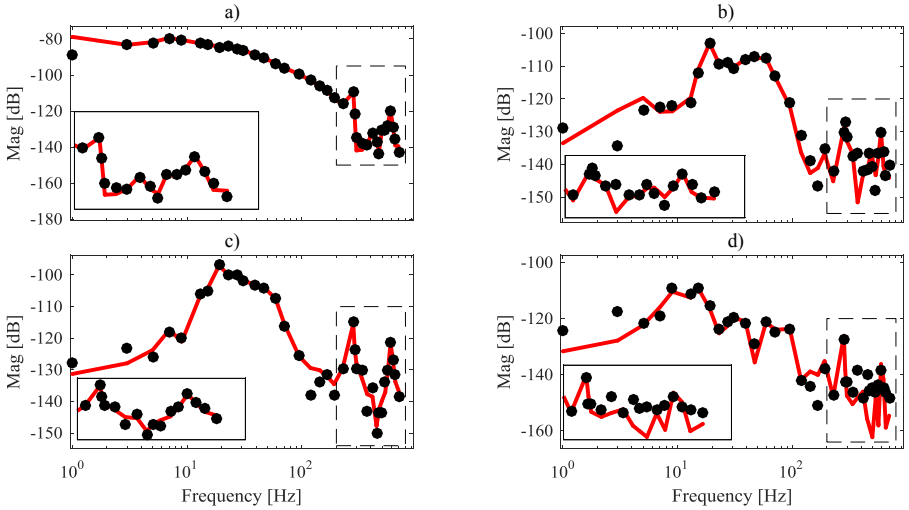

Fig. 6 Comparison of the online (SDFT) and off-line indirectly identified frequency responses in the SIMO case. From the drive end *x*-axis to the a) drive end *x*-axis, b) drive end *y*-axis, c) non-drive end *x*-axis, and d) non-drive end *y*-axis. The red line indicates the off-line indirectly identified model, and the dots show the online model.

the essential system dynamics similarly as the off-line identification approach.

IV. CONCLUSION

The real-time nonparametric closed-loop identification of the AMB system dynamics with an SDFT-based identification approach has been studied and analyzed. The discussion has covered the direct and indirect identification of the SISO and SIMO system dynamics. Based on the results of this paper, the SDFT can track the selected set of frequencies in real time, and more importantly, provide valid estimates of the AMB system dynamics at these frequencies. This property is important as it allows to design the excitation signal so that the SDFT method is feasible for system monitoring and diagnostics purposes, which is of significance in the future research. Adequate online identification method is of great importance as part of fault diagnostics routine in order to obtain information about the rotor faults, which are possible in AMB systems.

The experimental results show that the proposed method is applicable to determination of the frequency responses of the AMB system dynamics in real time on a sample-by-sample basis. Both the direct and indirect approaches have given valid estimates compared with the reference model and the corresponding frequency response obtained by offline identification. More importantly, the results demonstrate that the SDFT is applicable to the SIMO AMB system identification. In the DC region, the indirect identification has a somewhat better correspondence with the reference model than the direct identification. Thus, the indirect identification would be the preferred choice if the controller and the excitation signals were known.

REFERENCES

[1] A. Smirnov, "AMB system for high-speed motors using automatic commissioning," Doctoral dissertation, Lappeenranta University of Technology, Lappeenranta, Finland, 2012.

[2] A. Khader, B. Liu, and J. Sjoberg, "System identification of active magnetic bearing system for commissioning," in *Proc. of Int. Conf. on Model. Iden. and Cont*., Melbourne, Australia, Dec. 2014, pp.289-294.

[3] J. Medina, M. Parada, V. Guzman, L. Medina and S. Diaz, "A Neural Network-Based Closed Loop Identification of a Magnetic Bearings System," in *Proc. of ASME Turbo Expo, Power for Land, Sea and Air*, Vienna, Austria, June 2004, pp. 593–598

[4] A. Noshadi, J. Shi, W. S. Lee, P. Shi and A. Kalam, "System Identification and Robust Control of Multi-Input Multi-Output Active Magnetic Bearing Systems," *IEEE Trans. Contr. Techn..*, vol. 24, no. 4, pp. 1227–1239, July 2016

[5] H. M. N. K. Balini, I. Houtzager, J. Witte, and C. W. Scherer, "Subspace identification and robust control of an AMB system," in *Proc. of American Contr. Conf.*, Baltimore, USA, Jun. 2010, pp. 2200-2205.

[6] C. Gähler, and R. Herzog, "Identification of magnetic bearing systems," in *Proc. of 4th Int. Symp. on Mag. Bear.*, Zurich, Switzerland, Aug. 1994, pp. 293-298.

[7] C. Gähler, M. Mohler, and R. Herzog, "Multivariable identification of active magnetic bearing systems," in *Proc. of 5th Int. Symp. on Mag. Bear.*, Kanazawa, Japan, Aug. 1996, pp. 7-12.

[8] K. Hynynen, "Broadband excitation in the system identification of active magnetic bearing rotor system," Doctoral dissertation, Lappeenranta University of Technology, Lappeenranta, Finland, 2011.

[9] R. Gouws and G. van Schoor, "A current analysis and correction system for vibration forces on the rotor of a rotating active magnetic bearing system," *SAIEE Africa Research Jour.*, vol. 98, no. 3, pp. 101–111, 2007

[10] R. Gouws and G. van Schoor, "A comparative study on fault detection and correction techniques on active magnetic bearing systems," in *Proc. of IEEE Africon*, Windhoek, South Africa, Sep. 2007, pp. 1–9

[11] S-J. Kim and C-W Lee, "On-line identification of current and position stiffnesses by LMS algorithm in active magnetic bearing system equipped with force transducers," *Mech. syst. and signal process.*, vol. 13, no. 5, pp. 681–690, 1999

[12] J. Kejian, Z. Changsheng and T. Ming, "A Uniform Control Method for Imbalance Compensation and Automation Balancing in Active Magnetic Bearing-Rotor Systems," *Jour. of Dyn Sys., Meas. and Control*, vol. 134, no. 2, pp. 1–13, 2011

[13] L. Li, W. Kastner, and F. Worlitz, "Adaptive kalman filter for active magnetic bearings using sofcomputin," in *Proc. of 14th Int. Symp. on Mag. Bear.*, Linz, Austria, Aug. 2014, pp. 91-98.

[14] T. Schuhmann, W. Hofmann, and R. Werner, "Improving operational performance of an active magnetic bearings using kalman filter and state feedback control," *IEEE Trans. Ind. Electron.,* vol. 59, no. 2, pp. 821–829, 2012.

[15] N. Nevaranta, S. Derammelaere, J. Parkkinen, B. Vervisch, T. Lindh, K. Stockman, M. Niemelä, O. Pyrhönen and J. Pyrhönen, "Online Identification of a Mechanical System in Frequency Domain Using Sliding DFT," *IEEE Trans. Ind. Electron.,* vol. 63, no. 9, pp. 5712–5723, 2016.

[16] E. Jacobsen and R. Lyons, "The sliding DFT," *IEEE Signal Processing Magazine*, vol. 20, no. 2, pp. 74–80, 2003.

[17] H-J. Ahn and C-J. Kim, "Frequency domain indirect identification of AMB rotor systems based on fictitious proportional feedback gain," *Jour. of Mech. Science and Techn.*, vol. 30, no. 12, pp. 5389–5395, 2016

[18] R.P. Jastrzebkski, and R. Pöllänen, "Trade offs in LQ/LTR control designs for MIMO AMB systems," In *Proc. of 11th Int. Symp. on Mag. Bear*., 2008, pp. 433–440

[19] R.P. Jastrzebski, T. Sillanpaa, P. Jaatinen, A. Smirnov, J. Vuojolainen, T. Lindh, A. Laiho, and O. Pyrhönen, "Automated design of AMB rotor systems with standard drive, control software and hardware technologies," in *Proc. of 15th Int. Symp. on Mag. Bear.*, 2016, pp. 78–85.

[20] R.P. Jastrzebski, and R. Pöllänen, "Centralized Optimal Position Control for Active Magnetic Bearings – Comparison with Decentralized Control," *Electrical Engineering*, vol. 91, no. 2, pp. 101–114, 2009.

[21] R.P. Jastrzebski, J. Vuojolainen, P. Jaatinen, T. Sillanpaa and O. Pyrhönen, "Commissioning of modular 10kW magnetically levitated test rig," *19th Int. Conf. on Elec. Mach. and Sys*., Chiba, Japan, Nov. 13-16, 2016.

[22] J. Vuojolainen, R.P. Jastrzebski, O. Pyrhönen, "Using a pseudorandom binary sequence for rotor-bearing system identification in active magnetic bearing rotor systems," in *Proc. of 15th Int. Symp. on Mag. Bear.*, 2016, pp. 618–525.

[23] A. C. Wróblewski, J. T. Sawicki and A. H. Pesch, "Rotor model updating and validation for an active magnetic bearing based high-speed machining spinde, " *Jour. Of Eng. For Gas Turb. and Pow*. vol. 65, no.1, pp. 122509, 2012.

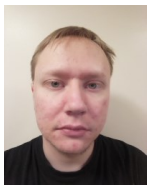

Jouni Vuojolainen received the B.Sc. and M.Sc. degrees in electrical engineering from Lappeenranta University of Technology (LUT), Lappeenranta Finland in 2014 and 2015, respectively, and is currently working toward his doctoral degree in electrical engineering. His current research interests include active magnetic bearing and rotor dynamics identification and application of identification methods to the diagnostics of rotating systems.

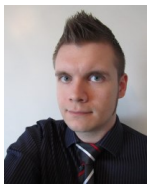

Niko Nevaranta received the B.Sc., M.Sc. and D.Sc degrees in electrical engineering from Lappeenranta University of Technology (LUT), Lappeenranta, Finland in 2010, 2011 and 2016, respectively, where he is currently working as a Post-Doctoral Researcher.

His research interest includes modeling and control of electrical drives, motion control, system identification, parameter estimation, system monitoring, and diagnostics.

Rafal Jastrzebski received the M.Sc. and D.Sc degrees in electrical engineering from the Technical University of Łódź (TUL), Poland and Lappeenranta University of Technology (LUT), Finland in 2002 and 2007. At LUT he currently holds an Academy Research Fellow position. He has wide experience in the research of active magnetic bearing (AMB) systems, bearingless machines, and particularly, in the development of advanced control to AMB systems.

Olli Pyrhönen received the M.Sc. and D.Sc. degrees in electrical engineering from Lappeenranta University of Technology (LUT), Lappeenranta, Finland, in 1990 and 1998, respectively. Since 2000, he has been a Professor in applied control engineering at LUT. In 2010, he received further teaching and research responsibility in the wind power technology at LUT. He has gained industrial experience as a R&D Engineer with ABB Helsinki from 1990 to 1993 and as a CTO of The Switch from 2007 to 2010. His current research areas include modeling and control of active magnetic bearings, bearingless machines, renewable power electronics, and electrical drive systems.

Publication IV

Vuojolainen, J., Nevaranta, N., Jastrzebski, R., and Pyrhönen, O.
Comparison of Excitation Signals in Active Magnetic Bearing System Identification

Reprinted with permission from
Modeling, Identification and Control
vol. 38, no. 3, pp. 123–133, 2017

Modeling, Identification and Control, Vol. 38, No. 1, 2017, pp. 1–11, ISSN 1890–1328

Comparison of Excitation Signals in Active Magnetic Bearing System Identification

Jouni Vuojolainen [1] Niko Nevaranta [1] Rafal Jastrzebski [1] Olli Pyrhönen [1]

[1] *Department of Electrical Engineering, Lappeenranta University of Technology, FI-53851 Lappeenranta, Finland*
E-mail: jouni.vuojolainen@lut.fi, niko.nevaranta@lut.fi, rafal.jastrzebski@lut.fi, olli.pyrhonen@lut.fi

Abstract

Active magnetic bearings (AMBs) offer frictionless suspension, vibration insulation, programmable stiffness, and damping, among other advantages, in levitated rotor applications. However, AMBs are inherently unstable and require accurate system models for the high-performance model-based multi-input multi-output control of rotor position. Control electronics with high calculation capacity and accurate sensors of AMBs provide an opportunity to implement various identification schemes. A variety of artificial excitation signal-based identification methods can thus be achieved with no additional hardware. In this paper, a selection of excitation signals, namely the pseudorandom binary sequence (PRBS), chirp signal, multisine, and stepped sine are presented, applied, and compared with the AMB system identification. From the identification experiments, the rotor-bearing system, the inner current control loop, and values of position and current stiffness are identified. Unlike recently published works considering excitation-based identification of AMB rotor systems, it is demonstrated that identification of the rotor system dynamics can be carried out using various well-established excitation signals. Application and feasibility of these excitation signals in AMB rotor systems are analyzed based on experimental results.

Keywords: Active magnetic bearings (AMB), magnetic levitation, chirp signal, frequency-domain analysis, multisine, pseudorandom binary sequence (PRBS), stepped sine, system identification

1 Introduction

Excitation signal-based identification routines are of key importance in the commissioning phase of active magnetic bearing (AMB) levitated rotor systems. Accurate models obtained by system identification are needed in order to design high-performance controllers (Noshadi et al., 2016), and they have an increasingly important role for diagnostic (Schuhmann et al., 2012) and monitoring purposes (Quinn et al., 2005), (Aenis et al., 2002), (Tiwiri and Chougale, 2014). A common choice for the excitation signal is a sine-wave-based spectrally rich signal, such as a multisine or swept sinusoid signal with a frequency content covering the desired frequency bands. In addition, a stepped sine is a typical signal choice for AMB commissioning purposes to guarantee rich excitation at a specific frequency at the time.

In the literature covering either modeling or control issues of AMB-levitated rotor systems, sine-wave-based excitation signals have been widely applied in identification experiments to obtain an adequate model for the system dynamics. In (Smirnov, 2012), an automatic commissioning approach for an AMB system has been proposed where stepped sine has been considered as an excitation signal to identify frequency responses. Similarly, in (Ahn et al., 2003), stepped sine has been applied for closed-loop identification to obtain a rigid body model for controller design. In (Hynynen and Jastrzebski, 2009), (Hynynen et al., 2010), optimized multisine signals have been proposed for closed-loop rotor system identification to avoid har-

doi:10.4173/mic.2017.1.1

monics produced by a nonlinear system. Although the commissioning and monitoring of an AMB-supported motor system is mostly based on the use of stepped sine or multisine (Smirnov, 2012)– (Kulesza, 2014), when moving towards advanced online identification routines, other signals such as the pseudorandom binary sequence (PRBS) and chirp should also be considered. Despite the extensive research in the field of closed-loop identification of AMB systems, there are only a few studies available where other excitation signals have been applied, or their feasibility to AMB system identification has been discussed. In (Vuojolainen et al., 2016), (Jastrzebski et al., 2016b), the PRBS has been introduced to study high-frequency bending modes in rotor dynamics. In addition, in (Garcia et al., 2016), PRBS is used for performance assessment of a bearingless motor to identify sensitivity functions. Moreover, in (Noshadi et al., 2016), (Inman et al., 2005), (Wroblewski et al., 2012), (Fang et al., 2013), (Tang et al., 2016), and (Lanzon and Tsiotras, 2005), chirp has been applied for the identification of rotor system dynamics. However, these studies do not provide any analysis of the obtained frequency responses as the main focus is on the identification for control, in other words, the models are evaluated to be representative in frequency regions that are relevant for control design purposes.

Despite the wide practical application of excitation-based identification routines for AMB systems, it appears that no papers have compared or discussed the applicability of different excitation signals for such a complex plant. In this paper, the feasibility of different types of excitation signals for identification of an AMB-levitated rotor system is studied. The excitation signals under consideration are PRBS, chirp signal, multisine, and stepped sine. An experimental six-degree-of-freedom modular AMB rotor system is taken as a test case machine. Based on the experimental identification results obtained with various excitation signals, the rotor dynamics, the inner current control loop dynamics, and the position stiffness and current stiffness values are identified for time-continuous linear models. These values are used to validate the identification results, and more importantly, a comparison between the different excitation signals is provided for the first time for such a comprehensive and complex plant model. Moreover, the identified position and current stiffness values are compared with static measurements using a force gauge, which is another key contribution of this paper. It is pointed out that the results presented in this paper are of importance in coupled AMB rotor model identification, levitation system diagnostics, and monitoring.

The paper is constructed as follows. First, the properties of all the excitation signals under study, namely the PRBS, chirp signal, multisine, and stepped sine are introduced and described in Section 2. After that, an identification problem of an active magnetic bearing system is discussed in Section 3 in brief. In Section 4, the experimental conditions for all excitation signals are given and identification results for the rotor-bearing system, inner current control loop, and position and current stiffness values are reported. Finally, conclusions are drawn by comparing the frequency responses and the estimated stiffness values obtained from the identification experiments with different excitation signals.

2 Excitation signals

Sufficiently rich excitation signals, in other words, generators of persistent excitation are of key importance to guarantee informative input-output data for system identification. Naturally, depending on the identification problem, distinct criteria direct the choice of the excitation signal Pintelon and Schoukens (2012). This paper studies closed-loop identification of an AMB-levitated system using various excitations signals.

2.1 PRBS

Pseudorandom binary sequence (PRBS) shown in Fig. 1 a) is an excitation signal that is deterministic and periodic and varies between two levels, amplitudes $+A$ and $-A$. The PRBS is easy to generate, and it has controllable spectral energy, a high spectral energy over a wide band range, and an optimal spectrum for the excitation signal. The basic PRBS is defined by the number of cells d and the selected excitation frequency f. With the number of cells d, the length N of the PRBS is calculated as

$$N = 2^d - 1. \tag{1}$$

The frequency resolution f_r of the PRBS is calculated by

$$f_r = \frac{f_s}{N}. \tag{2}$$

where f_s is the sampling frequency. The number of data points L needed to save the PRBS identification data is

$$L = \frac{N f_s}{f}. \tag{3}$$

The maximum length N is limited by the maximum available L and the ratio f_s/f, as seen in (3). Now, if we want to increase f_r defined by (2), this can be achieved with a higher f_s, a higher f, and a lower N.

2.2 Chirp

Chirp signal (see Fig. 1 b)), also known as sweep or swept signal, is an identification excitation signal in which the frequency is swept up or down in one period. Chirp signals are typically divided into two groups: linear, in which the frequency of the signal varies linearly with time, and exponential/geometrical, in which the frequency varies with geometric progression. In this paper, a linear chirp signal with a sinusoidal waveform is applied. The instantaneous frequency of the linear chirp signal can be calculated by

$$f(t) = f_0 + kt, \tag{4}$$

where f_0 is the starting frequency, t is the current time, and k is the rate of frequency change, which can be obtained by

$$k = \frac{f_1 - f_0}{T}, \tag{5}$$

where f_1 is the final frequency and T is the final time after the sweep from f_0 to f_1. The equation of the sine chirp signal is Pintelon and Schoukens (2012)

$$u(t) = A \cdot \sin\Big(2\pi \cdot \big(f_0 t + \frac{k}{2} t^2\big)\Big), \tag{6}$$

where A is the amplitude of the chirp signal. Chirp signals have been widely applied in AMB identification owing to their main advantage Inman et al. (2005)–Lanzon and Tsiotras (2005): at least to some degree, the frequency content of the signal can be controlled, and hence, its power can be concentrated on a specific frequency range, in other words, regions that are relevant for control design purposes.

2.3 Multisine

A multisine signal depicted in Fig. 1 c), with phases of the sine waves chosen randomly from the interval [0, 2π], can be determined by

$$u(t) = \sum_{n=1}^{N_\mathrm{f}} A_n \cdot \cos(2\pi f_n t + \phi_n), \tag{7}$$

where N_f is the total number of frequencies over n indices, A_n is the amplitude, f_n is the frequency, and ϕ_n is the phase of the nth sine wave component. When applied to AMB system identification, the multisine signal must be carefully designed as discussed in Hynynen and Jastrzebski (2009), Hynynen et al. (2010), where the excitation signal amplitude content has been designed to avoid the harmonics produced by the nonlinearities in the system. By adopting the same guidelines, the multisine signal implemented in this study is generated by using a maximum of four bands, where the starting and final frequencies, the frequency resolution, and the amplitude can be chosen freely for each band.

2.4 Stepped Sine

Stepped sine is a type of sine wave that has all the power at one frequency only as illustrated in Fig. 1 d). Therefore, several frequencies have to be excited separately to cover the required frequency range. Each component has a frequency f_n and an amplitude A_n, which, in general, can be chosen freely. The equation of the stepped sine wave is

$$u(t) = A_n \cdot \sin\Big(2\pi \cdot f_n t\Big), \tag{8}$$

In this paper, an adaptive amplitude stepped sine is considered where the frequency f_n is selected freely, but the amplitude A_n is adjusted to get an acceptable response and to keep the system in the linear region Smirnov (2012). The method is based on prespecified minimum and maximum limits in which the amplitude of the signal is controlled until a desirable value is reached.

3 Identification of an Active Magnetic Bearing System

Owing to its unstable open-loop system dynamics, an active-magnetic-bearing-supported rotor system is a typical example of a closed-loop identification problem. Naturally, the excitation signal can be superposed to different locations of the control structure, that is, the reference or controller output, in order to identify an open-loop plant model or analyze different properties (sensitivities) of the achieved closed-loop system Larsonneur (2009).

In Fig. 2, a block diagram of the closed-loop controlled AMB system illustrates the excitation and signal locations considered in this paper, where r_u denotes the excitation signal at the position control output, which is summed with the control current constituting the plant input u_1. The measured current of the AMB is denoted by y_1 and the rotor position by y_2.

It is emphasized that the AMB system identification must be carried out during system levitation, when the feedback control is operating actively Larsonneur (2009). In this paper, the transfer functions are identified by a direct approach, where the influence of the feedback is omitted. The main advantage of this approach is that the knowledge of the controller is not needed, but depending on the identification problem, it has the disadvantage leading to biased estimates

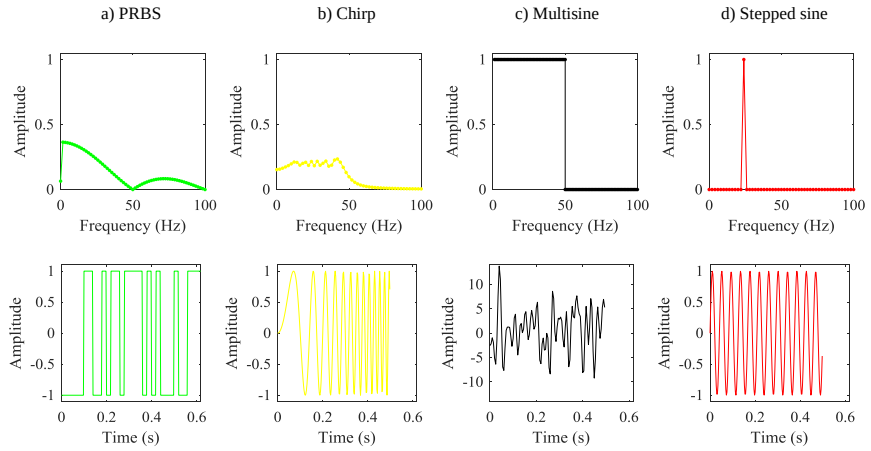

Figure 1: Comparison of the excitation signals in the frequency (upper row) and time domains (bottom row).

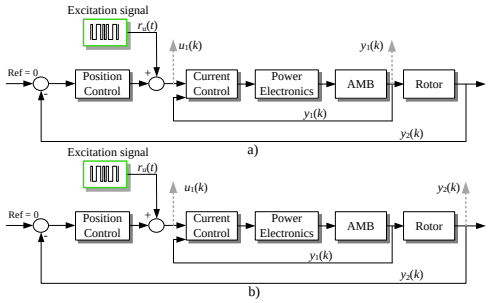

Figure 2: Block diagram of the AMB system with input and output signals used in the identification (dotted grey lines). a) Identification of bearing (current control loop) dynamics using the current reference signal $u_1(k)$ and the measured current $y_1(k)$ and b) identification of rotor-bearing dynamics using the current reference signal $u_1(k)$ and the measured position signal $y_2(k)$.

in some cases. Alternatives for a direct approach include an indirect approach and a joint-input-output approach Hynynen (2011). In the indirect approach, the closed-loop transfer function from the reference signal to the plant output is estimated. In the joint-input-output approach, the transfer function is estimated with the reference signal, and both the plant input and output are considered as outputs. It is pointed out that direct identification has provided accurate models for controller design of an AMB system in several papers Aenis et al. (2002), Smirnov (2012), Vuojolainen et al. (2016), Jastrzebski et al. (2016b), and Wroblewski et al. (2012), and therefore, the same approach is considered here. Moreover, the empirical transfer function estimation (ETFE) is used for the transfer function identification in this paper. The transfer functions are estimated for the SISO case only, that is, by exciting one current reference input of the system and then the dynamics are identified from the measured outputs.

4 Experimental Results

An AMB test rig is used to test PRBS, chirp signal, multisine, and stepped sine excitation signals. The AMB test rig consists of two radial and one axial AMB, resulting in a six-DOF system. The picture of the test rig is shown in Fig. 3. The test rig is discussed in detail in Jastrzebski et al. (2016b), where the stable rotational operation is shown.

All excitation signals are generated by Simulink in the Beckhoff TwinCAT environment. The Beckhoff TwinCAT environment is described in more detail in Jastrzebski et al. (2016a). The PRBS, chirp signal, and multisine are limited to a one-second period based on the memory consumption considerations, and the number of periods of the excitation sequence has to be at least two. This is because the first period is the transient period, and the data points related to this

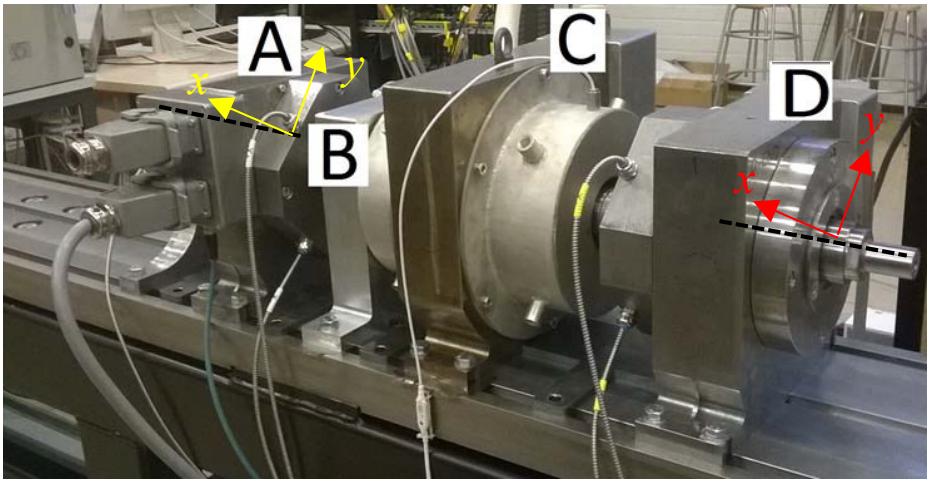

Figure 3: Experimental test rig. A) radial bearing non-drive-end, B) axial bearing, C) induction motor, and D) radial bearing drive-end.

period are discarded as they lead to incorrect results. Naturally, if three or more periods are used, an average over the periods is calculated and saved to increase the signal to noise ratio (SNR) and to minimize the effect of measurement errors.

In this paper, the excitation signals are designed with the following properties. The PRBS signal has a frequency of 3.33 kHz with eleven cells, resulting in a frequency resolution of 1.63 Hz. The amplitude is 2.5 A, and ten periods are collected. The chirp signal has a starting frequency of 5 Hz and a final frequency of 1 kHz. The amplitude is chosen as 1.0 A, and a one-second sweep and ten periods are considered. Again, the multisine signal has four bands, and ten periods are recorded. The first band is from 1 Hz to 19 Hz in 2 Hz steps with an amplitude of 10 mA. The second band is from 23 Hz to 199 Hz in 4 Hz steps, the amplitude being 50 mA. The third band is from 203 Hz to 399 Hz in 2 Hz steps, and the amplitude is 80 mA. Finally, the fourth band is from 403 Hz to 698 Hz in 5 Hz steps, and the amplitude is set to 120 mA. The stepped sine has a frequency range from 1 Hz to 750 Hz, and 250 points are used. Thus, the frequency resolution is 3.01 Hz while the maximum amplitude is 2.5 A.

4.1 Rotor-Bearing System Identification

To identify the rotor-bearing system, excitation is applied at the reference control current as depicted in Fig. 2 b). The plant input $u_1(k)$ and output $y_2(k)$ signals are measured for the corresponding axis, and the open-loop transfer function from the reference control current to the rotor displacement is obtained. This open-loop transfer function can be written as

$$G(\mathrm{j}\omega) = \frac{Y_2(\mathrm{j}\omega)}{U_1(\mathrm{j}\omega)}, \tag{9}$$

where $Y_2(\mathrm{j}\omega)$ and $U_1(\mathrm{j}\omega)$ represent the Discrete Fourier Transform (DFT) of the input and output signals. After the open-loop plant transfer functions have been obtained according to all of the identification results with different excitation signals, a comparison is made with the rotor transfer function of the Finite Element Method (FEM) model. In this paper, the FEM model is considered as a mathematical reference model that is based on the rotor dimensions. The obtained frequency responses from the identification experiments using different excitations are shown in Fig. 4. In addition, a zoom is taken from the frequency range {220, 800} Hz covering the flexible dynamics to compare the estimated frequency response.

Based on the identified frequency responses on the drive-end x- and y-axes (DX and DY), all excitation signals yield a similar accuracy compared with the FEM model on the slope to the first resonance frequency (frequency range from 10 Hz to 280 Hz). As expected, after the first resonance frequency, all the estimated frequency responses start to diverge from the FEM model results. Nevertheless, it is important to notice that the identification tests carried out with different excitation signals are still able to identify the

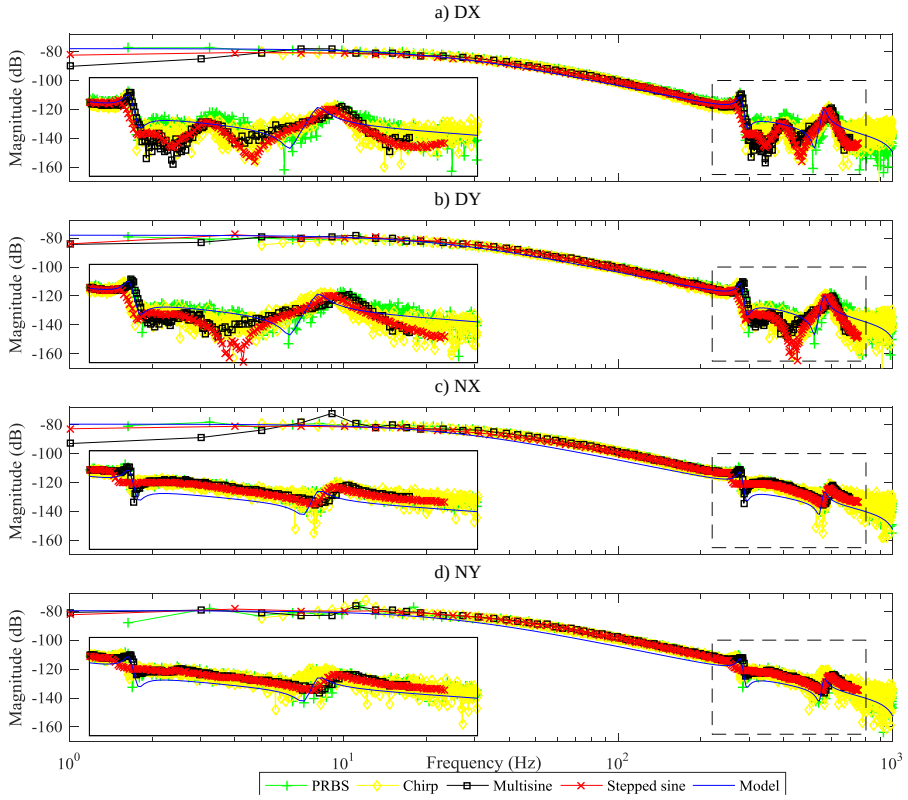

Figure 4: Comparison of the open-loop transfer functions of the rotor-bearing system. DX and DY denote the drive-end x-axis and y-axis, and NX and NY denote the non-drive-end x-axis and y-axis, respectively.

second resonance frequency located at 560 Hz. In the frequency range from 1 Hz to 10 Hz, which refers to the DC gain values, there is some variation between the identification methods.

Again, based on the identification results given in Fig. 4 c) and d), all of the tested excitation signals yield a similar accuracy from the slope to the second resonance frequency compared with the FEM model on the non-drive-end x- and y-axes (NX and NY). However, there is a noticeable offset between the FEM model and the identification results in this frequency range. Reasons for this are the nonlinear gain and steady-state errors in the inner current control loops and the uncertain transportation and PWM delay in the applied industrial drives connected through the CAN bus. Variation in the parameters of the inner current control loops is observed in the explicit inner-loop frequency-based identification and the static identification.

4.2 Inner Current Control Loop Identification

In the inner current control loop identification, excitation is applied at the reference control current as depicted in Fig. 2 a). The plant input u_1 and output y_1 signals are measured for the corresponding axis, and the open-loop transfer function from the reference control current to the rotor displacement is generated. This transfer function can be written as

$$G(\mathrm{j}\omega) = \frac{Y_1(\mathrm{j}\omega)}{U_1(\mathrm{j}\omega)}. \tag{10}$$

where $Y_1(\mathrm{j}\omega)$ represents the DFT of the output signal $y_1(k)$. The estimated frequency responses are compared with an approximated model for the inner con-

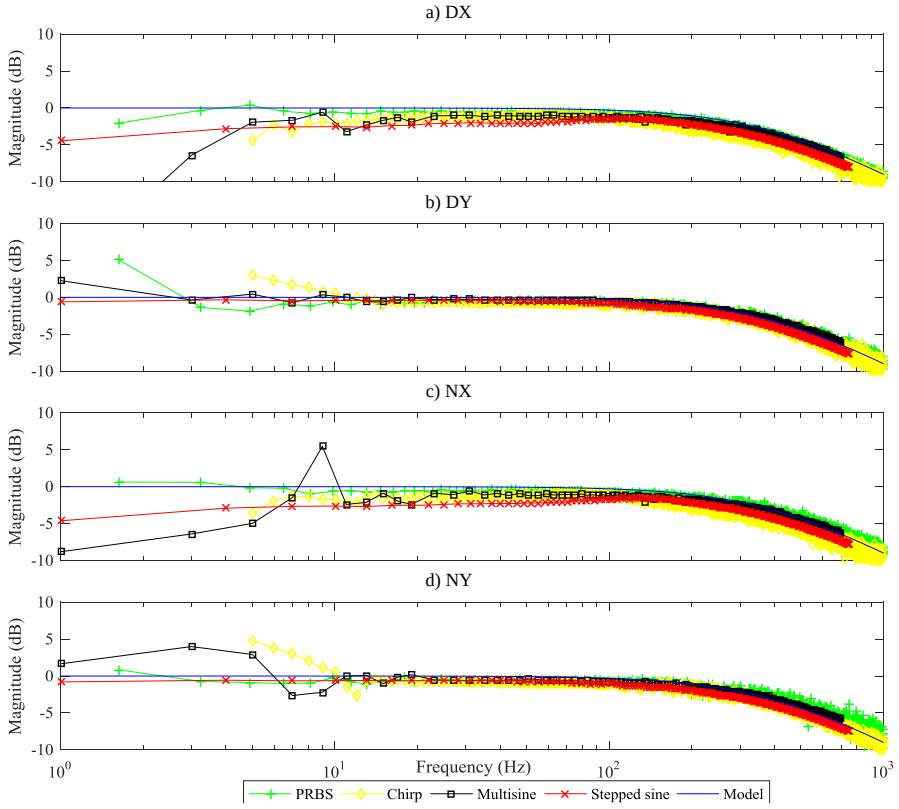

Figure 5: Comparison of the inner current control loop transfer functions. DX and DY are the drive-end x-axis and y-axis, respectively. NX and NY are the non-drive-end x-axis and y-axis, respectively.

trol loop expressed as

$$G_m(\mathrm{j}\omega) = \frac{\omega_1}{\mathrm{j}\omega + \omega_1}, \tag{11}$$

where ω_1 is the cutoff frequency, in this case 380 Hz. This first-order approximation can be considered accurate enough for the inner current control loop model. A comparison between the frequency response functions obtained with the PRBS-, chirp-signal-, multisine-, and stepped-sine-based identification experiments and an approximated model based on (11) of the inner current control loop are shown in Fig. 5.

It can be seen that all the identification results are in good correspondence with the approximated model. On average, above the 100 Hz frequency, all excitation signals yield similar results. As expected, the largest discrepancy between the estimated frequency responses is observable in the frequency range below 100 Hz. Especially, on the non-drive-end and drive-end x-axes (NX and DX), the multisine and stepped sine produce different results in this frequency range compared with the results obtained from other experiments. This can be explained by the difference between the excitation signals, in this case the amplitudes in this specific frequency region. Nevertheless, the results obtained from different identification experiments are in a satisfactory agreement, thereby indicating that similar system dynamics can be estimated.

4.3 Position and Current Stiffness Identification

In this paper, the identification results are validated by estimating a parametric modal model for the rigid part. In general, the parameter estimation of rigid and flexible modal models of AMB-supported rotor systems

can be treated separately Hynynen (2011) and Gahler et al. (1997). The general analytical parametric model for the rigid modes can be expressed in the form Hynynen (2011)

$$G_{\mathrm{r}}(\mathrm{j}\omega) = \frac{(s^2 - z_1^2)}{(s^2 - p_1^2)(s^2 - p_2^2)}, \tag{12}$$

where z and p represent the zeros and poles of the system. The rigid model dynamics can be expressed with the position stiffness values k_{xD} and k_{xN} and the current stiffness values k_{iD} and k_{iN}, and thus, these are chosen as parameters to be estimated. Moreover, by considering certain fixed system dynamics, (12) can be derived for the drive-end x- and y- axis as

$$G_{\mathrm{r,D}}(\mathrm{j}\omega) = \frac{k_{iD} \cdot d(s^2 - c(k_{xD} + k_{xN}))}{(s^2 - a(k_{xD} + k_{xN}))(s^2 - b(k_{xD} + k_{xN}))}, \tag{13}$$

and correspondingly, for the non-driven end x- and y-axes

$$G_{\mathrm{r,N}}(\mathrm{j}\omega) = \frac{k_{iN} \cdot d(s^2 - c(k_{xD} + k_{xN}))}{(s^2 - a(k_{xD} + k_{xN}))(s^2 - b(k_{xD} + k_{xN}))}. \tag{14}$$

It is pointed out that now the parameters a, b, c, and d describe the above-mentioned fixed system dynamics, that is, the parameters contain information about the sensor and actuator locations and transformation of the modal parameters into physical coordinates. In this paper, the fixed denominator parameters for the AMB system under study are $a = 0.05453$ and $b = 0.08494$ for both the drive-end and non-drive-end rigid models. The numerator fixed parameters c and d, instead, are slightly different for the drive end ($c = 0.06880$,$d = 0.1162$) and non-drive end ($c = 0.06873$,$d = 0.1168$), respectively. All these fixed parameters are constant assuming that changes are only made to the position and current stiffness values and are thus different for different rotor-bearing models.

By selecting M frequency points, the best fit for the position and current stiffness values of the analytical models can be iteratively searched by minimizing the error function. Naturally, the general form of the error function is the same for all axes, and thus, here the drive-end x-axis is given as an example

$$J_{\mathrm{DX}}(\boldsymbol{\theta}) = \sum_{i=1}^{M} w_i |G_{\mathrm{e,DX}}(\mathrm{j}\omega_i) - G_{\mathrm{r,D}}(\mathrm{j}\omega_i, \boldsymbol{\theta})|^2, \tag{15}$$

where $\boldsymbol{\theta} = [k_{iD}\ k_{xD}\ k_{iN}\ k_{xN}]$ is the parameter vector to be estimated, $G_{\mathrm{e,DX}}(\mathrm{j}\omega)$ are the experimental frequency response data, and w_i is a weighting function. Motivated by the method presented in Wroblewski et al. (2012), where flexible modes of a FEM model have been updated based on identification experiments, in this paper, the rigid model is fitted by considering the well-known Nelder-Mead function minimization method and excitation frequencies in the frequency range of only {1, 200} Hz as these frequencies correspond mainly to the rigid model. Both the drive-end x- and y-axes and the non-drive-end x- and y-axes are fitted the same, and thus, the total error function is written as

$$J_{\mathrm{tot}}(\boldsymbol{\theta}) = J_{\mathrm{DX}}(\boldsymbol{\theta}) + J_{\mathrm{DY}}(\boldsymbol{\theta}) + J_{\mathrm{NX}}(\boldsymbol{\theta}) + J_{\mathrm{NY}}(\boldsymbol{\theta}). \tag{16}$$

For the PRBS, $M = 122$ frequency points are used, for the chirp $M = 196$, for the multisine $M = 54$, and for the stepped sine $M = 67$. The weighting function w_i is selected so that the frequencies in the range of {10, 100} Hz are weighted with 2.5 and the other frequencies with 1.

The identified position and current stiffness values are also compared with static measurements with a force gauge. A force gauge manufactured by PCE Instruments, type PCE-FB2k, model H3-C3-300kg-3B, is used. This force gauge has a measuring range up to 2000 N and a resolution of 0.5 N. For the measurement, the rotor is connected with an elastic rope to a crane. The force gauge is connected between the rope and the crane. A comparison of the identified position and current stiffness values between all the excitation signals and the static measurements is given in Table 1.

Table 1 shows that the results obtained by using different excitation signals provide very similar results for the current stiffness at both the drive and non-drive ends. Compared with the initial assumption in the FEM modeling there is an about 55 % increase. The identification methods provide similar results for the position stiffness at the drive end, but the value of the static measurement is around 2.5 times higher than the identified results. At the non-drive end, the position stiffness value has a higher variation between the identification methods, but the variation is within a reasonable range. Again, the value of the static measurement is around 2.5 times as high as with the identification methods. This can be attributed to the nonlinear behavior of the position stiffness. The applied differential driving mode effectively linearizes the current stiffness but not the position stiffness. An analytical example of this is shown in Fig. 6, where Fig. 6 a) shows the behavior of the current force relation (current stiffness) and Fig. 6 b) the behavior of the position force relation (position stiffness).

To further analyze the estimated parameters, a few remarks should be made. First, the position stiffness

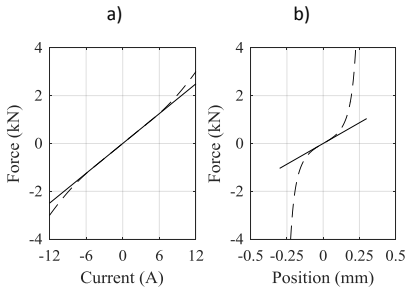

Figure 6: Analytical example of the linearization of (a) current force (current stiffness) and (b) position force (position stiffness) relation. The dotted line indicates the modeled nonlinear behavior and the solid line the assumed linear behavior.

is influenced by the steady state in the inner loops, which can obscure the error in the estimation. Still, it should be noticed that the estimated values are closer to the initial FEM model assumption than the ones obtained from the static position stiffness measurement. Second, the excitation signal has been superposed to the current control reference signal, which has an influence on the position stiffness estimation. For the current stiffness identification, instead, the frequency-domain identification seems to be appropriate as the results with the tested excitation signals are close to the static measurement. The challenges of identifying the stiffness (presented in Table 1), the combined inner current control loop (including PWM), and mechanical runout Kim and Lee (1997) contribute to the dc gain errors of the frequency-dependent plots Fig. 4. Nevertheless, the estimated parameters from the frequency domain observations are reasonable, and a good correspondence between the identification experiments is obtained, indicating that all of the studied excitation signals are suitable for identification of such system dynamics.

5 Conclusion

All the excitation signals presented in this paper, viz. the PRBS, chirp signal, multisine, and stepped sine, were found to be suitable for the identification of the rotor-bearing system, inner current control loop, and the position and current stiffness of an AMB system. The results indicated that all of the compared excitation signals are applicable for AMB system identification, and more importantly, based on the identified frequency responses and estimated stiffness parameters they provide similar results.

Table 1: Estimated Position and Current Stiffness Compared with the Initial FEM Model and Static Measurement with A Force Gauge

Method	k_{xD} [kN/m]	k_{iD} [N/A]	k_{xN} [kN/m]	k_{iN} [N/A]
Initial FEM Model	97.30	19.4	97.30	19.4
PRBS	148.00	31.04	132.00	31.04
Chirp	156.00	31.04	126.00	31.04
Multisine	156.00	31.04	148.00	31.04
Stepped sine	156.00	31.04	155.00	31.03
Static measurement	390.21	30.00	390.21	30.00

To sum up, no final decision could be made on the ’best’ excitation signal for AMB system identification. The decision on the signal to be applied could be made based on the considerations presented in this paper. The authors propose the PRBS for first and fast identification of the system in the commissioning phase, and the stepped sine to obtain more accurate results especially at higher and specific frequencies. The analysis of the excitation signals and their selection have a significant impact on identification, diagnostics, and monitoring of various levitation systems. The obtained results are generalizable to a wide variety of such control systems.

Future research could focus on testing the indirect and joint input-output approach for transfer function identification. Further, the system could be modified so that the excitation could be applied at the position control input. When this modification has been made, the position stiffness identification in the frequency domain could be repeated.

References

Aenis, M., Knopf, E., and Nordmann, R. Active magnetic bearings for the identification and fault diagnosis in turbomachinery. *Mechatronics*, 2002. 12(8):1011–1021. doi:10.1016/S0957-4158(02)00009-0.

Ahn, H.-J., Lee, S.-W., Lee, S.-H., and Han, D.-C. Frequency domain control-relevant identification of mimo amb rigid rotor. *Automatica*, 2003. 39(2):299 – 307. URL http://www.sciencedirect.com/science/article/pii/S0005109802002030, doi:10.1016/S0005-1098(02)00203-0.

Fang, J., Zheng, S., and Han, B. Amb vibration control for structural resonance of double-gimbal control moment gyro with high-speed magnetically sus-

pended rotor. *IEEE/ASME Trans. Mech.*, 2013. 18(1):32–43. doi:10.1109/TMECH.2011.2161877.

Gahler, C., Mohler, M., and Herzog, R. Multivariable identification of active magnetic bearing systems. *JSME International Journal Series C*, 1997. 40(4):584–592. doi:10.1299/jsmec.40.584.

Garcia, J., Gomes, A., and Stephan, R. Performance assessment of a self-bearing motor: an application of iso 14839. In *Proc. of 14th Int. Symp. on Mag. Bear. (ISMB)*. pages 155–158, 2016.

Hynynen, K. *Broadband excitation in the system identification of active magnetic bearing rotor systems*. Ph.D. thesis, Lappeenranta University of Technology, Lappeenranta, Finland, 2011.

Hynynen, K. and Jastrzebski, R. P. Optimized excitation signals in amb rotor system identification. In *IASTED Int. Conf. of Ident., Contr. and Appl.* pages 1–6, 2009.

Hynynen, K., Jastrzebski, R. P., and Smirnov, A. Experimental analysis of frequency response function estimation methods for active magnetic bearing rotor system. In *Proc. of 12th Int. Symp. on Mag. Bear. (ISMB)*. pages 40–46, 2010.

Inman, D. J., Kasarda, M., Quinn, D., Bash, T., Mani, G., Kirk, R., and Sawicki, J. T. Magnetic bearings for non-destructive health monitoring of rotating machinery supported in conventional bearings. In *Dam. Assess. of Struct. VI*, volume 293. pages 383–390, 2005. doi:10.4028/www.scientific.net/KEM.293-294.383.

Jastrzebski, R., Sillanpaa, T., Jaatinen, P., Smirnov, A., Vuojolainen, J., Lindh, T., Laiho, A., and Pyrhonen, O. Automated design of amb rotor systems with standard drive, control software and hardware technologies. In *Proc. of 15th Int. Symp. on Mag. Bear. (ISMB)*. pages 78–85, 2016a.

Jastrzebski, R. P., Vuojolainen, J., Jaatinen, P., Sillanpää, T., and Pyrhönen, O. Commissioning of modular 10kw magnetically levitated test rig. In *19th Int. Conf. on Elecl. Mach. and Syst. (ICEMS)*. pages 1–6, 2016b.

Kim, C.-S. and Lee, C.-W. In situ runout identification in active magnetic bearing system by extended influence coefficient method. *IEEE/ASME Trans. Mech.*, 1997. 2(1):51–57. doi:10.1109/3516.558858.

Kulesza, Z. Dynamic behavior of cracked rotor subjected to multisine excitation. *Journal of Sound and Vibration*, 2014. 333(5):1369 – 1378. URL http://www.sciencedirect.com/science/article/pii/S0022460X13009048, doi:10.1016/j.jsv.2013.10.031.

Lanzon, A. and Tsiotras, P. A combined application of h infin; loop shaping and mu;-synthesis to control high-speed flywheels. *IEEE Trans. Control Syst. Technol.*, 2005. 13(5):766–777. doi:10.1109/TCST.2005.847344.

Larsonneur, R. *Principle of Active Magnetic Suspension*, pages 27–68. Springer Berlin Heidelberg, Berlin, Heidelberg, 2009. URL http://dx.doi.org/10.1007/978-3-642-00497-1_2, doi:10.1007/978-3-642-00497-1$_2$.

Noshadi, A., Shi, J., Lee, W. S., Shi, P., and Kalam, A. System identification and robust control of multi-input multi-output active magnetic bearing systems. *IEEE Trans. Contr. Syst. Tech.*, 2016. 24(4):1227–1239. doi:10.1109/TCST.2015.2480009.

Pintelon, R. and Schoukens, J. *Design of Excitation Signals*, pages 151–175. Wiley-IEEE Press, 2012. URL http://ieeexplore.ieee.org/xpl/articleDetails.jsp?arnumber=6198975, doi:10.1002/9781118287422.ch5.

Quinn, D. D., Mani, G., Kasarda, M. E. F., Bash, T., Inman, D. J., and Kirk, R. G. Damage detection of a rotating cracked shaft using an active magnetic bearing as a force actuator - analysis and experimental verification. *IEEE/ASME Trans. Mech.*, 2005. 10(6):640–647. doi:10.1109/TMECH.2005.859833.

Schuhmann, T., Hofmann, W., and Werner, R. Improving operational performance of active magnetic bearings using kalman filter and state feedback control. *IEEE Trans. Ind. Electron.*, 2012. 59(2):821–829. doi:10.1109/TIE.2011.2161056.

Smirnov, A. *AMB system for high-speed motors using automatic commissioning*. Ph.D. thesis, Lappeenranta University of Technology, Lappeenranta, Finland, 2012.

Tang, E., Han, B., and Zhang, Y. Optimum compensator design for the flexible rotor in magnetically suspended motor to pass the first bending critical speed. *IEEE Trans. Ind. Electron.*, 2016. 63(1):343–354. doi:10.1109/TIE.2015.2472534.

Tiwiri, R. and Chougale, A. Identification of bearing dynamic parameters and unbalance states in a flexible rotor system fully levitated on active magnetic bearings. *Mechatronics*, 2014. 24(3):1011–1021. doi:10.1016/j.mechatronics.2014.02.010.

Vuojolainen, J., Jastrzebski, R., and Pyrhonen, O. Using a pseudorandom binary sequence for rotor-bearing system identification in active magnetic bearing rotor systems. In *Proc. of 15th Int. Symp. on Mag. Bear. (ISMB)*. pages 618–625, 2016.

Wroblewski, A., Sawicki, J., and Pesch, A. Rotor model updating and validation for an active magnetic bearing based high-speed machining spindle. *ASME. J. Eng. Gas Turbines Power*, 2012. 134(12):1–6. doi:10.1115/1.4007337.

Publication V

Nevaranta, N., Vuojolainen, J., Sillanpää, T., and Pyrhönen, O.
Pseudo Random Binary Signal for MIMO Frequency Response Identification of a Magnetically Levitated Rotor System

Reprinted with permission from
IOP Conference Series: Materials Science and Engineering
vol. 643, pp. 012146, 2019

IOP Conf. Series: Materials Science and Engineering **643** (2019) 012146 doi:10.1088/1757-899X/643/1/012146

Pseudo random binary signal for MIMO frequency response identification of a magnetically levitated rotor system

Niko Nevaranta*, Jouni Vuojolainen, Teemu Sillanpää and Olli Pyrhönen

LUT University, FI-53850, Lappeenranta, Finland

* E-mail: Corresponding author: niko.nevaranta@lut.fi

Abstract. High-speed machine technology with magnetically levitated rotor systems has become interesting solution in modern compressor, pump and turbo applications. Often, the commissioning of such machines is system identification-based with injected artificially generated excitation. In this paper a statistically uncorrelated PRBS design is proposed for multi-input multi-output MIMO system that gives the possibility to utilize same PRBS signal for all inputs. The proposed routine is validated with an experimental high-speed generator with active magnetic bearings (AMBs). The obtained frequency responses are validated by comparing the results with the mathematical model.

1. Introduction

System identification based commissioning with artificially generated excitation signals is in a key role in modern high-speed machines with magnetically levitated rotor systems. To obtain high-performance model-based control the identification data is needed to update the model of the rotor system. In general, the literature covering the identification of multiple input multiple output (MIMO) dynamics of such machines the applied excitation signals are based on multi-sine [1], stepped sine [2], chirp [3], [4], [5] or pseudo-random binary signal (PRBS) [6] designs. Typically the identification experiments are simplified and carried out in a single input multiple output (SIMO) or SISO manner. This is often justified, as the model used for control design can be updated based on such experiments. Some studies considers MIMO experiments in AMB systems, but the identification has been carried out in a two degree of freedom (2-DOF) manner [7], [8].

It is well known that, AMB supported rotor system is unstable and nonlinear in nature, hence the identification must be carried out in a closed loop and the nonlinearities has an effect to the obtained results. However, when the identification experiments is carried out in a narrow and almost linear position region, the excitation signal type can be freely selected. In [9] it is shown that different excitation signals produce similar identification results, when applied for commissioning purpose of AMB supported rotor system. This paper addressed issues in MIMO identification experiments of a high-speed machine by considering PRBS excitation signal that is designed to be statistically uncorrelated for MIMO identification experiments. This gives the possibility to inject the same excitation signal design for all the inputs simultaneously. The proposed routine is validated with a high speed machine, namely a 1 MW and 12 500 rpm hermetic steam turbo generator.

2. Identification of flexible rotor system

In Figure 1 the generalized structure of the MIMO closed loop identification is depicted where multiple PRBS excitation signal injection is considered. The PRBS excitation are superposed to the position

control output and signals used for the identification are the excitation and the measured input (current references) and output (positions) signals.

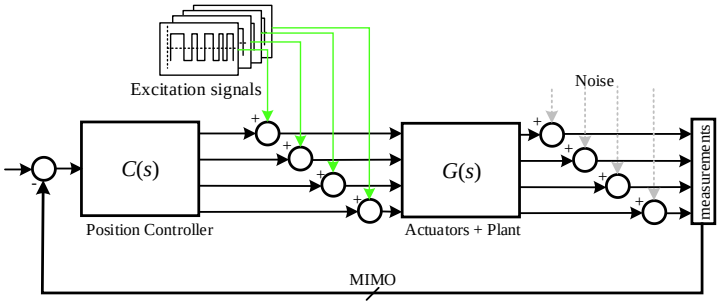

Figure 1. The MIMO closed loop identification experiment.

2.1. Closed-Loop Identification Experiments

The general expression for the direct frequency response estimation from the input and output signals can be expressed by the ratio of spectral density functions as follows

$$G(\mathrm{j}\omega)=\frac{S_{\mathrm{uy}}(\mathrm{j}\omega)}{S_{\mathrm{uu}}(\mathrm{j}\omega)}, \tag{1}$$

where $S_{\mathrm{uy}}(\mathrm{j}\omega)$ is the cross spectral estimate between input $u(t)$ and output $y(t)$ signals and the $S_{\mathrm{uu}}(j\omega)$ is the auto spectral estimate of the input signal. In the case of MIMO systems, the frequency response estimation of p input and q output system can be expressed in a similar form

$$\mathbf{G}^{\mathrm{H}}(\mathrm{j}\omega)_{[p\times q]}=\mathbf{S}_{\mathrm{uu}}^{-1}(\mathrm{j}\omega)_{[p\times q]}\cdot\mathbf{S}_{\mathrm{yy}}(\mathrm{j}\omega)_{[p\times q]}, \tag{2}$$

where $\mathbf{G}^{H}(\mathrm{j}\omega)$ is the Hermitian of the frequency response matrix. The radial controller is a H_∞ type that is tuned based on mixed sensitivity synthesis method. The controller K is found by minimizing

$$\left\|\begin{matrix}\mathrm{W_s S}\\ \mathrm{W_u KS}\end{matrix}\right\|_\infty \le 1, \tag{3}$$

where S is the sensitivity function and W_s is its design weight whereas the W_u is the design weight for the control effort. The sensitivity weight is selected as

$$\mathrm{W_s}(\mathrm{s})=\frac{\frac{\mathrm{s}}{\mathrm{M_s}}+\omega_{\mathrm{B}}}{\mathrm{s}+\omega_{\mathrm{B}}\mathrm{A}}, \tag{4}$$

where the parameter A indicates the steady state error and initially selected as 0.001. The ω_B is the crossover frequency that is here selected as 67.5 rad/s. The $M_s = 2$ is selected that indicates the desired maximum peak of the sensitivity functions. The control effort is limited by following first order weight

$$\mathrm{W_U}(\mathrm{s})=\frac{\mathrm{s}+\frac{\omega_{\mathrm{BC}}}{\mathrm{M_U}}}{\mathrm{A_U s}+\omega_{\mathrm{BC}}}, \tag{5}$$

where ω_{BC} is the controller bandwidth and M_{U} maximum gain of $K(s)S(s)$. Values of $\omega_{\mathrm{BC}} = 10000$, $M_{\mathrm{U}} = 50$ and $A_{\mathrm{U}} = 4$ has been selected for the radial controller control effort design.

2.2. PRBS Design

To design a PRBS signal several good guidelines can be found, like [10]. In the case of MIMO system, the same PRBS can be used if it is time shifted [11] to make them statistically uncorrelated by

$$r_{\mathrm{u,m}}(t)=A_{\mathrm{m}}\cdot u_{\mathrm{PRBS}}(t-\theta_{\mathrm{m}}), \qquad m=1,2,\ldots,p \tag{6}$$

where A_m is the amplitude of the signal, and the time shift can be selected as $\theta_m = N \cdot T_{sw} \cdot (m-1)/p$, where N is the length of the signal with the switching time T_{sw}. The length of the signal is determined by the amount of shift registers d as

$$N = 2^d - 1 \tag{7}$$

An example of a statistically uncorrelated 6-cell PRBS with a switching time of $T_{sw} = 6 \cdot T_s$ (when $T_s = 0.0067$s) design for a system with four inputs is shown in Fig. 2 a), where the time shift of 0.63 seconds is shown with red arrows. The effective band of the PRBS show in Fig. 2 b) can be expressed as

$$f_{BW} = \frac{1}{3 \cdot T_{sw}}, \tag{8}$$

representing the -3 dB drop in the signal. Hence, the frequencies to be covered with the effective band is important to consider in the PRBS design. A practical selection for the PRBS switching time is [12]

$$T_{sw} \approx \frac{2.5}{\omega_{max}}, \tag{9}$$

where ω_{max} can be often taken as a desired bandwidth of the closed loop system. In an AMB supported rotor system the signal should in general cover the frequencies of the rigid modes, and depending on the case, at least the first flexible mode. In Fig. 2 c) the PRBS generator is shown, that is, a maximum length binary signal generator with XOR feedback. Depending on the desired length of the shift register, the optimal maximum length signal is obtained by following the guidelines given in [13].

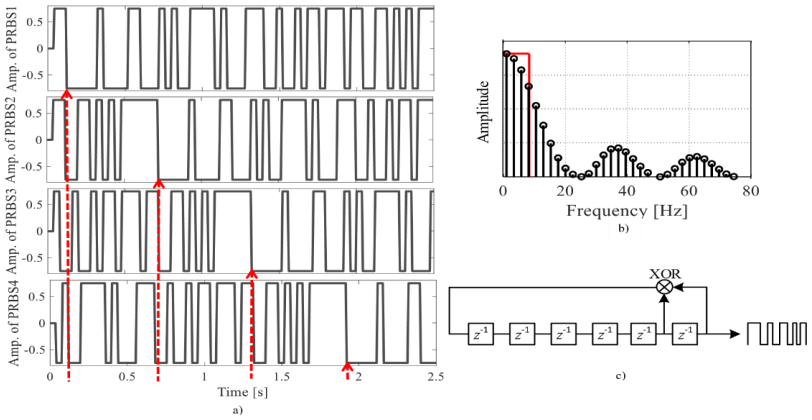

Figure 2. a) Uncorrelated PRBS design for system with four inputs, b) frequency spectrum and c) generation of PRBS.

3. Hermetic steam turbo generator

The high speed turbo generator consist of two main components; the turbine part and the electric machine. The generator is an induction generator with nominal power of 1 MW and 12 500 rpm that is controlled with ACSM1 frequency converters. The control and the excitation signals are implemented by Beckhoff's TwinCAT. The experimental system is shown in Fig. 3 a)–c). The radial and axial bearings are shown in Fig. 3 b) and the main parameters in Table 1.

Table 1. The parameters of axial and radial AMBs.

Value	Axial AMB	Radial AMB 1	Radial AMB 2
Current Stiffness [N/A]	581	170	270
Position Stiffness [N/μm]	5.68	1.19	1.88
Max. Force [N]	1110	1760	6360
Number of poles	2	12	12
Number of winding turns	65	54	85
Material	X20Cr13	SURAM270-35A0	SURAM270-35A

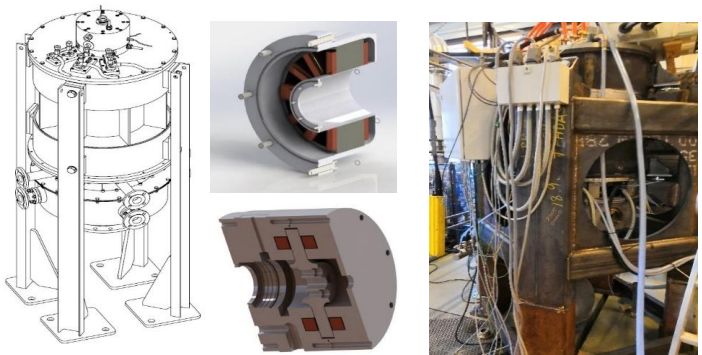

a) b) c)

Figure 3. a) Design of the generator, b) design of the axial and radial AMBs, and c) the experimental generator system.

4. Experimental results

The MIMO identification routine under study is considered during full levitation but without rotation. This stage correspond to initial commissioning step needed for identification for control [14]. The data acquisition and control is operated in a sample level of $T_s = 100\ \mu$s. The 6 times repeated PRBSs are generated with a 15-cell generator operating at $6 \cdot T_s$ with amplitude of 0.5 A. The initial mathematical model based on the mechanical design is used for comparison of the experimental results.

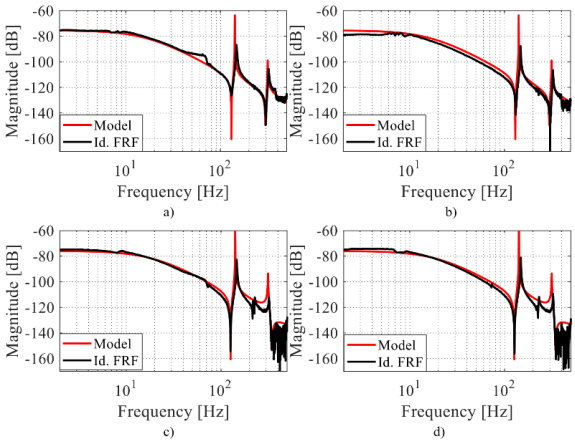

Figure 4. The frequency responses from the identification tests compared to the initial mathematical model; a) from the nondriven end x-axis current to x axis position Nx-Nx, b) Ny-Ny, c) Dx-Dx and d) Dy-Dy.

The experimentally obtained frequency responses (Nx-Nx, Ny-Ny, Dx-Dx, Dy-Dy) are shown in Fig. 4 and compared to the mathematical model of the rotor dynamics. It can be observed that the MIMO PRBS identification experiment provide reasonable results when compared to the modeled ones. The resonances can be clearly seen and the dynamics correspond well to each other. In Fig. 5, the MIMO frequency responses are shown for all input-output pairs of the measurement. The first resonance is clearly visible on all of the responses as well as the cross-coupling dynamics. On the same coordinate axis response but on the different end (e.g Dx-Nx) the responses are more accurate and the second resonance and first/second anti-resonances are also visible in some cases.

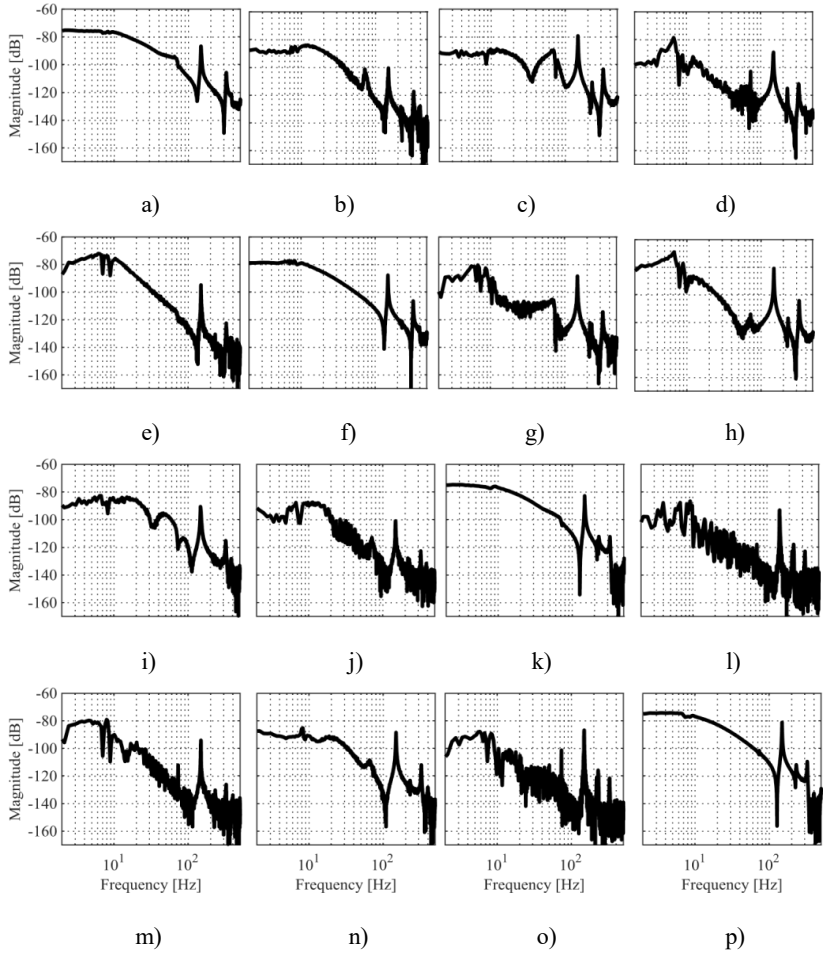

Figure 5. Estimated MIMO frequency response functions from the identification tests.
a) Nx-Nx,
b) Nx-Ny,
c) Nx-Dx,
d) Nx-Dy,
e) Ny-Nx,
f) Ny-Ny,
g) Ny-Dx,
h) Ny-Dy,
i) Dx-Nx,
j) Dx-Ny,
k) Dx-Dx,
l) Dx-Dy,
m) Dy-Nx,
n) Dy-Ny,
o) Dy-Dx,
p) Dy-Dy.

5. Conclusions

This paper studied the commissioning of an AMB supported high-speed generator by applying MIMO identification experiments. A statistically uncorrelated PRBS design was considered as an excitation signal that was injected to the controlled inputs simultaneously. Based on the obtained frequency responses, the proposed PRBS-based identification routine provides straightforward approach for the commissioning of a MIMO system. More importantly, the PRBS gives several advantages for MIMO system identification of AMB dynamics; it is relatively easy to design, implement and generate.

References

[1] Hynynen K 2011 Broadband excitation in the system identification of active magnetic bearing rotor systems," Ph.D. dissertation, LUT University
[2] Smirnov A 2012 Amb system for high-speed motors using automatic commissioning," Ph.D. dissertation, LUT University
[3] Lanzon A and Tsiotras P 2005 A combined application of H∞ loop shaping and μ-synthesis to control highspeed flywheels *IEEE Trans. on Control Systems Techn.* **13(5)** 766–77

[4] Kasarda M, Quinn D, Bash T, Mani G, Inman D J, Kirk R and Sawicki J T 2005 Magnetic bearings for non-destructive health monitoring of rotating machinery supported in conventional bearings *Damage Assessment of Structures VI, ser. Key Engineering Materials* **293** 383-90.
[5] Noshadi A, Shi J, Lee W S, Shi P and Kalam A 2016 System identification and robust control of multiinput multi-output active magnetic bearing systems *IEEE Trans. on Control Systems Techn* **24(4)** 1227–39
[6] Vuojolainen J, Nevaranta N, Jastrzebski R and Pyrhönen O Using a pseudorandom binary sequence for rotor-bearing system identification in active magnetic bearing rotor systems, In Proc. of 15th Int. Symp. on Mag. Bear. (ISMB) 618–25 20176.
[7] Hynynen K, Jastrzebski R P and Smirnov A 2010 Experimental analysis of frequency response function estimation methods for active magnetic bearing rotor system in Proc. of 12th Int. Symp. on Mag. Bear. (ISMB), 40–46.
[8] Hynynen K and Jastrzebski R P 2009 Optimized excitation signals in amb rotor system identification in *IASTED Int. Conf. of Ident, Contr. and Appl.* 1–6.
[9] Vuojolainen J, Nevaranta N, Jastrzebski R, Pyrhönen O. 2017 Comparison of excitation signals in active magnetic bearing system identification *Modeling, Ident. and Control* **38**(3) 123-33
[10] Vilkko T Matti, Roinila 2008 Designing maximum length sequence signal for frequency response measurement of switched mode converters, *Proc .of the Nordic Workshop on Power and Ind.l Electron. (NORPIE/2008)* 1–6
[11] Häggblom K E 2016 Evaluation of experiment designs for mimo identification by cross-validation *IFACPapersOnLine* **49(7)** 308–13.
[12] Pintelon R and Schoukens J 2010 System Identification: A Frequency Domain Approach. Wiley
[13] Pacas M, Villwock S, Szczupak P and Zoubek H 2010 Methods for commissioning and identification in drives *COMPEL - The int. jour. for comp. and math. in electrical and electron. eng.* **29(1)** 53–71
[14] Jaatinen P, Vuojolainen J, Nevaranta N, Jastrzebski R Pyrhönen O. 2019 Control System Commissioning of Fully Levitated Bearingless Machine *Mod, Ident. and Control* 40(1) 27–39.

Publication VI

Jaatinen, P., Vuojolainen, J., Nevaranta, N., Jastrzebski, R., and Pyrhönen, O.
Control system commissioning of fully levitated bearingless machine

Reprinted with permission from
Modeling, Identification and Control
vol. 40, no. 1, pp. 27–39, 2019

Modeling, Identification and Control, Vol. 40, No. 1, 2019, pp. 27–39, ISSN 1890–1328

Control System Commissioning of Fully Levitated Bearingless Machine

P. Jaatinen [1] J. Vuojolainen [1] N. Nevaranta [1] R. Jastrzebski [1] O. Pyrhönen [1]

[1] *Department of Electrical Engineering, Lappeenranta University of Technology, FI-53851 Lappeenranta, Finland*
E-mail: pekko.jaatinen@lut.fi, jouni.vuojolainen@lut.fi, niko.nevaranta@lut.fi, rafal.jastrzebski@lut.fi, olli.pyrhonen@lut.fi

Abstract

The bearingless permanent magnet synchronous motor (BPMSM) is a compact motor structure that combines the motoring and bearing functions based on well-designed integrated windings for generating both torque and magnetic suspension force. In order to achieve a successful high-performance control design for the BPMSM, an adequate model of the rotor dynamics is essential. This paper proposes simplified multiple-input and multiple-output (MIMO) control approaches, namely the pole placement and the linear-quadratic regulator (LQR), that allow to carry out identification experiments in full levitation. Additionally, the stability of the MIMO levitation controller is verified with the rotation tests. Compared with other recently published works, the novelty of this paper is to experimentally demonstrate that a stable fully levitated five-degrees-of-freedom (5-DOF) operation of a bearingless machine can be achieved by the proposed approach, and thereby, options for commissioning of such a system are obtained.

Keywords: Bearingless, magnetic levitation, MIMO control, self-levitating, system identification, 5-DOF

1 Introduction

Operation in the high-speed region is very beneficial especially in the field of compressor applications. The compressor pressure ratio and mass flow rate can be raised by increasing the rotational speed Yoon et al. (2013). In the speed range of 20 000 r/min and over, the electrical motor efficiency can be increased by achieving the minimum weight-power ratio. It is clear that operating in the high-speed region increases both the motor and compressor efficiency. Nowadays there is a growing interest in high-speed technology, where the traditional bearing solution is replaced by a more advanced solution, namely active magnetic bearings (AMBs) Gerhard Schweitzer (2009). The well-known benefits of AMBs are contact-free operation, active control of the rotor, and self diagnostic properties. As AMBs do not need oil lubrication because of the magnetic levitation of the rotor, they are the most suitable solution for oil-free compressor applications in the fields of pharmacy and food industry. However, one drawback of the AMBs is that they extend the total length of the rotor as the radial and axial magnetic bearings need a certain amount of space, which results in an increased axial length of the rotor shaft along with a larger and more complicated motor structure. Depending on the operational speed and rotor mechanical dimensions, this extra length can lower the flexible mode frequencies to the operating region. This is an unwanted feature as the operation close to the flexible mode is difficult. From the viewpoint of the overall system behavior, and especially with respect to controllability, it is advantageous that the rotor does not need to pass flexible modes.

Reducing the rotor length, simultaneously keeping the benefits of the traditional AMBs, a self-levitating or bearingless motor technology can be applied Chiba et al. (2009). In a bearingless motor, one stator pro-

doi:10.4173/mic.2019.1.3

duces both the levitation force to support the rotor and the torque for rotation. This can be achieved by the use of separate windings or by different common winding configurations in one stator unit Chiba et al. (2013). Because the windings are of a three-phase type for both generating torque and levitation force, commercial motor drives can be used, and thus, the amount of power electronics is decreased compared with the traditional AMB configuration.

Bearingless operation is possible also with single-stator disc-shape motors Mitterhofer and Amrhein (2012). Other applications that exploit the benefits of bearingless operation are artificial hearts Hoshi et al. (2006) and canned pump Warberger et al. (2010) applications, where a long air gap length is needed. However, in this paper, a standard horizontal-type machine equipped with two bearings is considered. The machine type with two or more supporting bearings can handle a higher loading force caused by the weight and mass flow of the impeller wheel.

In general, when dealing with high-speed machines, it is important to analyze the rotor behavior Swanson et al. (2008). As a result of the dynamic properties of the rotor structure, bending occurs when the rotation speed is increased. Without qualitative analysis of the rotor dynamics, the rotor operating point in nominal operation can be close to the rotor flexible mode. Thus, it is of great importance that in the machine commissioning phase, the rotor dynamics are identified in order to verify the flexible modes of the rotor Noh et al. (2017). A common method is to use an impulse hammer with vibration sensors to conduct the mode analysis. Naturally, as the AMB system is equipped with a displacement sensor and power electronics, the rotor identification can be made in the system without removing the rotor.

In recent years, a variety of different bearingless machine setups have been introduced in the literature, and their control has become a topic of significant interest. The five-degrees-of-freedom (5-DOF) control of a bearingless machine has been reported in Takemoto et al. (2009); Yamamoto et al. (2011); Severson et al. (2017), and other studies have considered the combination of a bearingless motor and a magnetic bearing in Cao et al. (2017); Schneider and Binder (2007). Here, the 5-DOF operation refers to two radial xy-planes and one axial z-plane of the control axes. Note, however, that many of the reported prototypes are laboratory versions, where all degrees of freedom (DOF) have not been evaluated. It is also worth emphasizing that in these examples the most common structure is a bearingless motor with a ball bearing supporting the other end of the rotor Chiba et al. (2013); Sun et al. (2016a); Ooshima et al. (2015); Yang et al. (2010); Huang et al. (2014). Although there are a few publications where the system has one bearingless motor, it is not shown or reported how the conical movement of the rotor is stabilized Qiu et al. (2015); Sun et al. (2016b); Xue et al. (2015); Yang and Chen (2009); Chen and Hofmann (2011); Cao et al. (2016); Zhang et al. (2016); Zhao and Zhu (2017). In addition, a common factor in all these publications is that they apply PID-based position controllers. To the authors' knowledge, only the model-based controller has been addressed in Messager and Binder (2016) for machines of the horizontal dual bearingless motor type. Another approach based on a linear-quadratic regulator (LQR) controller for a bearingless motor has been introduced in Kauss et al. (2008). However, the presented prototype is 2-DOF and the other end is supported by a ball bearing.

In order to conduct rotor identification, the rotor must be fully levitated. The aim of this paper is to study MIMO control approaches that provide a stable fully levitated operation of a bearingless machine. The novelty of this paper compared with the previously reported studies is that it provides experimental results that show the actual 5-DOF operation of a bearingless machine, and more importantly, introduces results of the full levitation. For this purpose, a 4-DOF MIMO controller is used for the radial position control. The axial position is controlled with an axial AMB, and it is separated from the radial controller. Rigid body is used as an initial rotor model. Pole placement and LQR radial position controllers are used, and the suitability of the controllers is discussed. The designed 4-DOF radial controllers are simulated and tested in a 10 kW dual motor interior permanent magnet bearingless machine. Additionally, the stability of the levitation control is verified with low-speed rotation tests. Finally, system identification experiments are carried out with the pole placement and the LQR controller by superposing a stepped sine excitation signal to the system.

2 Problem statement

To operate in a high-speed region, the dynamic properties of the rotor must be known. An initial analysis of the rotor dynamics is normally done with analytical tools, by which the natural frequencies of the rotor are found. However, experimental tests are mandatory to verify the model and detect possible defects of the rotor. One common method to carry out experimental modal analysis is to use an impulse hammer, which includes for example an integral piezoelectric accelerometer sensor to produce the excitation to the rotor and measure the applied force Kolondzovski et al. (2010). When the rotor system is equipped with AMBs, the

same modal analysis can be done in the system. Similarly as in the impulse hammer test, the AMBs produce the excitation signal and displacement sensors are used to measure the vibration of the rotor. Based on the results, the natural frequencies of the rotor can be found. The obtained results can be used to improve the analytical model by updating the rigid and flexible modes, thereby resulting in a more accurate system model.

To simplify this procedure in a bearingless machine, the rotor can be levitated without a rotating field as the rotor identification is made at a standstill. In this case, the decoupling of the torque and levitation windings can be ignored. When knowing the rotor angle and transforming the three-phase windings into a 2-phase system, the control principles of traditional AMB systems can be adopted.

2.1 System description

The prototype machine consists of two identical interior permanent magnet (IPM) bearingless motors (BMs) together with an axial magnetic bearing. Fig. 1. depicts the prototype machine. The axial magnetic bearing is in the middle of the machine, and bearingless motors are placed on opposite sides of the machine. This provides a symmetrical rotor structure when the load is not considered. A block diagram of the full control system is shown in Fig. 2. The rotor position is measured with an eddy-current sensor differentially from the radial direction and single ended from the axial direction. A non-contact encoder is placed on the right side of the machine to sense the rotor angle. Moreover, five industrial motor drives are used to operate the machine: one is needed for the axial bearing and two for the torque and radial force production for each BM. Each motor drive includes a field programmable gate array (FPGA), where the inner loop current controller is implemented. A block diagram of the inner current control loop is illustrated in Fig. 3. The upper-level control is implemented in a Beckhoff industrial PC, and the communication between the industrial PC and the motor passes through an EtherCAT industrial fieldbus. The sampling time of the control system is 50 μs.

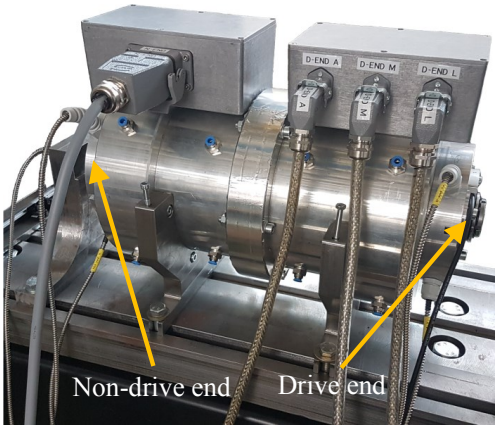

Figure 1: Photograph of the 10kW dual motor bearingless machine. The axial AMB is in the middle of the machine and bearingless motors are located on both ends.

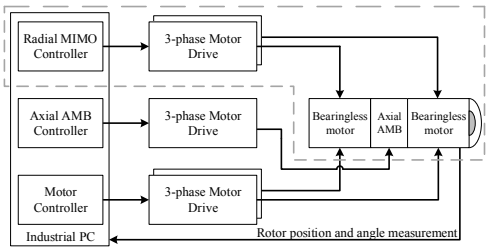

Figure 2: Block diagram describes the overview of the system configuration. All controllers are implemented on a Beckhoff industrial PC shown in far left. In total, five 3-phase motor drives are used to produce levitation force and torque. Three drives are allocated for the 5-DOF levitation purposes, and both motors are driven separately. The rotor position in 5-DOF is measured together with the rotor angular position.

3 Model of the system

In this paper, the rigid rotor model is used to tune the proposed control approaches. In general, a mathematical model of the system can be presented using a state-space representation

$$\begin{aligned} \dot{\mathbf{x}}(t) &= \mathbf{A}\mathbf{x}(t) + \mathbf{B}\mathbf{u}(t) \\ \mathbf{y}(t) &= \mathbf{C}\mathbf{x}(t) \end{aligned} \tag{1}$$

where $\mathbf{A}$ is the system matrix, $\mathbf{B}$ is the input matrix, and $\mathbf{C}$ is the output matrix. The vectors $\mathbf{x}$ and $\mathbf{u}$ are state and input vectors, respectively. In this paper, separate models for the axial and radial directions are used as the coupling is not strong. In the axial direction, the rotor is modeled as a point mass, whereas in the radial direction, a rigid body rotor model is used.

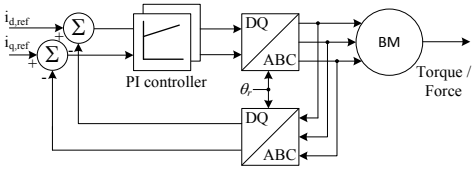

Figure 3: Block diagram of the PI current controller scheme applied to motor drives that produce the radial force. ABC: three-phase reference frame and DQ: rotor reference frame.

3.1 Rotor model

General form of the rotor model is presented in the following:

$$\mathbf{M}\ddot{\mathbf{q}}(t) + (\mathbf{D} + \Omega\mathbf{G})\dot{\mathbf{q}}(t) + \mathbf{K}\mathbf{q}(t) = \mathbf{F}(t), \tag{2}$$

where $\mathbf{M}$ is the mass matrix, $\mathbf{D}$ is the damping matrix, Ω is the rotational speed, $\mathbf{G}$ is the gyroscopic matrix, $\mathbf{K}$ is the stiffness matrix, $\mathbf{F}$ is the force applied to the rotor and $\mathbf{q}$ is the displacement vector of the rotor. This model can be simplified to a rigid rotor model, which describes the rotor movement with respect to the center of the rotor mass Smirnov (2012)

$$\mathbf{M}\ddot{\mathbf{q}}(t) + \Omega\mathbf{G}\dot{\mathbf{q}}(t) = \mathbf{F}(t), \tag{3}$$

where $\mathbf{M}$ is the diagonal matrix including rotor mass and inertia at the center of mass, $\mathbf{q} = \begin{bmatrix} x & y & \alpha_x & \alpha_y \end{bmatrix}^T$ is the vector that describes the rotor position in the xy-axis and the angle around the corresponding axis at the center of mass. As the displacement sensors and the magnetic bearings are not located at the center of mass, a coordinate transformation is needed for the control design and simulation purposes. To acquire the absolute location in the xy-axis of the sensors, $\mathbf{q}_s = \begin{bmatrix} x_{D,s} & y_{D,s} & x_{ND,s} & y_{ND,s} \end{bmatrix}^T$ and the magnetic bearing locations, $\mathbf{q}_b = \begin{bmatrix} x_{D,b} & y_{D,b} & x_{ND,b} & y_{ND,b} \end{bmatrix}^T$ at the drive and non-drive end of the machine, the following transformation matrices are applied

$$\mathbf{q}_b = \underbrace{\begin{pmatrix} 1 & 0 & 0 & -a \\ 0 & 1 & -a & 0 \\ 1 & 0 & 0 & b \\ 0 & 1 & b & 0 \end{pmatrix}}_{\mathbf{T}_b} \mathbf{q}, \quad \mathbf{q}_s = \underbrace{\begin{pmatrix} 1 & 0 & 0 & -c \\ 0 & 1 & -c & 0 \\ 1 & 0 & 0 & d \\ 0 & 1 & d & 0 \end{pmatrix}}_{\mathbf{T}_s} \mathbf{q}, \tag{4}$$

where a, b are the drive-end and non-drive-end bearing locations from the center of the rotor mass, respectively and c, d are the drive-end and non-drive-end sensor locations from the center of mass. Rotor cross-sectional view is illustrated in Fig. 4.

Radial forces produced by the bearingless machine can be presented by the following equation

$$\mathbf{F}(t) = \mathbf{K}_x\mathbf{q}_b + \mathbf{K}_i\mathbf{i}_c, \tag{5}$$

where $\mathbf{F}$ is the total linearized radial force generated by the bearingless machine, $\mathbf{q}_b$ is the rotor position at the bearing location, $\mathbf{i}_c$ is the control current to the levitation windings, $\mathbf{K}_x$ is the diagonal position stiffness matrix, and $\mathbf{K}_i$ is the diagonal current stiffness matrix. The total force depends on the rotor position and current in the levitation windings. The coefficients $\mathbf{K}_x$ and $\mathbf{K}_i$ can be determined experimentally by different tests and measurements. Parameters of the prototype machine are listed in Table 1.

In Fig. 5 a) the position stiffness value is determined by moving the rotor in the air gap, and the force caused by the unbalance pull of the permanent magnets is measured. From this measurement, the slope of the position stiffness can be calculated, $\mathbf{K}_x = \triangle f_x / \triangle P_x$. The current stiffness is measured by applying current in the levitation windings and measuring the corresponding radial force. Similarly, from the measured slope, the current stiffness can be calculated, $\mathbf{K}_i = \triangle f_x / \triangle i_L$. It can be seen that the measured values are closely matching the FEM simulations presented in Fig. 5. Measured values are used in the control design. The force measurement setup is described in more detail in Jaatinen et al. (2016).

The rigid rotor model presented in (3) can be further simplified by neglecting the gyroscopic matrix as the rotor is not rotating during the identification, that is, $\Omega = 0$. Furthermore, this simplification is also valid for the rotating system when axial length of the rotor is much greater than the rotor diameter thus the gyroscopic effect is then negligible Gerhard Schweitzer (2009). By substituting (4) and (5) into (3), a simplified rigid rotor model is achieved

$$\mathbf{M}_b\ddot{\mathbf{q}}_\mathbf{b} = \mathbf{K}_x\mathbf{q}_b + \mathbf{K}_i\mathbf{i}_c. \tag{6}$$

where $\mathbf{M}_b = (\mathbf{T}_b^{-1})^T\mathbf{M}\mathbf{T}_b^{-1}$ is the mass matrix in the bearing plane. In the state-space form, the simplified rotor model is written as

$$\begin{aligned} \mathbf{A}_r &= \begin{bmatrix} \mathbf{0} & \mathbf{I} \\ (\mathbf{M}_b)^{-1}\mathbf{K}_x & \mathbf{0} \end{bmatrix}, \\ \mathbf{B}_r &= \begin{bmatrix} \mathbf{0} \\ (\mathbf{M}_b)^{-1}\mathbf{K}_i \end{bmatrix}, \\ \mathbf{C}_r &= \begin{bmatrix} \mathbf{T_s}\mathbf{T_b^{-1}} & \mathbf{0} \end{bmatrix}. \end{aligned} \tag{7}$$

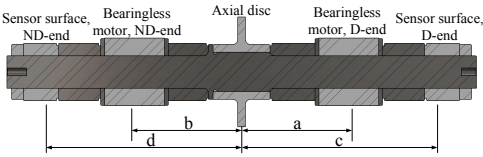

Figure 4: Cross-sectional view of the rotor in the prototype system. Locations of the bearingless motors and the sensor surfaces are measured respect of the center of mass.

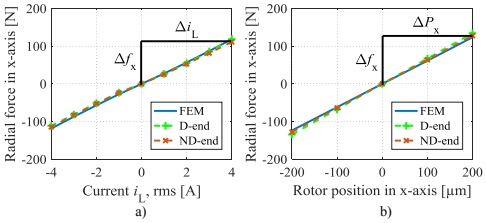

Figure 5: Simulated and measured current and position stiffnesses. The current stiffness can be calculated from the slope presented in a). In the same manner, the position stiffness can be calculated from the slope presented in b).

3.2 Actuator model

The actuator consists of the dynamics of the inner current control loop. A straightforward method to model the actuator dynamics is to use the bandwidth of the current controller

$$G_a = \frac{\omega_{bw}}{s + \omega_{bw}}, \tag{8}$$

where $\mathbf{G}_a$ is the approximate transfer function of the inner current loop and ω_{bw} is the bandwidth of the current controller.

In the simulation, the inner control loop consists of the PI controller, the motor drive model, and the bearingless motor model including the levitation windings. The motor drive is modeled as two-stage switching with a pulse width modulator. The bearingless motor is modeled in the dq reference frame as

$$\begin{aligned} u_d &= Ri_d + \frac{d}{dt}L_d i_d - \omega L_q i_q, \\ u_q &= Ri_q + \frac{d}{dt}L_q i_q + \omega L_d i_d, \end{aligned} \tag{9}$$

where u is the voltage over the levitation windings, R is the resistance of the levitation windings, L is the inductance of the levitation windings, i is the current of the levitation windings, and ω is the electrical angle.

3.3 Full model

A full model can be produced by combining the rotor model with the actuator model.

$$\begin{aligned} \mathbf{A} &= \begin{bmatrix} \mathbf{A}_a & \mathbf{0} \\ \mathbf{B}_r\mathbf{C}_a & \mathbf{A}_r \end{bmatrix}, \quad \mathbf{B} = \begin{bmatrix} \mathbf{B}_a \\ \mathbf{0} \end{bmatrix}, \\ \mathbf{C} &= \begin{bmatrix} \mathbf{0} & \mathbf{C}_r \end{bmatrix}, \end{aligned} \tag{10}$$

where $\mathbf{B}_a = -\mathbf{A}_a = diag\begin{bmatrix}\omega_{bw} & \omega_{bw} & \omega_{bw} & \omega_{bw}\end{bmatrix}$ is the current controller bandwidth, and the rigid rotor model matrices are denoted by the subscript r.

3.4 Axial AMB model

The axial direction of the rotor can be controlled separately as the coupling to the radial direction is negligible in the center of the air gap. As the axial AMB controls only 1-DOF, the model of the rotor can be simplified to a point mass model

$$m\ddot{q} = K_x q_a + K_i i_c, \tag{11}$$

where m is the rotor mass, q_a is the acceleration of the rotor, K_i is the current stiffness, and K_x is the position stiffness.

4 MIMO control of a bearingless machine

In the literature, there are many publications that address the issues of the MIMO control of traditional AMB systems equipped with two radial and one axial AMBs Yoon et al. (2013); Gerhard Schweitzer (2009). The same principles can be adopted to the bearingless machine control. However, there are two major differences compared with the traditional AMB system. Firstly, the rotating magnetic flux that generates the levitating force is synchronous with the rotor rotation. Secondly, decoupling of the motor control from the levitation control is required. If the decoupling parameters are correctly identified, the motor control does not affect the performance of the levitation controller Ooshima et al. (2004). It is emphasized that in this paper, the decoupling controller is not taken into consideration as the rotor identification is conducted with a nonrotating rotor. Moreover, a 4-DOF MIMO radial controller with a PID-type axial controller for commissioning and rotor identification purposes is tuned based on a rigid rotor model.

Table 1: Machine parameters

Parameter	Symbol	Value	Unit
Nominal speed	Ω_{nom}	30 000	r/min
Nominal power per motor unit	P_{nom}	5	kW
Rotor mass	m	11.65	kg
Rotor inertia	J	0.232	kgm^2
Resistance, levitation winding	R	0.27	Ω
Inductance, levitation winding	L	3.27	mH
BM location	a, b	107.5	mm
Position sensor location	c, d	211	mm
Air gap length	l_δ	0.6	mm
Rotor length	l_{r}	480	mm
BM lamination stack length	l_{rl}	61	mm
BM lamination diameter	d_{rl}	68.8	mm
BM stator outer diameter	d_{s}	150	mm
Axial disk thickness	l_{a}	8	mm
Axial disk diameter	d_{a}	112	mm
Rotor shaft diameter	d_{rs}	33	mm
Current stiffness, measured	K_{i}	29	N/A
Position stiffness, measured	K_{x}	672	N/mm
Current stiffness, FEM	$K_{\text{i,FEM}}$	29.6	N/A
Position stiffness, FEM	$K_{\text{x,FEM}}$	618	N/mm
Maximum input deviation	u_{nmax}	2	A
Maximum output deviation	m_{n}	25	µm

Furthermore, an additional coordinate transformation is needed when comparing the bearingless system with the traditional AMB system. In Fig. 6, the principle of the radial force generation both in the x and y directions is shown. Here, the three-phase winding is transformed into a two-phase presentation. When the rotor is in a certain angular position, for instance 0 deg, where the poles are parallel with the stationary xy-reference frame, the corresponding two-phase current produces force in that axis. By changing the polarity of the current, the force direction can be reversed. By taking into account the rotation of the rotor in the coordinate transformation, the force can be generated at any angle. A radial position control-loop block diagram is presented in Fig. 7. Note the coordinate transformation between the position controller and the inner current controller.

4.1 State-feedback control with pole placement

One common control method for handling state equations is state feedback with pole placement, in which the locations of the closed-loop poles are selected to obtain the desired performance. As all states are not measurable, a state estimator is also needed. To remove the steady-state error, an integral state is augmented to the state feedback controller. The full discrete-time state equation can be written Franklin et al. (2010)

$$\begin{bmatrix}\mathbf{x}(k+1)\\ \mathbf{x}_I(k+1)\end{bmatrix} = \begin{bmatrix}\mathbf{\Phi} & \mathbf{0}\\ \mathbf{C} & \mathbf{I}\end{bmatrix}\begin{bmatrix}\mathbf{x}(k)\\ \mathbf{x}_I(k)\end{bmatrix} + \begin{bmatrix}\mathbf{\Gamma}\\ \mathbf{0}\end{bmatrix}\mathbf{u}(k) - \begin{bmatrix}\mathbf{0}\\ \mathbf{I}\end{bmatrix}\mathbf{r}(k), \tag{12}$$

where $\mathbf{\Phi}$, $\mathbf{\Gamma}$ are discretized system state and input matrices, $\mathbf{C}$ is the output matrix, $\mathbf{I}$ is the identity matrix, $\mathbf{x}$ is the system state vector, $\mathbf{x}_I$ is the integral state vector, $\mathbf{u}$ is the system input vector, and $\mathbf{r}$ is the reference input vector. The feedback law is then written as

$$\mathbf{u}(k) = -\begin{bmatrix}\mathbf{K} & \mathbf{K_I}\end{bmatrix}\begin{bmatrix}\mathbf{x}(k)\\ \mathbf{x}_I(k)\end{bmatrix}, \tag{13}$$

where $\mathbf{K}$ is the state feedback gain and $\mathbf{K}_I$ is the integrator gain.

The state estimator uses the following presentation

$$\hat{\mathbf{x}}(k+1) = \mathbf{\Phi}\hat{\mathbf{x}}(k) + \mathbf{\Gamma}\mathbf{u}(k) + \mathbf{L}(\mathbf{y}(k) - \mathbf{C}\hat{\mathbf{x}}(k)), \tag{14}$$

where $\hat{\mathbf{x}}$ is the estimated state vector and $\mathbf{L}$ is the feedback gain of the state estimator. In this paper, the state feedback controller is designed by using the principles presented in Gerhard Schweitzer (2009).

The main drawback of the pole-placement-based tuning is that it is not very intuitive. Secondly, when the system degree increases, also the number of poles to be placed increases, resulting in a more complex tuning problem. This is an important factor to be acknowledged, especially when including flexible modes to the control model.

4.2 Linear-quadratic regulator

There are other control methods that facilitate controller tuning by providing more intuitive tools, which do not need direct manipulation of the poles. One of these optimal control methods is the linear-quadratic regulator (LQR). The controller tuning is based on minimization of the quadratic cost function

$$\mathcal{J} = \frac{1}{2}\sum_{k=0}^{N}[\mathbf{x}^T(k)\mathbf{Q}_1\mathbf{x}(k) + \mathbf{u}^T(k)\mathbf{Q}_2\mathbf{u}(k)], \tag{15}$$

where $\mathcal{J}$ is the cost function, $\mathbf{x}$ is the state vector, $\mathbf{u}$ is the input vector, $\mathbf{Q}_1$ is the output weight function, and $\mathbf{Q}_2$ is the input weight function. The weighting

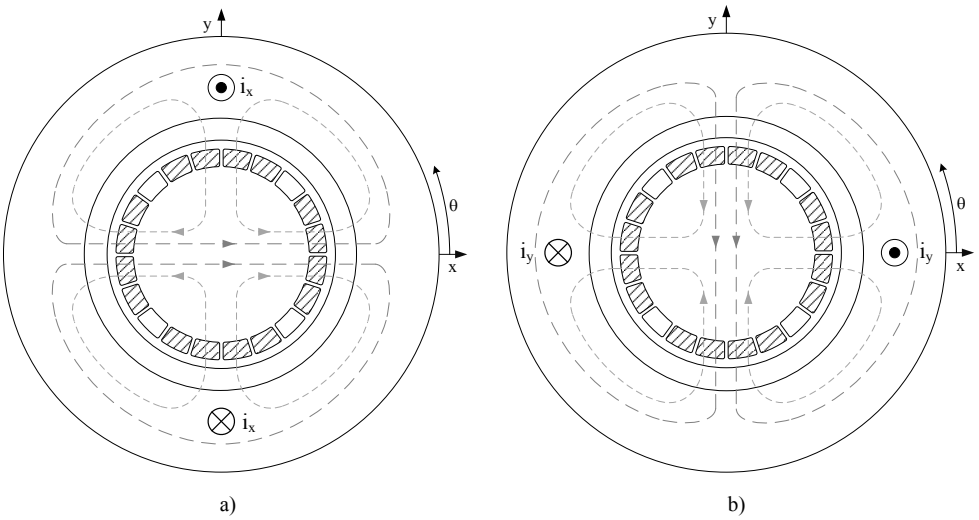

Figure 6: Description of radial force generation in a permanent magnet bearingless motor. The three-phase windings are transformed into a two-phase presentation in the xy plane. The currents of the two-phase windings are denoted by i_x and i_y. The principle of producing radial force in the x-axis is shown in a). By applying current to the x phase windings, the flux is increased and decreased opposite to the air gap in x-axis. This flux unbalance produces the radial force. By applying negative current, the force direction can be reversed. In a similar fashion, the radial force in the y-axis can be produced by applying current in the y-phase winding.

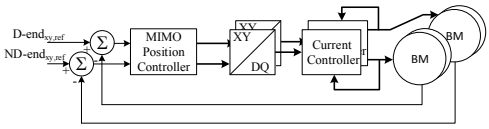

Figure 7: Block diagram of the position control loop.

functions are diagonal matrices that affect the states and inputs of the system. There are different methods to determine the weighting functions $\mathbf{Q}_1$ and $\mathbf{Q}_2$. One of the methods is called Bryson's rule Franklin et al. (2010), where the effect of the state weight on the output follows

$$\mathbf{Q}_1 = \mathbf{C}^T \bar{\mathbf{Q}}_1 \mathbf{C}. \tag{16}$$

The weights are selected for the output by deciding how large a deviation of the output is acceptable

$$\bar{\mathbf{Q}}_{1,n} = \begin{pmatrix} 1/m_1^2 & 0 & \cdots & 0 \\ 0 & 1/m_2^2 & \cdots & 0 \\ \vdots & \vdots & \ddots & \vdots \\ 0 & 0 & \cdots & 1/m_n^2 \end{pmatrix}, \tag{17}$$

where m_n is the maximum deviation of the output signal. The weights for the inputs are selected by the maximum input signal amplitude

$$\mathbf{Q}_{2,n} = \begin{pmatrix} 1/u_{1max}^2 & 0 & \cdots & 0 \\ 0 & 1/u_{2max}^2 & \cdots & 0 \\ \vdots & \vdots & \ddots & \vdots \\ 0 & 0 & \cdots & 1/u_{nmax}^2 \end{pmatrix}, \tag{18}$$

where u_{nmax} is the maximum input signal deviation. Table 1 lists the values selected for the weights m and u based on several simulation iterations.

When designing the LQR-based controller, the degree of freedom is lower (two parameters) than with the pole placement method, where eight poles have to

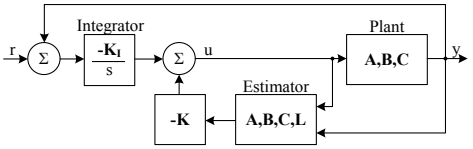

Figure 8: Block diagram of the state feedback controller. A state estimator is necessary for generating the full state vector including rotor acceleration, which is not measurable. Naturally, an integral action is added to remove the steady-state error.

be selected. This difference is amplified in the case of the flexible plant model, where more states are added to the system plant.

5 Experimental Results

Both controllers are tested with the prototype bearingless machine. First, the initial lift-up test is conducted and compared with simulations in Fig. 9. The rotor position is shown during the initial lift-up with the pole placement and the LQR controller. At the beginning of the test, the rotor is resting on the backup bearings, where it is levitated to the center of the air gap. Based on the simulations, it can be noted that the pole placement controller has a higher overshoot, but both controllers provide full levitation.

In Figs. 10 and 11, the current in the dq reference frame is shown for the pole placement controller and the LQR controller during the rotor lift-up sequence. Because of the unbalanced magnetic pull of the embedded magnets in the rotor, a high current peak is needed to lift the rotor away from the backup bearings to the center of the air gap. Based on the results, it can be concluded that both of the proposed controllers meet the requirement of levitating the rotor. It can also be seen that a good correspondence between the simulations and measurements is achieved. From the current RMS values in the steady-state situation we can notice that the LQR controller provides lower current demand. It is pointed out, however, that there is one notable difference between the BMs in the experimental test; the ND-end has a smaller current ripple than the D-end.

5.1 System Identification

As was shown in Fig. 9, both the proposed control approaches provided a stable fully levitated operation of the bearingless machine. Thus, system identification

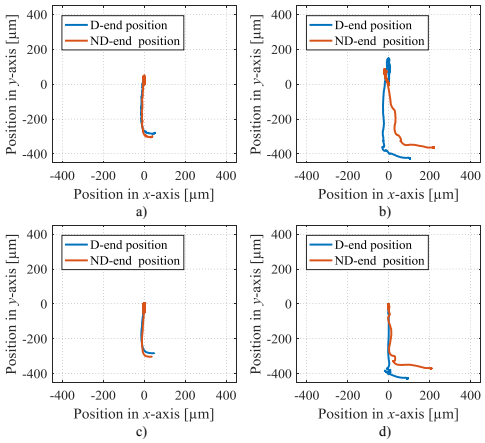

Figure 9: Simulated and measured rotor lift-up from the backup bearings. Initially, the rotor is lying on the backup bearings, and after the controller is enabled, the rotor is magnetically levitated to the operating point, that is the origin $(x, y) = (0, 0)$. Simulation and measurement results for the pole placement controller are shown in a) and b), and for the LQR controller in c) and d).

experiments can be carried out when the rotor is levitating by superposing artificially generated excitation signals to the control system. In this paper, an adaptive amplitude stepped sine signal is considered with a frequency band from 1 Hz to 750 Hz in order to validate the suitability of the control approaches for commissioning purposes. System identification experiments are carried out with both control approaches. In Fig. 12, the experimentally obtained frequency responses are shown. Uncertainty is shown in the low frequency area (<10 Hz) as it is challenging to identify the DC-area with the motor inverter. Also the closed loop controller influences to the low frequency region limiting the accuracy of identification. Nevertheless, identified rotor model for both controllers is matching closely to the initial rigid rotor model. Identified rotor model can be further use in the control design where the flexible part is included. Evidently, the system rotor dynamics can be identified in the full-levitation mode similarly as with the 5-DOF AMB system Vuojolainen et al. (2017).

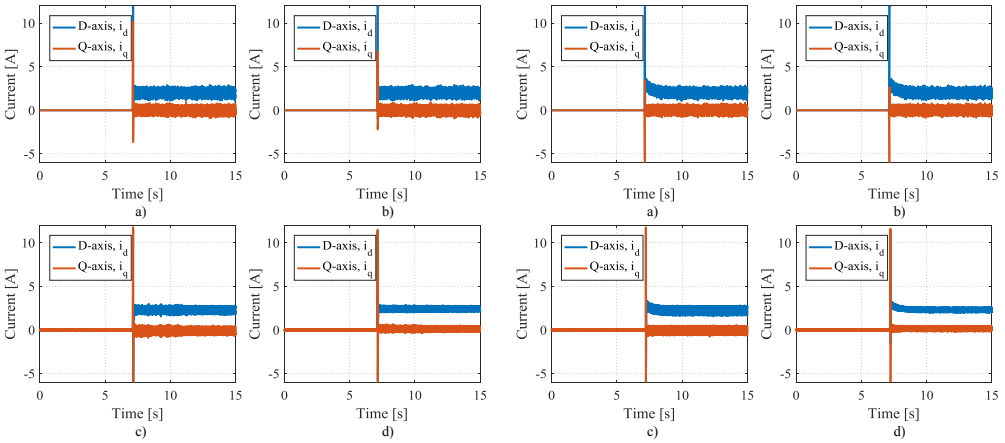

Figure 10: Simulated and measured DQ currents during the rotor lift-up with the pole placement controller. Simulation of the DQ axis current of the D-end and the ND-end motor are shown in a) and b), respectively. The measured DQ axis current of the D-end and the ND-end motor are shown in c) and d), respectively. Steady state RMS values for current in the simulation a) and b) are 2 A. For the measured steady state RMS current values c) 2.3 A and d) 2.4 A.

Figure 11: Simulated and measured DQ currents during the rotor lift-up when using the LQR controller. Simulation of the DQ axis current of the D-end and the ND-end motor are shown in a) and b), respectively. The measured DQ axis currents of the D-end and the ND-end motor are shown in c) and d), respectively. Steady state RMS values for current in the simulation a) and b) are 2 A. For the measured steady state RMS current values c) 2.2 A and d) 2.3 A.

5.2 Rotational tests

To further validate the observations reported in this paper, rotational tests are carried out with modest velocity of 150 and 300 r/min. The measured currents from the motor and levitation coils are shown with the measured position during the rotation test for both speeds in Fig. 13 and Fig. 14. Note, that, for illustrative purposes the rotational test are carried out only with the LQR based control approach. These results clearly indicate that the proposed control approach produces stable levitation also during rotation. Torque for the rotation is produced with the D-end motor windings without the decoupling in the levitation controller. The average fluctuation of the positon measurement during the rotation is 2.5 µm, which is caused by the sensor noise and the runout of the sensor surface together with the unbalance of the rotor. By comparing rotor position measurements in Fig. 13 and Fig. 14 it can be noticed that D-end orbit is affected the most from the rotation speed change. Fundamental orbit change of the rotor position with rotor speed from 150 to 300 r/min is for D-end from 2.15 µm to 2.1 µm and for ND-end 4.5 µm to 3.2 µm. Effect of the cross-coupling between the levitation and the torque windings in D-end is seen from the results.

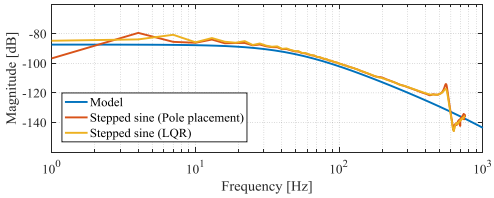

Figure 12: Frequency response plot where the result of the experimental identification with the stepped sine method is compared with the rigid body rotor model. The experimental result shows the first flexible mode peak.

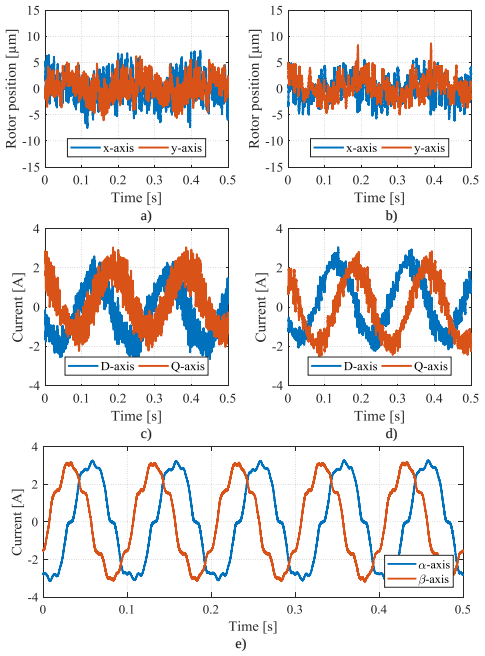

Figure 13: Rotation test with speed of 150 r/min. Measured rotor position is shown for D-end and ND-end in a) and b), respectively. Levitation winding current for D-end and ND-end is shown in c) and d). respectively. Torque producing current in the D-end motor windings is shown in e). The motor currents are represented in $\alpha\beta$ -armature reference frame.

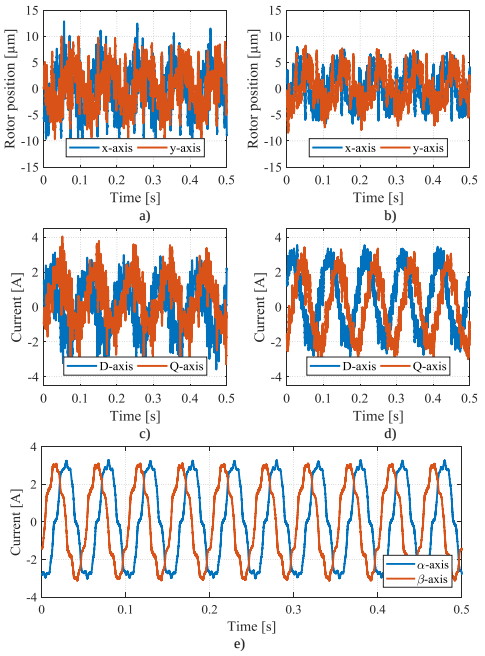

Figure 14: Rotation test with speed of 300 r/min. Measured rotor position is shown for D-end and ND-end in a) and b), respectively. Levitation winding current for D-end and ND-end is shown in c) and d). respectively. Torque producing current in the D-end motor windings is shown in e). The motor currents are represented in $\alpha\beta$ -armature reference frame.

6 Summary of the Commissioning Steps

A summary of the commissioning steps is given to explicate the connection between the proposed control methods and the control system.

- **Step I**: Derivation of the rigid system model (2) using the rotor mass m and the inertia J with the position stiffness K_x and current stiffness K_i parameters obtained from the FEM and validated by experiments (see Fig. 5). To derive the full model used for the control design (10), the inner current controller dynamics (14) is considered.
- **Step II**: MIMO state space controller design considering pole placement or LQR. The initial selection for the pole placement control is to place all the poles in the same location, that is, $z = e^{-\sqrt{\frac{K_x}{m}}\cdot T_s}$, which corresponds to the eigenvalue for a spring-mass-system with a negative stiffness. The LQR can be straightforwardly designed with Bryson's rule by selecting reasonable maximum input signal and output deviation limits for the controller. A good initial selection for the maximum output deviation is to consider smaller values for the deviation than the values given in the ISO standard ISO 14839-2:2004(E) (2004), where the acceptable rotor vibration with respect to the air-gap length in magnetic levitation applications is recommended. Here, a value of $0.083{\cdot}C_{min}$ is considered, where C_{min} is the minimum clearance. The maximum levitation current can be used as

the initial value for the input deviation. An acceptable control effort can be achieved by tuning the input deviation, and thus, in this paper, the selected input deviation is 2 A.

- **Step III**: Estimator design (14) based on the system model, The estimator can be tuned by using the general guidelines given for instance in Messager and Binder (2016) , Franklin et al. (2010) so that the observer poles are around 4–10 times faster than the closed-loop poles. Here, a ten times faster design is considered.

- **Step IV**: Check in the simulation that the desired response and dynamics are obtained for the lift-up test (see example in Fig. 9 a) and c)). If the requirements are not met, redesign the controller and the estimator in **Steps II** and **III**.

- **Steps V–VI**: Experimental lift-up test, where the basic functionality of the controller is further verified. After that, identification tests supported with a model validation routine should be carried out. Here, the adaptive amplitude stepped sine Vuojolainen et al. (2017) is used as an excitation signal in the identification experiments.

After the proposed commissioning routine, the natural next step is the controller retuning based on the identified model, if the initial mathematical model does not correspond to the identified one. This step is important, especially if there is some identified dynamics, such as cross-coupling, which should be considered in the final controller design for the rotation over the whole speed range. To this end, previous studies focusing on the control of different bearingless machine applications Zhang et al. (2016), Zhao and Zhu (2017) have shown that PID-based controllers are useful tools for stabilizing a rigid rotor. However, a MIMO controller should be considered as a final controller as it is more straightforward to tune in order to adequately stabilize the complex dynamics in the case of a flexible rotor Yoon et al. (2013). Moreover, in general, when considering a magnetically levitated high-speed motor application with a very high speed requirement, the PID controller has certain shortcomings that can destabilize the system for example if there are flexible modes within the controller bandwidth. When commissioning is carried out with a MIMO controller, the final control law can be designed using the same algorithm straightforwardly. In this case, this ensures a better cooperation between bearingless motors for the stabilization of the system and stable rotational operation over the whole speed range.

7 Conclusion

Commissioning steps for fully levitated bearingless machine using the model based control approach is presented. It is beneficial to apply the MIMO control principles over very traditional PID-based control structures, which do not take into account the coupling of the rotor system. In this paper, it was shown that the well-established MIMO AMB control principles can be straightforwardly applied to a bearingless machine system. By comparing the adopted controllers, it is shown that the LQR outperforms the pole placement controller. Designing an LQR-based controller is much more straightforward as a result of the more intuitive tuning methods. Secondly, weighting-function-based controllers are not sensitive to a model order change as the weights affect the inputs and outputs but not the states themselves. Updating a rigid body rotor model to a flexible model would increase the number of poles to be tuned. Naturally, the pole placement controller is more suitable for simpler systems than a complex MIMO system, such as a 4-DOF levitated rotor system, but in this paper, it was only considered as an example MIMO control case for a bearingless machine.

The results presented in this paper are important as the 5-DOF operation of bearingless machines has not been comprehensively analyzed in the literature thus far. The 5-DOF operation was shown and analyzed with two distinct MIMO control approaches using simple rigid rotor model. The proposed controllers can be applied for commissioning purposes, and it was experimentally shown that artificial-excitation-based system identification experiments can be carried out during full levitation operation. Additionally, stability of the LQR based levitation controller was verified with the low-speed rotation tests.

References

Cao, X., Yang, H., Zhang, L., and Deng, Z. Compensation strategy of levitation forces for single-winding bearingless switched reluctance motor with one winding total short circuited. *IEEE Trans. on Ind. Electron.*, 2016. 63(9):5534–5546. doi:10.1109/TIE.2016.2558482.

Cao, X., Zhou, J., Liu, C., and Deng, Z. Advanced control method for single-winding bearingless switched reluctance motor to reduce torque ripple and radial displacement. *IEEE Trans. Energy Convers.*, 2017. PP(99):1–1. doi:10.1109/TEC.2017.2719160.

Chen, L. and Hofmann, W. Modelling and control of one bearingless 8-6 switched reluctance motor with single layer of winding structure. In *14th European*

Conf. on Power Electron. and Appl. (EPE). pages 1–9, 2011.

Chiba, A., Fukao, T., Ichikawa, O., Oshima, M., Takemoto, M., and Dorrell, D. G. *Magnetic bearings and bearingless drives*, pages 1–15. Elsevier, Amsterdam, The Netherlands, 2009. doi:10.1016/B978-0-7506-5727-3.X5000-7.

Chiba, A., Horima, S., and Sugimoto, H. A principle and test results of a novel bearingless motor with motor parallel winding structure. In *IEEE Energy Convers. Congr. and Expo. (ECCE)*. pages 2474–2479, 2013. doi:10.1109/ECCE.2013.6647019.

Franklin, G. F., Powell, J., and Workman, M. L. *Digital control of dynamic systems*, pages 364, 400–401. Ellis-Kagle Press, 1200 Pilarcitos Ave. Halfmoon Bay, CA 94019, 2010.

Gerhard Schweitzer, E. H. M. *Magnetic bearings*, pages 1–82. Springer-Verlag Berlin Heidelberg, Springer-Verlag Berlin Heidelberg, 2009. doi:10.1007/978-3-642-00497-1.

Hoshi, H., Shinshi, T., and Takatani, S. Third-generation blood pumps with mechanical noncontact magnetic bearings. *Artificial Organs*, 2006. 30(5):324–338. doi:10.1111/j.1525-1594.2006.00222.x. Cited By 153.

Huang, J., Li, B., Jiang, H., and Kang, M. Analysis and control of multiphase permanent-magnet bearingless motor with a single set of half-coiled winding. *IEEE Trans. on Ind. Electron.*, 2014. 61(7):3137–3145. doi:10.1109/TIE.2013.2279371.

ISO 14839-2:2004(E). Mechanical vibration – Vibration of rotating machinery equipped with active magnetic bearings – Part 2: Evaluation of vibration. Standard, International Organization for Standardization, Geneva, CH, 2004.

Jaatinen, P., T. Sillanpää, R. J., and Pyrhönen, O. Automated parameter identification platform for magnetic levitation systems: case bearingless machine. In *15th Int. Symp. on Magnetic Bearings*. 2016.

Kauss, W. L., Gomes, A. C. D. N., Stephan, R. M., and David, D. F. B. Lqr control of a bearingless machine implemented with a dsp. In *11th Int. Symp. on Magnetic Bearings*. pages 475–480, 2008.

Kolondzovski, Z., Sallinen, P., Belahcen, A., and Arkkio, A. Rotordynamic analysis of different rotor structures for high-speed permanent-magnet electrical machines. *IET Electric Power Appl.*, 2010. 4(7):516–524. doi:10.1049/iet-epa.2008.0272.

Messager, G. and Binder, A. Observer-based pole placement control for a double conical high-speed bearingless permanent magnet synchronous motor. In *18th European Conf. on Power Electron. and Appl. (EPE)*. pages 1–10, 2016. doi:10.1109/EPE.2016.7695264.

Mitterhofer, H. and Amrhein, W. Motion control strategy and operational behaviour of a high speed bearingless disc drive. In *6th IET Int. Conf. on Power Electron., Mach. and Drives (PEMD)*. pages 1–6, 2012. doi:10.1049/cp.2012.0297.

Noh, M., Gruber, W., and Trumper, D. L. Hysteresis bearingless slice motors with homopolar flux-biasing. *IEEE/ASME Transactions on Mechatronics*, 2017. PP(99):1–1. doi:10.1109/TMECH.2017.2740429.

Ooshima, M., Chiba, A., Rahman, A., and Fukao, T. An improved control method of buried-type ipm bearingless motors considering magnetic saturation and magnetic pull variation. *IEEE Trans. Energy Convers.*, 2004. 19(3):569–575. doi:10.1109/TEC.2004.832065.

Ooshima, M., Kobayashi, A., and Narita, T. Stabilized suspension control strategy at failure of a motor section in a d-q axis current control bearingless motor. In *IEEE Ind. Ind. Soc. Annu. Meeting*. pages 1–7, 2015. doi:10.1109/IAS.2015.7356813.

Qiu, Z., Dai, J., Yang, J., Zhou, X., and Zhang, Y. Research on rotor eccentricity compensation control for bearingless surface-mounted permanent-magnet motors based on an exact analytical method. *IEEE Trans. Magn.*, 2015. 51(11):1–4. doi:10.1109/TMAG.2015.2451163.

Schneider, T. and Binder, A. Design and evaluation of a 60 000 rpm permanent magnet bearingless high speed motor. In *7th Int. Conf. on Power Electron. and Drive Sys. (PEDS)*. pages 1–8, 2007. doi:10.1109/PEDS.2007.4487669.

Severson, E., Nilssen, R., Undeland, T., and Mohan, N. Design of dual purpose no voltage combined windings for bearingless motors. *IEEE Trans. Ind. Appl.*, 2017. PP(99):1–1. doi:10.1109/TIA.2017.2706653.

Smirnov, A. *AMB system for high-speed motors using automatic commissioning*. Ph.D. thesis, Lappeenranta University of Technology, Lappeenranta, Finland, 2012.

Sun, X., Shi, Z., Chen, L., and Yang, Z. Internal model control for a bearingless permanent magnet synchronous motor based on inverse system method. *IEEE Trans. Energy Convers.*, 2016a. 31(4):1539–1548. doi:10.1109/TEC.2016.2591925.

Sun, X., Xue, Z., Zhu, J., Guo, Y., Yang, Z., Chen, L., and Chen, J. Suspension force modeling for a bearingless permanent magnet synchronous motor using maxwell stress tensor method. *IEEE Trans. Appl. Supercond.*, 2016b. 26(7):1–5. doi:10.1109/TASC.2016.2599708.

Swanson, E. E., Maslen, E. H., Li, G., and Cloud, C. H. Rotordynamic design audits of amb supported machinery. In *37th Turbomachinery Symp.* pages 133–158, 2008.

Takemoto, M., Iwasaki, S., Miyazaki, H., Chiba, A., and Fukao, T. Experimental evaluation of magnetic suspension characteristics in a 5-axis active control type bearingless motor without a thrust disk for wide-gap condition. In *IEEE Energy Convers. Congr. and Expo. (ECCE)*. pages 2362–2367, 2009. doi:10.1109/ECCE.2009.5316174.

Vuojolainen, J., Nevaranta, N., Jastrzebski, R., and Pyrhönen, O. Comparison of excitation signals in active magnetic bearing system identification. *Modeling, Identification and Control*, 2017. 38(3):123–133. doi:10.4173/mic.2017.3.2.

Warberger, B., Reichert, T., Nussbaumer, T., and Kolar, J. W. Design considerations of a bearingless motor for high-purity mixing applications. In *SPEEDAM*. pages 1454–1459, 2010. doi:10.1109/SPEEDAM.2010.5545102.

Xue, B., Wang, H., Tang, S., and Liang, J. Levitation performance analysis for bearingless switched reluctance motor. In *18th Int. Conf. on Elect. Machines and Syst. (ICEMS)*. pages 264–270, 2015. doi:10.1109/ICEMS.2015.7385039.

Yamamoto, N., Takemoto, M., Ogasawara, S., and Hiragushi, M. Experimental estimation of a 5-axis active control type bearingless canned motor pump. In *IEEE Int. Electric Machines and Drives Conf. (IEMDC)*. pages 148–153, 2011. doi:10.1109/IEMDC.2011.5994829.

Yang, S. M. and Chen, C. C. Improvements of radial force control for a spm type pmsm self-bearing motor drive (ecce). In *IEEE Energy Convers. Congr. and Expo.* pages 3451–3455, 2009. doi:10.1109/ECCE.2009.5316514.

Yang, Y., Deng, Z., Yang, G., Cao, X., and Zhang, Q. A control strategy for bearingless switched-reluctance motors. *IEEE Trans. Power Electron.*, 2010. 25(11):2807–2819. doi:10.1109/TPEL.2010.2051684.

Yoon, Y., Lin, Z., and Allaire, P. E. *Control of surge in centrifugal compressors by active magnetic bearings*, pages 92–94. Springer-Verlag London, Berlin, Heidelberg, 2013. doi:10.1007/978-1-4471-4240-9.

Zhang, S., Liu, L., Wang, S., Jia, Y., and Qie, C. Complete control of radial suspension force for bearingless induction motors. In *IEEE 11th Conf. on Ind. Electron. and Appl. (ICIEA)*. pages 2180–2184, 2016. doi:10.1109/ICIEA.2016.7603950.

Zhao, C. and Zhu, H. Design and analysis of a novel bearingless flux-switching permanent magnet motor. *IEEE Trans. on Ind. Electron.*, 2017. 64(8):6127–6136. doi:10.1109/TIE.2017.2682018.

ACTA UNIVERSITATIS LAPPEENRANTAENSIS

869. KARHU, MIIKKA. On weldability of thick section austenitic stainless steel using laser processes. 2019. Diss.

870. KUPARINEN, KATJA. Transforming the chemical pulp industry – From an emitter to a source of negative CO2 emissions. 2019. Diss.

871. HUJALA, ELINA. Quantification of large steam bubble oscillations and chugging using image analysis. 2019. Diss.

872. ZHIDCHENKO, VICTOR. Methods for lifecycle support of hydraulically actuated mobile working machines using IoT and digital twin concepts. 2019. Diss.

873. EGOROV, DMITRY. Ferrite permanent magnet hysteresis loss in rotating electrical machinery. 2019. Diss.

874. PALMER, CAROLIN. Psychological aspects of entrepreneurship – How personality and cognitive abilities influence leadership. 2019. Diss.

875. TALÁSEK, TOMÁS. The linguistic approximation of fuzzy models outputs. 2019. Diss.

876. LAHDENPERÄ, ESKO. Mass transfer modeling in slow-release dissolution and in reactive extraction using experimental verification. 2019. Diss.

877. GRÜNENWALD, STEFAN. High power fiber laser welding of thick section materials - Process performance and weld properties. 2019. Diss.

878. NARAYANAN, ARUN. Renewable-energy-based single and community microgrids integrated with electricity markets. 2019. Diss.

879. JAATINEN, PEKKO. Design and control of a permanent magnet bearingless machine. 2019. Diss.

880. HILTUNEN, JANI. Improving the DC-DC power conversion efficiency in a solid oxide fuel cell system. 2019. Diss.

881. RAHIKAINEN, JARKKO. On the dynamic simulation of coupled multibody and hydraulic systems for real-time applications. 2019. Diss.

882. ALAPERÄ, ILARI. Grid support by battery energy storage system secondary applications. 2019. Diss.

883. TYKKYLÄINEN, SAILA. Growth for the common good? Social enterprises' growth process. 2019. Diss.

884. TUOMISALO, TEEMU. Learning and entrepreneurial opportunity development within a Finnish telecommunication International Venture. 2019. Diss.

885. OYEDEJI, SHOLA. Software sustainability by design. 2019. Diss.

886. HUTTUNEN, MANU. Optimizing the specific energy consumption of vacuum filtration. 2019. Diss.

887. LIIKANEN, MIIA. Identifying the influence of an operational environment on environmental impacts of waste management. 2019. Diss.

888. RANTALA, TERO. Operational level performance measurement in university-industry collaboration. 2019. Diss.

889. LAUKKANEN, MINTTU. Sustainable business models for advancing system-level sustainability. 2019. Diss.

890. LOHRMANN, CHRISTOPH. Heuristic similarity- and distance-based supervised feature selection methods. 2019. Diss.

891. ABDULLAH, UMMI. Novel methods for assessing and improving usability of a remote-operated off-road vehicle interface. 2019. Diss.

892. PÖLLÄNEN, ILKKA. The efficiency and damage control of a recovery boiler. 2019. Diss.

893. HEKMATMANESH, AMIN. Investigation of EEG signal processing for rehabilitation robot control. 2019. Diss.

894. HARMOKIVI-SALORANTA, PAULA. Käyttäjät liikuntapalvelujen kehittäjinä - Käyttäjälähtöisessä palveluinnovaatioprosessissa käyttäjien tuottama tieto tutkimuksen kohteena. 2020. Diss.

895. BERGMAN, JUKKA-PEKKA. Managerial cognitive structures, strategy frames, collective strategy frame and their implications for the firms. 2020. Diss.

896. POLUEKTOV, ANTON. Application of software-defined radio for power-line-communication-based monitoring. 2020. Diss.

897. JÄRVISALO, HEIKKI. Applicability of GaN high electron mobility transistors in a high-speed drive system. 2020. Diss.

898. KOPONEN, JOONAS. Energy efficient hydrogen production by water electrolysis. 2020. Diss.

899. MAMELKINA, MARIA. Treatment of mining waters by electrocoagulation. 2020. Diss.

900. AMBAT, INDU. Application of diverse feedstocks for biodiesel production using catalytic technology. 2020. Diss.

901. LAAPIO-RAPI, EMILIA. Sairaanhoitajien rajatun lääkkeenmääräämistoiminnan tuottavuuden, tehokkuuden ja kustannusvaikuttavuuden arviointi perusterveydenhuollon avohoidon palveluprosessissa. 2020. Diss.

902. DI, CHONG. Modeling and analysis of a high-speed solid-rotor induction machine. 2020. Diss.

903. AROLA, KIMMO. Enhanced micropollutant removal and nutrient recovery in municipal wastewater treatment. 2020. Diss.

904. RAHIMPOUR GOLROUDBARY, SAEED. Sustainable recycling of critical materials. 2020. Diss.

905. BURGOS CASTILLO, RUTELY CONCEPCION. Fenton chemistry beyond remediating wastewater and producing cleaner water. 2020. Diss.

906. JOHN, MIIA. Separation efficiencies of freeze crystallization in wastewater purification. 2020. Diss.

LUT University

ISBN 978-952-335-517-0
ISBN 978-952-335-518-7 (PDF)
ISSN-L 1456-4491
ISSN 1456-4491
Lappeenranta 2020